Physicochemical effects of turbulence and entrainment in atmospheric pressure plasma jets.

Thesis submitted in accordance with the requirements of the University of Liverpool for the degree of Doctoral in Philosophy by

Youssef MORABIT, M. Eng

Centre for Plasma Microbiology

University of Liverpool

December 2020

Table of Contents

Abstract

Atmospheric pressure plasma jets (APPJ) are currently the focus of an intense international research effort due to their unique chemical and physical characteristics. A defining aspect of the plasma jet is the interplay between plasma physics, plasma chemistry, and fluid dynamics which ultimately dictate application efficacy. This project focuses on uncovering the link between the fluid dynamics of the emerging noble gas channel into quiescent ambient air and the chemical reactions induced by the reactive species produced in the discharge. Several, biochemically relevant species, reactive oxygen, and nitrogen species (RONS) are created such as O, OH, O_3, H_2O_2, NO. These reactions occur with the presence of air, thus at the interface of the shear layer of the plasma jet and the medium. Making it a crucial parameter toward the generation of relevant reactive species, this interface is intrinsically linked to fluid dynamic characteristics of the jet. Particle Image Velocimetry provides novel time- and spatially-resolved quantitative velocity measurements of the jet with and without the influence of the plasma discharge. This influence is characterised; the induced-turbulence is generated by disturbances created in the shear layer of the jet by gas heating and electrohydrodynamics (EHD), moreover the observation and measurement of velocity fluctuations and turbulence in the laminar region of the jet provide novel insight on the fluid dynamics consequences of the plasma discharge. Those perturbations propagate along the jet and alter the structure with an intensity dependant on the fluid dynamic parameters and the plasma input parameters. These observations show the presence of instability on the plasma jet structure, particularly the edges, thus the results imply the presence of air entrainment in the laminar region of the jet which impact the plasma physics and chemistry.

Furthermore, the plasma-induced velocity increase of the jet is characterised, and is below a 10% increase of the initial velocity. In contrary to past assumptions, the velocity effect of the plasma discharge is thus unable to solely alter the state of the jet. Rayleigh scattering and Laser-induced fluorescence provide insights on the induced air entrainment and mixing in the shear layer, and the spatial distribution of relevant chemical species (OH). The results show that plasma-induced perturbations decrease the laminar region length, increase the turbulence intensity, and increase the quenching rate of OH fluorescent state. This indicates the critical aspect of the shear layer instabilities on the physicochemical characteristics of the plasma jet. Ultimately, the plasma jet applications mostly directed downward impinging on a target, the electrical parameters of the generation of the plasma revealed to be able to control the structure of the jet; thus the gas mixing and the chemistry.

The adaptability of the plasma jet configuration and input parameters allow a decisive control over the jet structure and the chemistry while being used at atmospheric pressure and near room temperature, it makes it a convenient non-obstructing technique for localised treatment. This study shows the ability to control the chemistry of the jet through the electrical parameters, for applications where the wanted chemistry is already in the jet, generating a laminar jet will oppose greatly the mixing with the environment. Whereas, applications where the mixing with ambient air is mandatory to obtain relevant reactive species, electrical parameters prone to perturb and provoke earlier transition to turbulence will be crucial. The electrical parameters in a pulse-driven APPJ, mainly the repetition frequency and the pulse width are crucial to controlling the jet structure and chemistry in a cost-efficient way. The chemistry issued from plasma jet generation has proven to be of great interest in several fields, such as material processing, wound healing, bacteria and. These efforts will pave the way for new understanding and applications of the plasma jet.

Acknowledgements

First, I would like to express my gratitude to my supervisor Pr James Walsh who gave me the opportunity to carry out this Ph.D.; he shared his knowledge and his love for Robbie Williams, while the first was the most important, the latter built unforgettable memories. His support and guidance throughout the steps of this adventure were crucial in my academic development.

A Special thank goes to my co-supervisor Eric Robert for his help and guidance during this journey, as well as my collaborators Aaron Dickenson, Richard Whalley, Mohammad Hasan, and Martina Modic, with whom I had the pleasure of meeting and enjoyed working on several projects. My thanks go to my academic advisors Pr Xin Tu and Dr. Mohammad Hassan, for their guidance and feedback from annual reviews.

I want to express my appreciation to Gareth Blacoe, Jill Anson, and Phil Hilton for their great help and the enjoyable daily chat, the best smiles in the building. Many thanks to my fellow researchers; Aaron Dickenson for the excessive amount of Coffee intake, Mike Barnes, Paddy McCarthy as a very inspiring character, Stephane Simon as a fellow rugby fan, Andreas Katsigiannis, and the delicious Greek sweets, Stefania Fabbri, Peter Ryan, Matt Smith, Felix Walk, Brandon Harris, Kirsty McKay, Breno Salgado who have all made my experience over the course of this Ph.D. a very enjoyable journey. To my friends Abdelhamid Dahou, Younes El Farouki, Mehdi Hyani, Pierre Levent, I would like to express my sincere appreciation for their support and the good times shared. To my aunt Fatiha and her beautiful two kids, it is a blessing to see you whenever possible. To my brother, I am very fortunate that we can spend time having fun. I want to end with a thank you to my mom for making this possible, and for supporting me through the difficult times.

List of Figure

List of Table

List of abbreviations

AC: Alternative current

APPJ: Atmospheric pressure plasma jet

COST: Cooperation in Science and Technology

DBD: Dielectric barrier discharge

DC: Direct current

DNA: Deoxyribonucleic acid

ECM: Extracellular matrix

EHD: Electrohydrodynamic

ESKAPE: Enterococcus faecium, Staphylococcus aureus, Klebsiella pneumoniae, Acinetobacter baumannii, Pseudomonas aeruginosa, and Enterobacter spp.

FTIR: Fourier transform infrared spectroscopy

GAPDH: Glyceraldehyde 3-phosphate dehydrogenase

G+: Gram-positive

G-: Gram-negative

H_2DCFDA: 2',7'-dichlorodihydrofluorescein diacetate

HEPA: High-efficiency particulate air

HV: High Voltage

ICCD: Intensified charge-coupled device

IW: Ionisation wave

LIF: Laser-induced fluorescence

PIV: Particle image velocimetry

RANS: Reynolds-Averaged Navier-Stokes

RNS: Reactive nitrogen species

ROS: Reactive oxygen species

RONS: Reactive oxygen and nitrogen species

SLM: Standard litre per minute

TALIF: Two-photon Absorption Laser-Induced Fluorescence

TDLAS: Tunable diode laser absorption spectroscopy

MS: Mass spectroscopy

TEMP: 2,2,6,6-tetramethylpiperidine

TEMPO: 2,2,6,6-tetramethyl- piperidine-1oxyl

UV: Ultraviolet

List of symbols

A: Cross-sectional area

A_E: Einstein emission coefficient

A_L: Area of the laser beam

Cs: Cross-section

D: Capillary inner diameter

d: Distance

D_{ij}: Binary diffusion coefficient

D_T: Turbulent diffusivity

d_p: Particle diameter

E: Electric field

E_0: External electric field

E_a: Internal electric field

E_g: Energy gap

E_L: Laser energy per pulse

f: Frequency

f_c: Characteristic frequency

Fr: Froude number

g: Gravitational acceleration

g_{int}: Overlap integral

h: Planck constant

hν: Photon energy

I: Current

I_0: Incident wave intensity

I_{Sc}: Scattered light intensity

I_L: Laser irradiance

k_B: Boltzmann constant

T: Temperature

T_e: Electron temperature

Tg: Gas temperature

T_i: Ion temperature

k: Turbulent kinetic energy

M : Molecular weight

n_e: Density of electrons

n_{exc}: Density of OH in the excited state

n_i: Density of ions

N_n: Density of scattering particles

P: Pressure

P_T: Production of turbulence

Q: Volumetric flow rate

R: Capillary inner radius

r: Radial axis

$r_{0.5}$: Half-radius fluctuations

Re: Reynolds number

$R_{x,r}$: Reynolds stress

Sc_T: Turbulent Schmidt number

s'_{ij}: Fluctuating deformation rate

S_k: Strokes number

S_{LIF}: Intensity of the laser-induced fluorescence

S_{Ray}: Rayleigh scattered signal

St: Strouhal number

t_L: Temporal length of the laser pulse

U: Velocity magnitude

U_0: Initial velocity

U_c: Centreline velocity

U_{eff}: Effective velocity

U_m: Maximum velocity

U_r: Radial velocity

$\overline{U}_r$: Time-averaged radial velocity

u_r: Radial turbulence component

u_r': Turbulence intensity of the radial velocity fluctuations

U_x: Streamwise velocity

$\overline{U}_x$: Time-averaged streamwise velocity

u_x: Streamwise turbulence component

u_x': Turbulence intensity of the streamwise velocity fluctuations

V: Voltage

$\vec{V}$: Diffusion velocity

V_{Ray}: Rayleigh scattering volume of the measured signal

x: Streamwise axis

x_0: Virtual origin

x_i: Mole fraction

x_t: Transition-to-turbulence point

x_p: Potential core length

α: Optical polarizability

$\vec{\Gamma}$: Diffusive flux

$\partial^{\beta=0}\sigma_0 / \partial\Omega$: Differential cross-section for Rayleigh scattering

ΔL: Temporal FWHM of the laser pulse

ΔP: Pressure variation

Δs: The spatial FWHM of the laser beam at the observation point

Δt: Time delay between laser pulses

Δx: Tube length

Δx_v: Length of the detection volume

Δy_v: Width of the detection volume

ε: Turbulent kinetic energy dissipation rate

ξ: Scattering angle

η: Calibration constant

θ: Momentum thickness

λ: Wavelength

λ_L; Laser wavelength

μ: Fluid viscosity

ν: Frequency

ν_v: Kinematic viscosity

ν_j: Injected fluid kinematic viscosity

ρ: Density

ρ_a: Ambient fluid density

ρ_f: Fluid density

ρ_j: Injected fluid density

ρ_p: Particle density

ω: Angular frequency

ω_i: Mass fraction

Publications

First authored publications:

Y. Morabit, R. D. Whalley, E. Robert, M. I. Hasan & J. L. Walsh. Turbulence and entrainment in an atmospheric pressure dielectric barrier plasma jet, 2019, Plasma Processes and Polymers, 17:e1900217

Y. Morabit, M. I. Hasan, R. D. Whalley, E. Robert, M. Modic and J. L. Walsh.

A review of the gas and liquid phase interactions in low-temperature plasma jets used for biomedical applications, 2021, European Physics Journal D, 75, 32

Co-author publications:

Dickenson, Y. Morabit, M. I. Hasan & J. L. Walsh

Directional mass transport in an atmospheric pressure surface barrier discharge, 2017, Scientific Reports, 7, 14003

M. I. Hasan, Y. Morabit, A. Dickenson & J. L. Walsh.

Impact of electrode geometry on an atmospheric pressure surface barrier discharge, 2017, Applied Physics Letters, 110, 264101

Conference proceedings:

Invited:

Y. Morabit, M. Hasan, R. D. Whalley & J. L. Walsh.

Turbulence and entrainment in plasma jets, 2019, iPlasmaNano, Porec Croatia.

Y. Morabit, J. L. Walsh, M. I. Hasan, R. D. Whalley.

Quantitative insights into the fluid interactions downstream of an atmospheric pressure dielectric barrier plasma jet, 2018, Conference Poster, European Physical Society Conference on Plasma Physics.

Chapter 1 Introduction

1.1 Rationale & Overview of the Challenge

The focus of an intense international research effort has currently been on atmospheric pressure plasma jets due to their unique chemical and physical characteristics. A defining aspect of the plasma jet is the interplay between plasma physics, plasma chemistry, and fluid dynamics, ultimately dictating application efficacy. This thesis explores the link between the fluid dynamics of the emerging noble gas channel into the quiescent ambient air and the reactive chemical species resulting from the interaction, ultimately addressing the complex situation of plasma-induced turbulence propagation in the expanding jet. These efforts will pave the way for novel biomedical applications of the plasma jet in the future.

Atmospheric pressure non-thermal plasma jets typically comprise a flowing noble gas plasma flushed into the ambient air. Such devices have proven to be extremely promising in some biomedical applications due to the reactive chemical species produced within the discharge. Several biochemically relevant species, known collectively as reactive oxygen and nitrogen species (RONS), are created.[1] These species are typically produced when the ambient air is entrained within the flowing noble gas channel. Consequently, knowledge of the physicochemical processes occurring at the interface between the flowing plasma and quiescent air is crucial to understand, and ultimately control, application efficacy. To date, the fluid dynamics occurring downstream of a plasma jet have been mostly observed with qualitative techniques (i.e., Schlieren photography). However, the work reported in this thesis is the first to apply a quantitative analysis technique (i.e., Particle image velocimetry (PIV)) to uncover a detailed understanding of the interaction between the plasma and the quiescent air. Particular focus is directed toward plasma-induced turbulence downstream of the jet orifice, with spatially

resolved Rayleigh scattering and Laser-induced fluorescence being used to provide further insights into the entrainment and mixing of ambient air and the spatial distribution of OH in the jet.

This study provides quantitative velocity data of a sinusoidally driven atmospheric pressure plasma jet (APPJ) at several different flow rates and applied voltages. An in-depth analysis of the velocity components under the influence of the plasma discharge and the related turbulent components was performed from this investigation. The plasma-induced turbulence is highlighted through turbulent kinetic energy and Reynolds shear stress measurements. It was demonstrated that the perturbation in the flow caused by the plasma discharge has a considerable impact on the gas mixing and, consequently, discharge chemistry. To further probe the underpinning mechanisms of turbulence generation, a pulse-driven APPJ was adopted. By varying the repetition frequency, the dominant repetition frequency to generate perturbations in the jet shear layer and induce turbulence was examined. The effect of voltage polarity and the voltage pulse width was also important, with both polarity and pulse width impacting the length of the plasma plume and the laminar-to-turbulent transition point. Notably, these electrical parameters offer a means to control the behaviour of the jet, introducing the exciting possibility to electrically manipulate air entrainment, gas mixing, and RONS chemistry in an APPJ.

One of the most widely used DBD configurations is the atmospheric pressure plasma jet, which consists of a noble gas plasma flowing within a capillary, exhausted into the ambient air. The configuration has attracted enormous attention recently due to its unique ability to generate a wealth of reactive chemical species that are directly accessible under ambient conditions beyond the confines of the electrodes, thus offering both inherent safety and

reactivity. Such devices are widely used in high-value materials processing applications and, more recently, in the biomedical area.

The application of a plasma jet expanding into the ambient air and impinging onto a target is of great practical importance yet almost entirely unexplored from a quantitative perspective. The fluid dynamics effects induced in the flowing gas and quiescent background are complex yet vital if the discharge chemistry is to be fully understood. It is well known that the interaction between a noble gas plasma and molecular gases results in a rich cocktail of reactive species. However, the production of such species is spatially and temporarily dependant; thus, understanding the effect of the fluid dynamics, especially the generation of turbulence, on the chemistry is crucial for the optimisation of plasma jet applications.

1.2 Aims and objectives

This work aims to uncover a new understanding of how the plasma interacts influences the fluid dynamics of the jet and how plasma-induced changes affect the generation of reactive chemical species. This understanding is crucial as all applications of the plasma jet inevitably involve the transport of reactive plasma species to a downstream sample. Consequently, the new insights gained in this work will contribute significantly to the current body of knowledge in the area, potentially enabling new application domains. Given the recent interest in using such devices for biomedical applications, a low-temperature helium plasma jet has been chosen as the focus for this work; as is typical in many applications, the jet was allowed to flow into the ambient quiescent ambient air.

Several research objectives will be addressed to reveal a new understanding of the underpinning processes, including:

(1) To develop a new method for injecting seeding particles in the plasma jet that has minimal impact on the properties of the plasma while enabling quantitative measures of the jet flow to be made.

(2) To show the link between air entrainment and turbulence generation induced by the plasma using qualitative measurements including Schlieren photography and, more importantly, quantitative measurements using Particle Image Velocimetry.

(3) To identify the physicochemical effects of plasma-induced turbulence using multiple experimental techniques such as Rayleigh scattering, Particle Image Velocimetry, and Laser-Induced Fluorescence (LIF).

(4) To characterise the key discharge parameters responsible for generating turbulence in a plasma jet and thus establish a framework on which the discharge chemistry can be manipulated.

Achieving these objectives provides considerable scope to undertake novel research. The interaction between the plasma emerging from the jet orifice and the quiescent air is extremely complex due to the electrohydrodynamic forces generated by the discharge. Thus very few quantitative studies have been conducted. Many studies have explored qualitative techniques to probe this complex situation (e.g., Schlieren imaging),[2–5] but such efforts shed little light on the underpinning processes. Quantitative measurement techniques used to study fluid motion are typically limited in spatial or temporal resolution and do not allow instantaneous capture of the fluid motion. They also present limitations such as being obtrusive/intrusive to the fluid flow (e.g., hot wire anemometry[6] or Laser Doppler Anemometry[7]). Due to the complexities of the situation and the lack of experimental techniques

available, there is a real opportunity to deliver high-impact research findings that will provide new insights into many emerging applications in the biomedical area.

Notable, a state-of-the-art high-speed PIV system is available within the Centre for Plasma Microbiology, which offers an opportunity to gain quantitative insight into the complex fluid interactions within the plasma jet. The quantitative measurements presented in this work are believed to be one of the first made on a plasma jet. The main practical challenge was to seed the jet with particles to characterise the flow using the PIV system without disturbing the discharge. In addition to PIV, many other advanced spectroscopy-based techniques such as LIF and Rayleigh scattering were used to provide insight into the discharge chemistry, allowing a link between the fluid dynamics and discharge chemistry made. Thus, this thesis offers several notable contributions, including:

(1) A report on the qualitative and quantitative results on the influence of plasma generation on the behaviour of the jet flow, with a particular focus on the influence of the applied voltage and the gas flow rate. Measurements of the plasma-induced turbulence in the jet were performed and reported in a poster contribution at the 2018 European Physical Society Conference on Plasma Physics.

(2) A report outlining quantitative velocity measurements of a sinusoidal driven atmospheric pressure plasma jet combined with Rayleigh scattering and LIF. This contribution revealed novel insights into the intrinsic link between plasma generation, fluid dynamics, and chemistry. Experimental and computational results revealed the impact of plasma-induced turbulence on the structure of the jet, provoking air entrainment and gas mixing in the laminar region. The consequences of the induced turbulence on the OH spatial density in the plasma jet were assessed and published in the international journal *Plasma Processing and Polymers*.

(3) Through the use of a short-pulse driven APPJ, the influence of key electrical parameters (pulse width, repetition rate, and polarity) on the fluid dynamics of a plasma jet expanding into the ambient air and impinging on a target was examined. The work has been submitted to the European Physical Journal D: Atomic, Molecular, Optical, and Plasma Physics.

1.3 Introduction into low-temperature plasmas

Plasmas are ionised gases characterised by a mixture of neutral and charged particles, including electrons and ions. It is, on average, electrically neutral ($n_e = n_i$). The presence of free charge carriers allows plasma to be an electrical conductor. Plasmas are typically divided into hot plasmas such as Solar plasmas and Fusion reactors and low-temperature plasmas. The latter is composed of Thermal plasmas (i.e., Arcs, Plasma arc welding,[8] Plasma arc cutting[9]) and Non-thermal or cold plasmas (i.e., Plasma actuators,[10] APPJ[11]). When the temperature of the heavy particles is similar to that of the electrons, the plasma is considered to be in thermal equilibrium and is thus defined as thermal plasmas. In non-thermal plasma, the temperature differs profoundly between the electrons (T_e) and the heavy species (T_i, T_g). The low frequency of collisions between electrons and heavy particles and the difference in mass makes the transfer of kinetic energy inefficient. Thus the ions and neutrals stay at a low temperature, limiting the thermal influence of the plasma discharge over a target being ambient air or bio-relevant target, while still allowing high temperature chemistry through energetic electrons.[12] Depending on the discharge generation conditions, the temperature of the neutrals and ions can be close to room temperature and these particular plasmas are the focus of this thesis.

One way to create a plasma is by providing an external input of energy to a neutral gas. This energy input can ionise the system. This ionisation can proceed by several different

processes, the most crucial being direct ionisation of atoms or molecules by electron impact. Figure 1 shows ionisation through direct electron impact, electron attachment to atoms or molecules, and ion-molecule reactions. The ionisation occurs when a free electron collides with a neutral atom; the free electron has an energy higher than the ionisation potential of the outermost electron being removed from the neutral, creating of positively charged ion (Figure 1a); or it is either trapped inside the electric potential barrier of the atom creating a negatively charged ion and hinder the production of electrons and thus the generation of the plasma as there is one less free electron (Figure 1b). In addition to these, recombination of electron-ion or ion-ion occurs, as well as excitation and dissociation of neutral species by electron impact, relaxation of excited species, and electron detachment.[13]

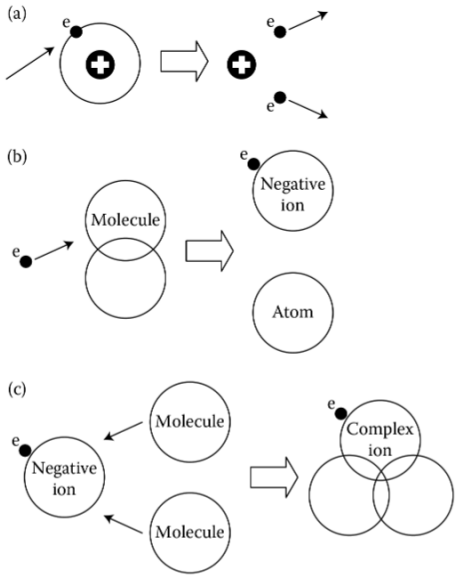

Figure 1: Illustrations of elementary processes. (a) Ionisations. (b) Dissociative attachment and formation of a negative ion. (c) Complex ion formation.[14]

The most common way of generating a plasma is to apply high electric fields between two electrodes. Several breakdown mechanisms can lead to the formation of a self-sustaining plasma discharge. For example, low-pressure DC discharge follows the Townsend mechanism; the electric fields accelerate the electrons before colliding with neutrals.[13] If the electrons gathered enough energy, the impact with neutrals could induce new electrons and ions. The recently created electrons are also accelerated and could participate in the initiating electron avalanche. The electrons are accelerated to higher energies due to the large mean free path of particles. This facilitates the generation of an electron avalanche and thus the ignition of plasma. At higher currents, the glow discharge mechanism prevails; the secondary emission of electrons comes from transferring the ions kinetic energy to the cathode releasing electrons, which participate in the discharge processes.[15] The excited atoms release their energy-emitting lights, providing the glowing aspect of discharge. The normal glow discharge where the current density is constant, and the plasma covers the cathode increasingly surging the current and the abnormal glow discharge, where the current increase follows the voltage increase.[15] At atmospheric pressure, the shorter mean free path hinders the ionisation of the gas, thus necessitating a stronger electric field to ignite a plasma.[13] However, depending on the power source, pressure, and electrode configuration, other mechanisms can be present. The generation of a high electric field and sharp edges, wires, or pins causes the electrical breakdown of a local region of the air in the proximity of the electrode, thus generating a corona discharge.[16] The presence of a secondary electrode would generate an electric arc. A sharp edge will have a higher electric field strength than the rest of the material. The electric field must be stronger than the dielectric strength of the air to provoke an electric breakdown. A strong enough electric field leads to a local ionisation; however, this phenomenon is contained in this local region. In the case of a dielectric barrier discharge (DBD) jet, the ionisation process is described by the streamer mechanism. The electric field generated by space charges participates in the total

electric field. In contrast, in a Townsend mechanism, this secondary electric field is negligible.[13,17] In a dielectric barrier discharge, space and surface charges can produce secondary electrons by direct ionisation leading to an electron avalanche; if the avalanche is of sufficient magnitude, then a positive streamer can be initiated. A positive streamer, also called a cathode-directed streamer, characterises a streamer that grows from anode to cathode. However, when this transformation takes place far from the anode, and the streamer grows toward both electrodes, it is called an anode-directed streamer or negative streamer. The streamer concept is described in Figure 2. The avalanche propagation is opposite to the local ionisation wave (IW). When the applied voltage is high enough, the space charge leads to a considerable internal electric field E_a.[18] The electrons are in the head of the avalanche while the positive ions remain behind creating a dipole. The dipole distorts the external electric field E_0. In front and behind the avalanche, both the external electric field E_0 and the internal electric field E_a add up. The newly formed stronger electric field accelerates the ionisation. Upon reaching the anode, the electrons flow into the electrode, and mostly an ionic trail remains in the gap. The primary avalanche emits high energy photons ($h\nu$) which through photoionisation generates the secondary avalanches. The new electrons join the ionic trail and form a quasi-neutral plasma channel. The cathode-directed streamer starts where the positive charge and the electric field of the primary avalanche are the highest, near the anode.

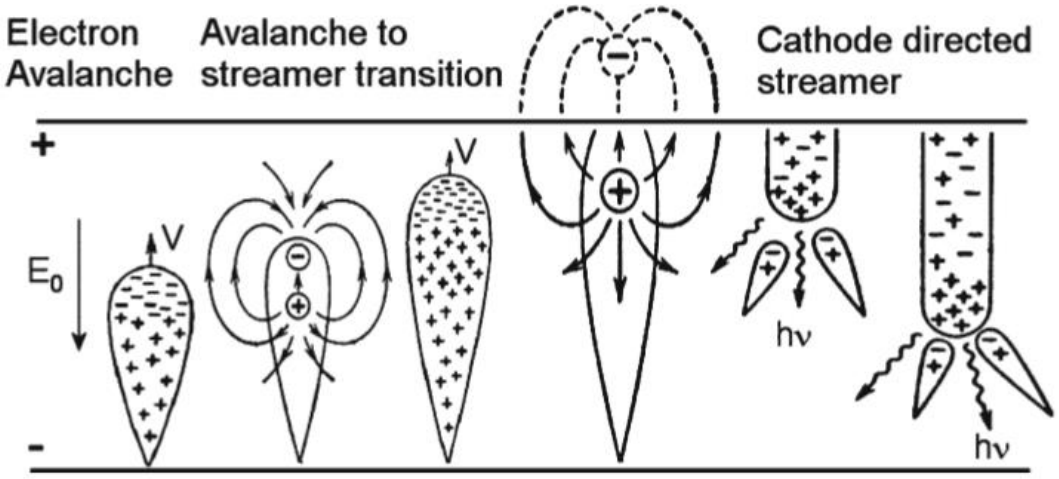

Figure 2: Timeline of microdischarge initiation stage. Processes shown are avalanche development triggered by occasional primary electron and transition of avalanche to the streamer.[19]

Typically, discharges at atmospheric pressure are usually created using noble gases such as neon, helium, and argon as they have a smaller reduced electric field value requirement to generate breakdowns (Table 1). Although noble gases are very stable, they also can generate metastable species if excited. A metastable is an excited species with a long lifetime; for example, the metastable helium atom He(2^3S) has excitation energy of 19.8 eV, which is significantly lower than the ionisation energy of helium (24.6 eV). Moreover, the metastable species participate in the ionisation processes in the plasma, with a collision of lower ionisation potential atom, also called Penning ionisation.[13]

Table 1: Electric fields sufficient for the Townsend breakdown of centimetre-size gaps at atmospheric pressure.[13]

Gas	E/p (kV/cm)
Air	32
Ar	2.7
He	10
N_2	35
Ne	1.4
O_2	30

Interest in atmospheric pressure cold plasma has grown due to our ability to create and apply it beyond the confines of a vacuum chamber; this has opened the gateway to application in healthcare and agriculture that are simply not feasible with vacuum plasma techniques. Unfortunately, with atmospheric pressure plasma discharges, the glow-to-arc transition can occur quickly, which poses a major problem in many emerging application areas. One of the most common ways to avoid the glow-to-arc transition is by adding a dielectric barrier in the discharge gap; this creates what is known as a dielectric barrier discharge. In an arc discharge, the electrodes become sufficiently hot to allow the cathode to emit electrons thermionically. It is distinguished into two states, non-thermal arcs and thermal arcs. In the context of the work described in this thesis and many of the current applications of atmospheric pressure plasma, arc plasma is undesirable due to its high-temperature characteristics.

The presence of a dielectric barrier prevents the use of DC; hence sinusoidal or pulsed voltages are used. The configuration is simple to operate and allows high power with little

possibility that the discharge will transition into an arc. It is widely used in the industry for ozone generation and has more recently been developed and used in a wide range of material processing and biomedical applications.[14] Usually, a material made of glass, quartz, or ceramic is used; the essential characteristics are low dielectric loss and high breakdown strength. The dielectric is an insulator that can be polarised under the application of an electric field. The positive charges follow the direction of the electric field, whereas the negative charges do the opposite. The breakdown strength defines the limit of the dielectric material before the material starts conducting current, leading to catastrophic failure.

1.4 Dielectric barrier discharge plasma jets

The definition of a plasma jet differs from the classic DBD plasma discharge by projecting the gas outside of the electrode arrangement into the environment.[20] This requires injecting a carrier or feed gas between the electrodes; noble gases are mostly used due to their chemically inert properties and low breakdown voltage. In this scenario, the neutral gas is flushed through a capillary where the discharge is generated; thus, the gas is ionised while flowing. At the capillary exit, the plasma impinges into the ambient environment surrounding the capillary and provokes various interactions depending on the gases at play. An essential aspect of any DBD system is that a time-varying voltage of sufficient magnitude to initiate breakdown must be applied. As the dielectric material covers one or both electrodes, there is no path for DC to flow. An additional factor influencing the characteristics of an APPJ is the choice of electrode configuration. Figure 3 shows a selection of the most common electrode configurations used in APPJ discharges. The configurations shown in Figure 3(a), (b) and (c) employ a coaxial electrode within the dielectric capillary to generate the discharge;[21–31] an advantage of this configuration is the reduced breakdown voltage. However, a drawback of this

configuration is the lack of a dielectric between the driven electrode and a downstream sample, making the system more liable to arcing. Configurations (d) and (e) employ ring electrodes positioned outside the capillary, acting to enhance electrical safety at the expense of an increased breakdown voltage.[32–37] The chosen electrode configuration can also affect the shape of the plasma plume beyond the capillary, thus influencing the generation and transport of reactive species.[25,38] In all cases, capacitive coupling to the ground provides a return path for current flow when a single electrode is employed. In most cases, the downstream sample acts as the ground electrode, and consequently, the plasma properties can be strongly influenced by the sample composition and the distance from the capillary.

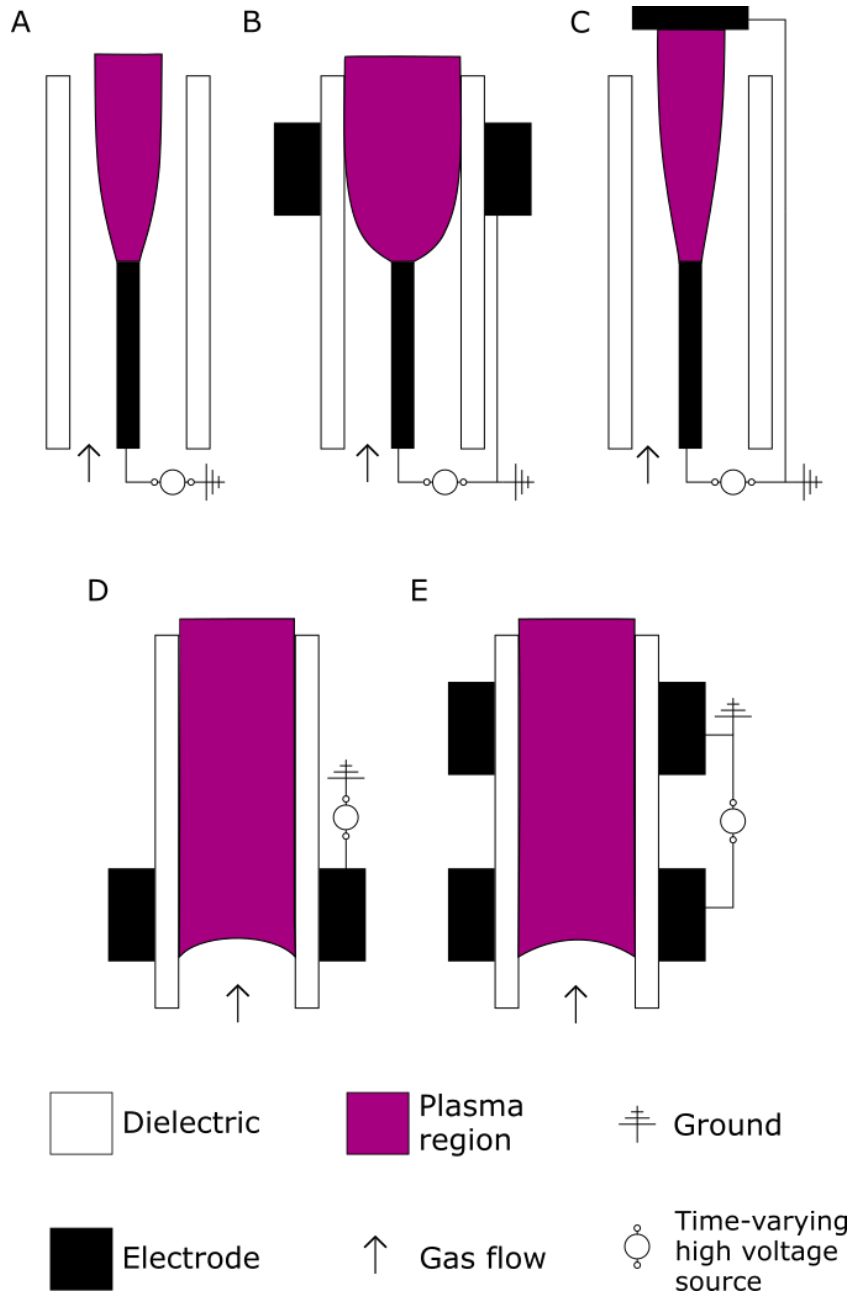

Figure 3: Cross-sectional views of commonly used low-temperature plasma jets configurations.

Specific applications require custom variations of the typical APPJ discharge configuration; for example, APPJs developed for applications in endoscopy require meter-long flexible capillaries to produce a stable column of plasma.[39–47] For applications where power consumption is a concern or additional safety is required, an APPJ with a dielectric-covered pin electrode can generate a discharge with similar properties to those with an uncovered pin

electrode configuration at much lower power.[48] Safety is crucial for medical treatment; the kINPen MED was the first APPJ accredited as a medical device with certified electrical safety. This plasma source serves as a standard for biomedical studies.[49]

A downside of APPJs is the relatively small area of treatment covered by the plasma, which is typically on the order of a few mm^2.[50] It represents a challenge to the scalability of the discharge. It thus limits its potential for large-scale applications. To overcome this problem, multiple APPJs can be combined into arrays to maintain the advantages of a single APPJ while simultaneously increasing the treatment area. In some studies, each APPJ in the array has an individual gas feed,[51–54] while in others, all the jets share a single gas feed,[51–53,55–57] both expand the plasma-target area of contact. A drawback of arraying multiple APPJs is gas consumption, which can quickly become prohibitively expensive when noble gases are used. Furthermore, due to the electrical characteristics of the plasma column emerging from each capillary in an APPJ array, the interaction between discharges is inevitable. Several studies have shown that individual plasma columns within an array can either repel or attract each other depending on their characteristics, acting to reduce treatment uniformity downstream.[51,58]

1.5 Plasma jet design and plasma generation

The plasma was generated with a kHz excited DBD jet at atmospheric pressure in this work, shown in Figure 4. A coaxial configuration is composed of a powered pin electrode and a grounded ring copper electrode, the former situated in the dielectric capillary and the latter fixed on the outer of the capillary. The copper ring is at a 5 mm distance from the exit of the jet, and the pin electrode is situated 5 mm upstream from the ring electrode.

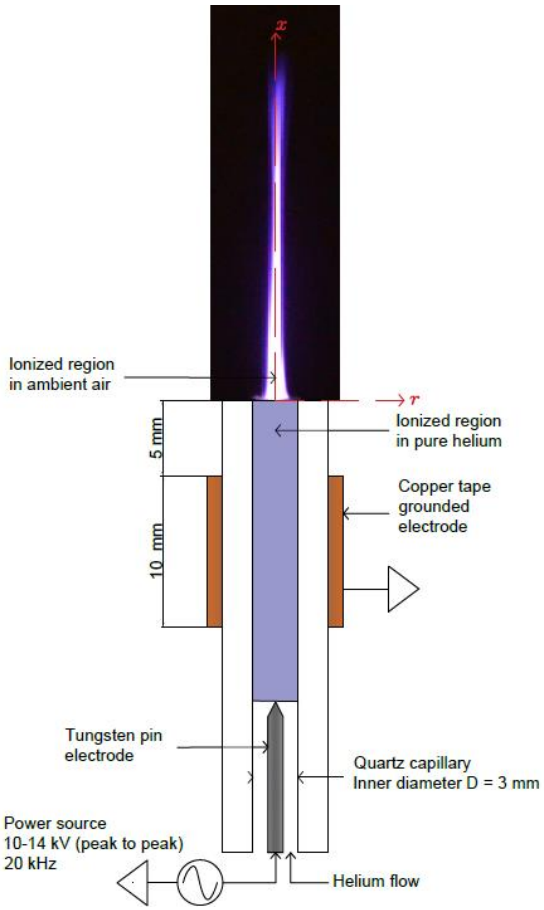

Figure 4: Sinusoidal driven atmospheric pressure non-thermal plasma jet configuration schematic.

When APPJs are in operation, in kHz excited DBD jets, a continuous luminous plasma plume can be seen by the naked eye; however, such observations do not show the true nature of the discharge. Using short-exposure imaging techniques, the plasma plume has been revealed to consist of a sequence of IW propagating at high speeds in the order of 10^5 – 10^8 $cm.s^{-1}$.[59–62]. IWs are present in dielectric barrier discharges, where ionisation occurs in a small volume that changes position over time. This volume is characterised by a strong electric field, which energises electrons and leads to dissociation and ionisation of the feed gas by electron impact.

Ionisation waves, also known as plasma bullets, are ignited near the driven electrode when the externally applied electric field exceeds the breakdown voltage in the feed gas[62–69]. They propagate towards the grounded electrode and create a conductive channel connecting the bullets to the powered electrode.[70,71] During this time, the dielectric surface at the grounded electrode accumulates surface charges; these charges induce an electric field that opposes the applied electric field.[72] This phenomenon hinders the discharge as the total electric field is decreased; thus, the discharge stops the presence of the dielectric limits the transition of the discharge into a spark or arc. The discharge is maintained in the non-thermal regime due to the limited amount of charge and average current density.[72] The use of a pin electrode allow the generation of a stronger electric field that peaks at the extremity of the pin. Moreover, when the discharge is initiated, the electron surface density has a maxima at the same point. The electron temperature has a maxima at the closest surface of the dielectric to the pin.[73] The dielectric capillary serves as a guide for the IW propagation,[74] the IW expands radially and propagates in a hollow emission distribution that peaks near the capillary inner wall, what is known as the "wall-hugging" mode.[75] When propagating in the feed gas outside of the capillary, the IWs initially keep the doughnut-shaped structures. Their shape then progressively changes to a 'homogenous' structure as they propagate downstream due to air diffusion into the feed gas flow.[62] IW propagation mechanisms can differ in more complex electrode configurations, such as propagation in a long flexible capillary or a glass loop, which showed the IW tended to hug one wall due to curvature.[47,76]

The electric field supports the propagation of the IW; thus, the voltage pulse duration (or period in the case of sinusoidal excitation) is a key factor in the propagation length. As IW's continue to propagate, the finite conductivity of the plasma channel weakens the electric field until they arrive at a position where the direct ionisation rate drops as a result of changing gas

composition and weakened electric field. This typically occurs at a distance of a few centimeters downstream from the capillary orifice, depending on flow rate and capillary diameter.[63]

1.6 Thesis outline

This thesis is presented in seven chapters. Chapter one provides a brief introduction to general plasma science and DBD jets in particular; the challenges and objectives of the work were also presented. Chapter two provides a comprehensive review of the current literature surrounding atmospheric pressure plasma jets, focusing on plasma physics, fluid dynamics, chemistry, and selected applications. Chapter four describes the experimental techniques and computational models used to characterise plasma jet behaviour. Chapter four provides quantitative measurements of an APPJ using PIV. Chapter five combines PIV, Rayleigh scattering, and LIF measurements made on a sinusoidal driven APPJ. The consequences of the plasma-induced turbulence on air entrainment and gas mixing are measured. These novel results link the crucial physicochemical properties of the plasma to fluid dynamics. Chapter six focuses on the influence of the plasma generation parameters on a pulse-driven APPJ in terms of their impact on the fluid flow structure. Finally, chapter seven summarises the main results and conclusions of the thesis while providing an outlook on future investigations.

Chapter 2 Background theory and relevant literature

In this chapter, the theory and literature relevant to studying the physicochemical aspects of an atmospheric pressure plasma jet are discussed. The chapter contains an overview of the IW generated inside the capillary. The fluid dynamic background of a jet impinging into a resting medium, defined as a free submerged jet, and an insight into the complex interaction between the plasma physics, fluid dynamics, and the chemistry related to the plasma species reacting with ambient air.

APPJ's are the focus of an intense international research effort due to their unique chemical and physical characteristics.[20,49,77,78] A defining aspect of the plasma jet is the interplay between plasma physics, plasma chemistry, and fluid dynamics, which ultimately dictate application efficacy. Plasma jets can be constructed using various electrode configurations and powered using a plethora of high voltage power sources (with frequency ranging from DC to GHz). A vast array of gases has also been investigated, ranging from noble gases such as helium and argon to complex gas mixtures. In the context of biomedical and healthcare-related applications, perhaps the most common plasma jet configuration is based on the dielectric barrier discharge operating in a noble gas. It allows for generating a stable flux of plasma species downstream of the high-voltage electrodes with minimal risk of arcing[14]. Given the widespread use of the DBD jet configuration for healthcare-related applications, it is chosen as the primary focus.[49,78]

The remainder of this chapter is divided into four sections. The first provides a discussion of the physical mechanisms giving rise to the fast IW or 'plasma bullet' phenomena typically observed. The second section provides information on gas dynamics and turbulence. The third section explores the interaction of the plasma jet with the quiescent background, with

a specific focus on a helium-free jet expanding in ambient air. The fourth section assesses the chemistry of a helium plasma jet impinging into ambient air and the main reactions in the production of OH species inside the plasma plume.

2.1 Fast Moving Ionisation Waves

The IW initiated at the powered electrode is guided by the dielectric capillary towards the jet exit; the electric field at the tip of the IW has a significant influence on its characteristics. For instance, the speed of the IW is directly correlated with the strength of the electric field at its tip; a strong electric field increases the velocity of the IW.[79] The electric field of the IWs decreases as they move towards the exit of the capillary, which is explained by electric potential screening as a result of surface charging of the inner walls of the capillary.[80,81] The electric field then increases when the IWs exit the capillary. This effect is attributed to the contraction of the IWs as they are moving away from the capillary, which strengthens the electric field by focusing the charge density of the IWs into a smaller volume,[4] leading to an increase in the IWs propagation speed.[79,82,83]

The polarity of the applied voltage driving the discharge influences the strength of the total electric field at the front of the IW. The presence of space charge induced electric field in the opposite direction of the Laplacian electric field associated with the electrode polarization. Figure 5 shows the influence of the polarity on the total electric field for a pulse-driven APPJ.[84] For positive polarity cases, the total electric field increases due to the addition of the external electric field and space charge-induced field.[84] In the case of negative polarity, the total electric field is weakened as the external electric field and the space charge induced field to subtract from each other, as highlighted in Figure 5.[84] In most cases, the space charge electric field has a higher transient amplitude than the Laplacian electric field. Moreover, standard

configurations with an input voltage on the order of a few kVs generate an electric field in the tens of kV cm^{-1}.[79,85] Bourdon et al. measured the peak value of the electric field along the plasma plume generated by a pulse-driven helium APPJ at 45 $kV.cm^{-1}$, which is in agreement with computational modelling predictions.[81] The generation of strong external electric fields was revealed to be of interest when treating cell membranes since they can be charged capacitively to induce apoptosis. Electric field strengths in the range of 10-100 $kV.cm^{-1}$ influence the membrane's field-dependent relative permittivity.[86] Maximum electric field values up to 170 $kV.cm^{-1}$ were estimated with computational modelling by Norberg *et al.*.[87] Begum *et al*. experimentally measured, with optical emission spectroscopy, the maximum local electric field of 95 $kV.cm^{-1}$ at 13 mm from the tube exit for a nanosecond pulse plasma pencil (4-8 kV, 500-800 ns, 4 kHz).[83]

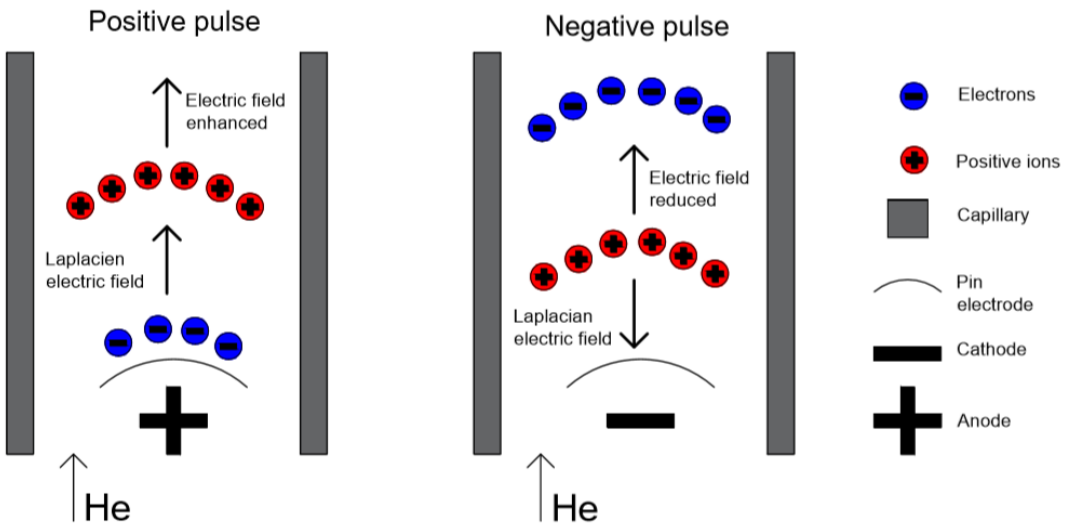

Figure 5: The electric field distribution with positive and negative pulses in a plasma jet.[84]

The propagation velocity of the IW can be decreased along the axis of propagation by placing a positively biased downstream ring or plate electrode. In contrast, the opposite effect can be induced by negatively biasing the downstream electrodes.[32,88] Simulations show that a negatively biased downstream electrode increases the electric field of the IW, thus, increasing

the propagation speed, whereas a positively biased downstream electrode reduces the electric field of the IW and causes a decrease in the propagation speed.[32] Wang *et al*. observed that the IW velocity decays faster as it travelled downstream when the pulse frequency increased from 1 to 3 kHz on a pulse-driven APPJ, although the peak velocity was unchanged.[22] They explained this effect by the increased number of charged species in the bullet head and faster recombination speed at higher pulse frequency. The increase of the pulse repetition rate produces an accumulation of charge deposition on the inner capillary or wall charging surface, affecting the plasma column by inducing an electric potential shielding.[70] This results in an observed increase of the propagation velocity of the IW, and thus, a longer plasma plume.[89] The addition of a dielectric target and the deposition of positive charge on its surface weakens the electric field. It encourages the streamer head into a radial propagation towards areas with a stronger electric field.[90]

The characteristics of IW's are also dependent on the feed gas, i.e., its composition and flow rate. The feed gas is usually helium or argon, although more exotic noble gasses and gas mixtures have been explored. The choice of feeding gas has a major impact on the physicochemical processes at play. For example, Penning ionisation in helium-fed APPJs increases the propagation speed of IWs, compared to that observed in argon for similar configurations.[24,91] While the flow rate does not directly affect the physical properties of the jet, it influences the mixing of impurities downstream of the capillary and thus can impact ionisation and attachment processes altering the charge density and the electric field distribution.[4,92]

The strong electric field in the ionisation wave originates from a strong charge imbalance. In cathode-directed IWs, positive ions dominate electrons and negative ions, while in anode-directed IWs, negative ions and electrons dominate.[93] The charged species move

under the influence of the electric field while colliding with the feed gas molecules, leading to a net momentum transfer from the charged species to the feed gas. This momentum transfer appears as an effective force known as the EHD force.[94] The EHD force has three components in terms of the physical mechanism involved, of which the dominant component is the electric field; it is also dependent on the charge density.[94] The impact of EHD forces in an APPJ has been investigated experimentally by Park *et al*. and computationally by Hasan *et al*.[60,95] Park *et al*. studied a helium APPJ driven by varying length voltage pulses, using a combination of experiments and modelling. They showed that the residual charge after the collapse of the IW also contributed to the EHD force.[60] The role of the EHD force is particularly interesting in the transition of the plasma jet into a turbulent state. Computational studies showed a role increasing the axial velocity inducing an earlier transition, while in comparison, the gas heating effect was considered too weak to influence the structure of the jet.[33]

The plasma plume length decreases for long pulse widths in the case of a pulse-driven APPJ.[96] Lu *et al*. showed a weak dependence between the plasma plume length and the electric field in the streamer head.[97] Additionally, the authors showed the importance of gas mixing in the effluent of the plasma jet on the plasma plume structure and chemistry. This observation, coupled with the measurements of plasma-induced air entrainment, hint towards the mixing prone behaviour of the plasma jet under specific electrical conditions.[98]

2.2 Gas dynamics and turbulence

Fluid dynamics is a very important topic to be understood; from weather forecasting to aerofoils, fluid dynamics has a wide spectrum of applications.[99] Amongst these, air flow applications are particularly used for ventilation, cooling, drying, etc. Air jets are easy to generate and have a strong ability to mix; thus, a strong knowledge is important to optimise

mass, momentum, heat exchange.[100] In fluid dynamics, the behaviour of the flow is governed by the ratio $\frac{inertial\ forces}{viscous\ forces}$ which defines the Reynolds number. The Reynolds number is used to determine the state of a fluid, laminar or turbulent, depending on the relative importance of the fluid momentum over the fluid stickiness.[99] The transition between laminar and turbulent flow can be considered in the context of its Reynolds number. It is commonly assumed that flows with a Re <2300 are laminar flow, between 2300 and 4000 is transitional flow, and flows above Re of 4000 are fully turbulent.[101,102] Flows with a Re <300 are considered very low in comparison. In a laminar flow, the viscous forces of the fluid are dominant, and the fluid motion is smooth. In opposition, the inertial forces dominate in a turbulent flow, and the fluid propagates chaotically.

For a fluid propagating in a capillary, the Reynolds number can be calculated as follow:

$$Re = \frac{\rho\, U_{eff} D}{\mu} = \frac{U_{eff} D}{\nu_v} = \frac{QD}{\nu_v\, A} \qquad (2.1)$$

Where *D* is the diameter of the tube (m), ρ is the density of the fluid (kg/m^3),

In low Reynolds jets, the flow in the capillary behaves in a laminar fashion, meaning a Gaussian velocity profile across the streamwise cross-section of the flow shown in Figure 6.

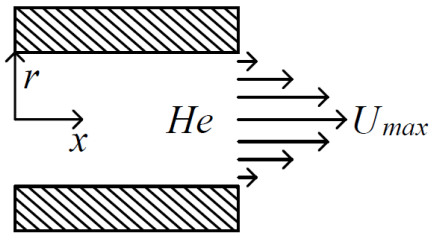

Figure 6: Schematic of a laminar flow at the exit of the capillary (own contribution).

The velocity profile in the tube as a function of the radius r is given by the Hagen-Poiseuille equation:

$$U(r) = \frac{\Delta P}{4\mu\Delta x}\,(R^2 - r^2) = U_m(1 - \frac{r^2}{R^2}) \qquad (2.2)$$

Where ΔP is the variation of pressure (Pa), Δx is the length of the tube (m), R is the inner radius of the tube (m), μ is the viscosity of the fluid $(Pa.s = \frac{kg}{m.s})$ and U_m (m/s) is the maximum flow velocity in the center of the tube at *U(0)*. The relation between the volumetric flow rate Q (m^3/s) and the velocity of the fluid in the tube is as follows:

$$Q = A \times U_{eff} \qquad (2.3)$$

Where A is the cross-sectional area (m^2). and U_{eff} is the effective velocity of the fluid (m/s). The cross-sectional area can be expressed as $A = \pi R^2$; thus, $dA = 2\pi r dr$. The volume flow rate Q becomes:

$$Q = \int U(r)dA = \int_0^R U_m\left(1 - \frac{r^2}{R^2}\right)2\pi r dr \qquad (2.4)$$

$$Q = 2\pi U_m\left[\frac{r^2}{2} - \frac{r^4}{4R^2}\right]_0^R = \frac{1}{2}\pi R^2 U_m = \frac{1}{2}U_m \times A \qquad (2.5)$$

The effective velocity U_{eff} is defined as follows in the function of the maximum velocity:

$$U_{eff} = \frac{U_m}{2} \qquad (2.6)$$

$$Q\,(\frac{m^3}{s}) = U_{eff}\pi R^2 \qquad (2.7)$$

$$Q\ (LPM) = U_{eff}\pi R^2 \times 60\ \times 1000 \qquad (2.8)$$

This final form is equivalent to the one obtained with the Darcy-Weisbach equation for the pressure loss in a tube due to the friction of an incompressible fluid.[102]

In a capillary, a flow is laminar if the Reynolds number is below 2300. An increase in velocity is required to reach this transitional value. A secondary velocity input could increase the velocity to reach this threshold. In a plasma discharge, the EHD increases the velocity of the travelling gas. Whalley and Walsh estimated an increase of the maximum velocity U_m by <2.5%.

Additionally, the velocity increase due to the gas heating was estimated <9% of U_m for a Re < 400.[103] In this study, a velocity increase of up to 10% was observed. However, the choice of a very low Reynolds flow in the capillary requires a very strong velocity increase to reach the transitional threshold. A flow with a Re of 118 requires an increase in velocity by a minimum of 1950% to transition into a turbulent state in the capillary. However, the observed transitions of the plasma jet into a turbulent state are thus provoked through a different mean.

2.3 The link between fluid dynamics and atmospheric pressure plasma jet physicochemical properties

When a plasma jet is fed with helium, the flowing gas impinges into ambient air, and both fluids can be considered incompressible. The absence of an obstacle in front of the jet characterises the jet as a free jet. A fluid impinging and spreading through a resting fluid defines it as a submerged jet and a variable-density jet.[104] A free submerged vertical buoyant jet schematic is presented in Figure 7. The potential core of the jet is at the exit of the orifice where the velocity is uniform and maximal (U_m); it diminishes gradually. Beyond, the shear layer is

identified by an evolutive velocity profile along the jet propagation axis. The potential core delimits this layer at the centre, and the jet edges, the shear layer at the exit of the capillary are particularly small in size and fragile.[103] These edges are in contact with ambient air and present a strong difference in velocity. In the potential core, the fluid may be considered inviscid, as the viscous effect is weak. The centreline velocity in the potential core is constant at U_m, whereas the mixing regions have large velocity and density variations.

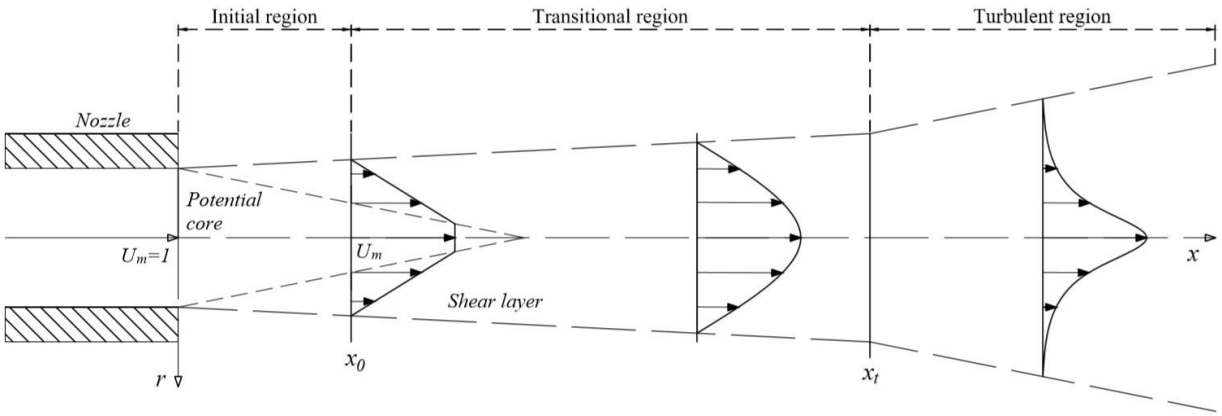

Figure 7: Free submerged jet schematic (own contribution).

The turbulent flow field of a variable-density jet can be characterised by momentum flux ratio to buoyancy flux. This ratio is defined by the dimensionless parameter called the Froude number, $Fr = U_m^2\rho_j / g\ D(\rho_a - \rho_j)$, where, U_m is the jet exit velocity, ρ_j is the density of the noble gas, ρ_a is the density of the ambient fluid, g is the acceleration due to gravity, and D is the inner diameter of the capillary. When the APPJ is orientated to generate a turbulent jet flow in the vertical direction, the developing flow field is divided into three distinct regions,[105] which are functions of increasing vertical distance away from the jet exit. First, there is a region of pure jet behaviour driven by momentum flux. At the end of the pure jet region, the fluid flow enters into an intermediary region where both the momentum flux and buoyancy flux play equally important roles. Finally, the jet flow is driven by buoyancy forces. Irregular

fluctuations of velocity and pressure characterise this turbulent region, where the turbulent fluctuations are random in nature.[106]

The velocity at the centre of the expanding jet evolves with a well-known trend displayed in Figure 8. It is composed of 3 parts; the initial region extending to the virtual origin x_0; the transitional region where the centreline velocity decreases; and the fully developed turbulent region where the centreline velocity stabilises. In the case of a jet where the disturbances are extremely small, the transition from laminar to the turbulent jet is a 'natural transition' which is caused by small and uncontrollable disturbances.[107]

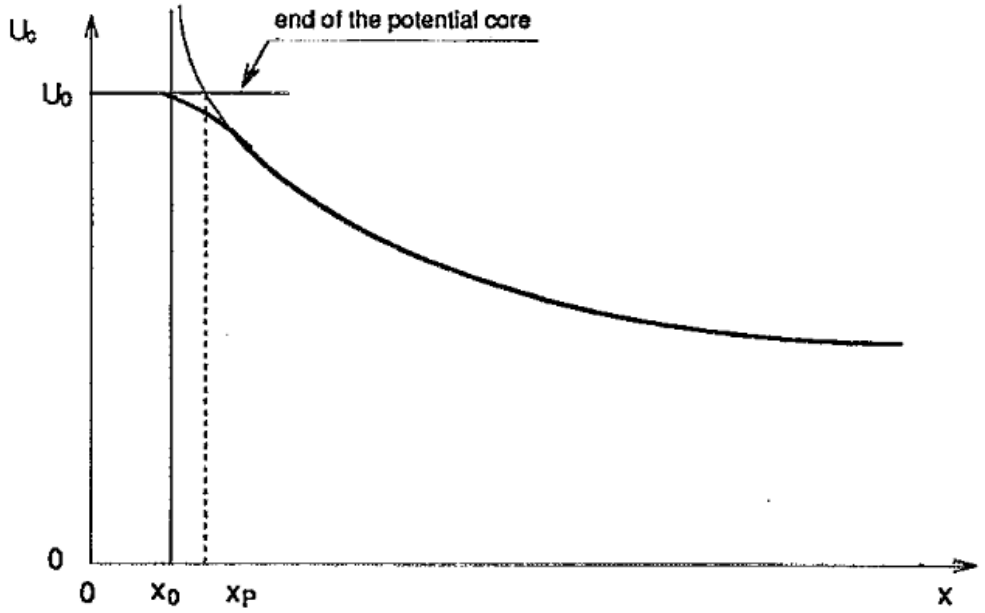

Figure 8: Velocity centreline of an expanding jet. With U_0 the initial velocity, x_0 the virtual origin, and x_p the potential core length.[108]

One important parameter is the Strouhal number which defines the relationship between the characteristic frequency, the amplitude, and the velocity; it has a wide range of utility, such as characterising the movements of birds,[109,110] insects,[109] dolphins,[109,111] the flow around

cylindrical cylinders,[112] or the perturbation of flow field.[113] To further understand the generation of turbulence, the observation of the distribution of disturbances in a shear layer of a jet at a large Reynolds number was investigated.[114–116] The growth rate of disturbances in the shear layer was thoroughly evaluated with artificially generated disturbances.[107,115,117–119] The experimental study of the Strouhal number on jet turbulence by Schlieren photography and hot-wire anemometry showed a preferred mode for a Strouhal number of 0.30.[120] Michalke showed a maximum amplitude of growth rate of small perturbations in a shear layer space-wise and timewise around a Strouhal number of 0.017.[119] Furthermore, experimental data gathered showed a range of Strouhal numbers between 0.013 and 0.023 for axisymmetric jets.[121] In the case of a low Reynolds number jet, instabilities are generated in relation to the Strouhal number.[35,107,122]

A considerable effort has been directed towards identifying the mechanisms that link the dynamics of the propagating plasma to the flow effects observed in the gas channel emerging from the jet orifice. Many studies have demonstrated that plasma generation in a flowing noble gas jet leads to an abrupt laminar-turbulent transition of the flow beyond the orifice. EHD forces and gas heating have been suggested as possible mechanisms to explain the dramatic change in flow dynamics. EHD forces are considered the dominant factor in kHz excited APPJ's.[103] The EHD force consists of a momentum transfer by the charged species under the influence of the electric field to the feeding gas molecules. In contrast, the gas heating process corresponds to the energy transferred from the elastic collisions between electrons and 'cold' neutral gas molecules. Notably, the predicted impact of these two phenomena on the flow velocity of the jet falls below the requirement to explain the observed reduction of the laminar region of the jet.[103]

Several studies have probed the interaction of the expanding plasma jet into a quiescent background via qualitative observations using Schlieren imaging.[2,3,27,35,123] The first PIV study of a free submerged axisymmetric plasma jet provided a fluid dynamic angle to characterise the plasma-induced turbulence phenomenon by Whalley and Walsh.[35] Both qualitative and quantitative methods confirm that the presence of a discharge generated at kHz frequencies within the flowing gas results in perturbation to the jet flow and the early onset of turbulence.[35,118,119,121]

To date, some of the most extensive research characterising the developing turbulent flow fields generated by an APPJ has been conducted by Whalley & Walsh.[35] High-speed Schlieren imaging and 2D PIV were used to investigate the developing turbulent flow fields within the pure jet region of a helium APPJ. Figure 9 shows instantaneous Schlieren imaging of a helium APPJ flow at a Reynolds number of $Re = U_m D/\nu_j = 135$, where ν_j is the kinematic viscosity of helium. The Reynolds number is a ratio of inertial forces to viscous forces present within the fluid flow and is an essential non-dimensional parameter used to describe the state of the flow (*e.g.* whether the flow is laminar, turbulent or in a state of transition-to-turbulence). Without plasma generation, Figure 9(a), the fluid flow remains laminar. However, the generation of a plasma plume, Figure 9(b), leads to an abrupt transition into a turbulent regime. These types of qualitative observations on plasma-induced turbulent jet flows are well-known within the APPJ community.[2,33,123] Generally, these turbulent flow fields have been observed in APPJ's with Reynolds numbers ranging from Re = 135 – 840 using both pulsed and sinusoidal excitation with applied voltages from 4 – 30 kV. The frequency of excitation is known to be an important parameter. Within the fluid dynamics communities, frequencies are often represented by the non-dimensional Strouhal number, $St = f_c\theta/U_m$, where f_c is a

characteristic frequency, θ is the momentum thickness of the shear layer at the jet exit, which characterise oscillations within the fluid flow.

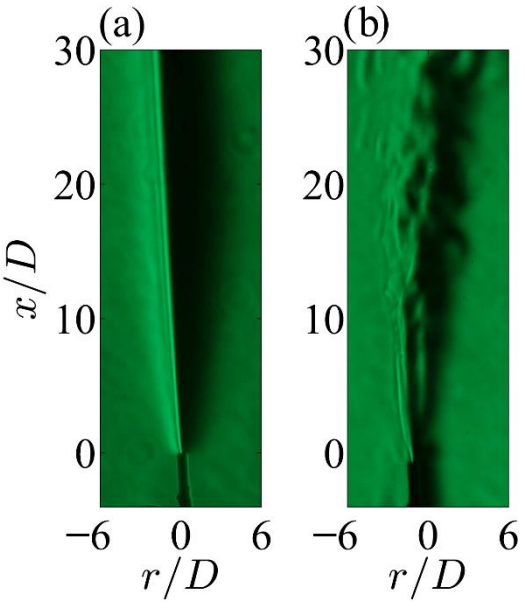

Figure 9: Schlieren photography of (a) helium jet flow at Re = 135 and (b-d) helium jet flow at Re = 135 with plasma ignited at (b) 16 kV.[35]

The shear layers (i.e., velocity gradients) at the jet exit are highly unstable.[122,124] Figure 10 shows a schematic of the generation of vortices along with an expanding free jet; The vortices are initiated in the shear layer of the jet and are expected to propagate and grow in intensity.[100] Similarly, the plasma-induced perturbations are expected to affect the fluid dynamic structure of the jet. Furthermore, small finite perturbations with amplitudes on the order of 10% of the mean jet exit velocity, which contains frequencies with a Strouhal number of $St < 0.04$, can grow exponentially in the unstable shear layers and laminar transition jet flows into turbulent regimes from a Reynolds number as low as $Re \approx 50$.[107,119,125,126] Linear stability theory[2,63,98,119,127,128] and many experimental observations[121] of, albeit, homogeneous (i.e., constant density) axisymmetric jet flows predict that small finite perturbations will amplify the most within the jet shear layers when they have a dominant excitation frequency corresponding to a Strouhal number $St \approx 0.017$. To put this into context, volume flow rates of a few standard-

litres-per-minute typical for APPJ flows through capillaries with internal diameters of a few mm's, typical dominant frequencies of 10's of kHz are to be expected, often coinciding with the frequency of plasma excitation.

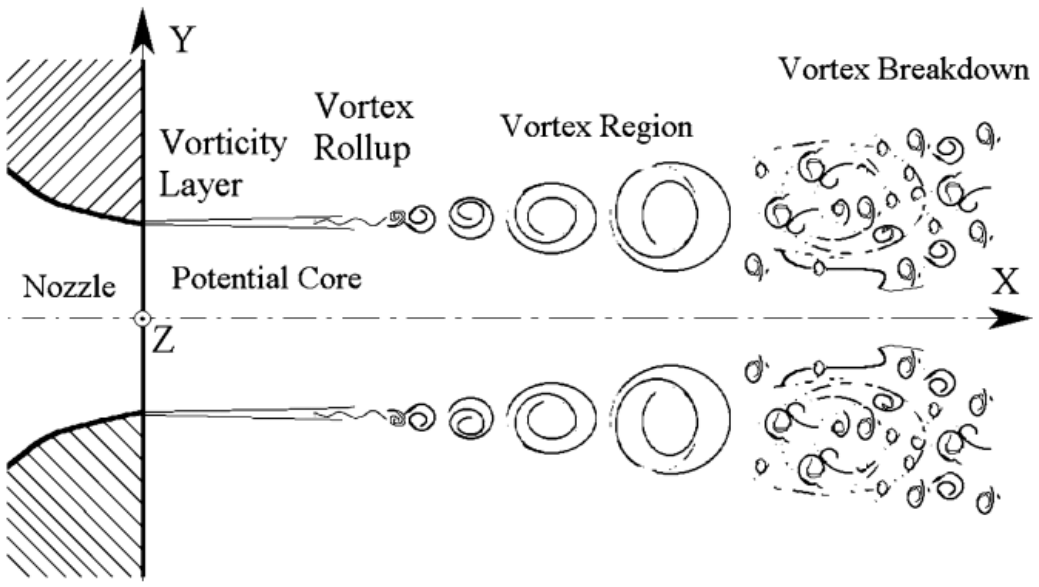

Figure 10: Schematic of a free jet flow expanding, with the generation of vortices along the jet.[100]

Global instability modes in low-density axisymmetric jets have been found with dominant frequencies on the order of 10's of kHz for APPJ flows.[129] Whalley & Walsh posited that the sudden onset of turbulence generated within an APPJ flow was due to a combination of small-amplitude electro-hydrodynamic body forces and gas heating causing perturbations in the unstable shear layers at the jet exit.[35] These perturbations are amplified as they travel downstream, causing velocity fluctuations, Reynolds shear stresses, and turbulence production. They estimated that the combined contribution of these perturbations could increase the mean jet exit velocity by up to 10% with an order-of-magnitude analysis. The evolution of an APPJ structure is described in Figure 11, where several sections are highlighted, the perturbations in the shear layer at the exit of the capillary (1), the instabilities initiating vortices (2), the

developed vortices (3), the strong alteration of the core structure in spade shape (4), and the completely altered structure (5).

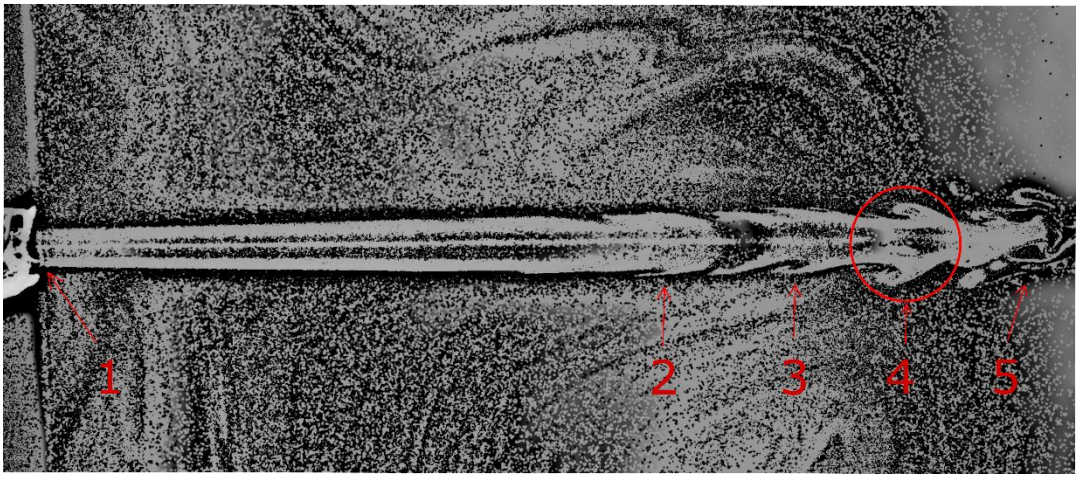

Figure 11: PIV picture of a seeded helium APPJ expanding in seeded ambient air (own contribution).

While many studies have considered the interaction of an APPJ and the quiescent ambient air, this typically does not correspond to a realistic usage scenario when an APPJ is used in a biomedical application. The plasma does not only interact with the background gas but also impinges on a target substrate. However, a downward directed helium jet bends upward due to the upward buoyancy force overwhelming the diminishing natural inertia of the flow. In the presence of plasma, the natural inertia of the flow is combined with the EHD. It counteracts the buoyancy force and allows the development of the APPJ downward onto a target.[5] Although the APPJ can be applied downward, the pulse repetition rate and the nature of the target are crucial factors in developing the structure of the jet.[3,5]

Boselli *et al*. used high-speed Schlieren imaging to observe a helium plasma jet with and without a target.[2] Their study showed that the fluid dynamics change between the plasma on and off cases, with instabilities noted in the plasma-on case. The generation of turbulent

structures was more visible with a metallic substrate than with a dielectric-covered metallic substrate. These observations were attributed to charge deposition on the dielectric surface limiting the current, whereas the conductive substrate behaved like a counter electrode, causing a dramatic shift in the discharge dynamics and likely resulting in less perturbation to the jet shear layer. However, Robert *et al.* and Darny *et al*. showed the reverse effect, where the APPJ was able to force an otherwise turbulent flow into a laminar transition similarly; however, the pulse repetition rate and the nature of the target played a crucial role in the eventual jet structure.[3,5]

Whalley & Walsh conducted a statistical analysis of 2D PIV data to characterise the APPJ flow downstream of the plasma plume.[35] They showed that the ensemble-averaged centreline velocity (U_c) of a helium APPJ flow decays at a constant rate independent of applied voltage and Reynolds number after the vertical distance from the jet exit, taking into account the density variations. In their investigation, the potential core (x_p) length was assumed to be negligibly small.[130] They also noted that the spread of the APPJ was approximately double the typical angle found in the literature,[108,131] which was most likely due to a low Reynolds number effect.[132]

A free submerged jet can be characterised by the velocity profiles across the mixing area. Using a pointwise quantitative measurement system such as PIV allows the calculation of the turbulent kinetic energy and the Reynolds shear stress through the calculation of velocity and turbulence components.

The first step in obtaining these parameters is to calculate the velocity along the x-axis U_x and the velocity along the r axis U_r.

$$\boldsymbol{U_x = \frac{(x_2 - x_1)}{\Delta t}} \tag{2.10}$$

$$\boldsymbol{U_r = \frac{(r_2 - r_1)}{\Delta t}} \tag{2.11}$$

As previously stated, Δt is the time for which the variation of position occurs—corresponding to the time delay between the laser pulses of the PIV system. The velocity magnitude U can thus be expressed.

$$\boldsymbol{U = \sqrt{U_x{}^2 + U_r{}^2}} \tag{2.12}$$

Using the Reynolds decomposition, the flow velocity field can be decomposed into a time-averaged velocity and a turbulence component[133].

$$\boldsymbol{U_x = \overline{U}_x + u_x} \text{ , and } \mathbf{U}_r = \boldsymbol{\overline{U}_r + u_r} \tag{2.13}$$

Where, $\overline{U}_x, \overline{U}_r$ are the time-averaged velocities and u_x , u_r are called the turbulence components and correspond to the deviation from the time-averaged velocity. A time average of a turbulence component is equal to zero.[133] To avoid this situation, Dryden and Kuethe proposed the definition of the turbulence intensity of the velocity fluctuations streamwise $\boldsymbol{u'_x}$ and radial $\boldsymbol{u'_r}$ by the root-mean-square value;[134]

$$\boldsymbol{u'_x = \sqrt{\overline{u_x{}^2}}}, \qquad \boldsymbol{u'_r = \sqrt{\overline{u_r{}^2}}} \tag{2.14}$$

To quantitatively express the flow field, averaging either time-related or space-related or both is necessary. The Eulerian description of the flow field averaging has three mathematical forms.[133]

The time average:

$$\bar{U}(x_0) = \lim_{T\to\infty} \frac{1}{2T} \int_{-T}^{+T} dt\, U(x_0, t) \tag{2.15}$$

The space average:

$$\bar{U}(t_0) = \lim_{x\to\infty} \frac{1}{2T} \int_{-x}^{+x} dt\, U(x, t_0) \tag{2.16}$$

The ensemble average of N identical experiments:

$$\bar{U}(x_0, t_0) = \frac{\sum_1^N nU_n(x_0, t_0)}{N} \tag{2.17}$$

In the case of a quantitative study using PIV, the spatial and temporal resolution allows for calculating the fluctuation's velocities. For a finite time interval, the intensity of turbulence fluctuations corresponds to the standard deviation of the streamwise or radial velocity at a specific position;

$$u_x' = \sqrt{\frac{1}{N}\sum_{x=1}^{N}(U_x - \overline{U}_x)^2}\ \left(\frac{m}{s}\right) \tag{2.18}$$

The turbulent kinetic energy *k* is the kinetic energy per unit mass of the turbulence fluctuations in a turbulent flow, calculated from the intensity of the turbulence velocity fluctuations along the x- and y-axis.

$$k = \frac{1}{2}(u_x'^2 + u_r'^2)\ (m^2/s^2) or\ (J/kg) \tag{2.19}$$

The Reynolds stress is defined as a part of the turbulent kinetic energy and expresses the production of turbulence P_T in the fluid. It is the product of the time-averaged intensity of turbulence fluctuations along both axes.

$$P_T = -\overline{\boldsymbol{u_x u_r}}\frac{\boldsymbol{\partial \overline{u_x}}}{\boldsymbol{\partial x_r}} \tag{2.20}$$

The production of turbulence is composed of the Reynolds stress component $R_{x,r,}$ and the shear stress term $\frac{\boldsymbol{\partial \overline{u_x}}}{\boldsymbol{\partial x_r}}$.

$$\boldsymbol{R_{x,r} = -\overline{u_x u_r}} \tag{2.21}$$

The elements presented are important in translating the velocity measurements into turbulence data. While the velocity measurements of an APPJ are novel, several techniques provided a strong addition.

2.4 Chemistry at the interface of the helium plasma jet and ambient air.

Noble gas plasmas are expected to have little chemical reactivity; however, impurities found within the feed gas (e.g., H_2O, O_2, and N_2) can give rise to various RONS. In this work, the chemistry is divided into two zones: in the idealised helium plasma jet and ambient air interface. The latter is the most important as the presence of air generates a very rich presence of species. The helium plasma jet extends from the pin electrode to the plasma plume. In the ideal case where the helium is 100% pure, the species present are He, He^*, He_2^*, He^+, He_2^+; they are obtained through two-body collisions, three-body collisions, recombination, electron-impact ionisation, metastable production, and vibrational excitation.[135] However, this case is

not realistic; the helium used in this work has a purity of >99.999% from the supplier with impurities of H_2O < 2 ppm, O_2 < 2 ppm, and N_2 < 4 ppm. While being in small quantities, these impurities participate in the chemistry in the capillary and the consequential chemistry in the plasma plume. The chemical reactions of N_2 and O_2 with He were studied by Bourdon *et al.* and Murakami *et al.*, respectively.[81,135]

One of the goals of this work is to identify the influence of plasma-induced turbulence and air entrainment on chemistry. Among all the species present in the plasma, OH is solely created by H_2O. In an ideal case, the presence of OH in plasma would be due to mixing at the interface plasma/ambient humid air or humid air entrainment.[136] However, the presence of impurities participates in the generation of OH.[136] Moreover, the OH in the plasma plume were mostly generated from the impurities by Yonemori *et al.* using LIF and particularly the transition $P_1(3)$ of OH. [136] Li et al. looked at an RF argon plasma jet, particularly the transitions $P_2(6)$, $P_1(4)$, and $P_2(3)$, they showed a similar conclusion that the OH generation happens in the plasma plume region, in addition, the highest density was obtained with 0.3% H_2O.[137] The addition of air hinders the generation of OH through decreasing H_2O^+ by the production of O_2^+ and other reactions of nitrogen and oxygen species with OH.[138] However, the humidity of the ambient air has a minor effect on the density of OH produced relative to the production from the impurities.[139] The effect of air entrainment from a humid ambient air would suggest an increase in OH production.

Beyond the jet capillary, the discharge is free to interact with the quiescent background gas (typically humid air), resulting in an abundance of reactive chemical species. While such interactions act to increase the reactivity of the plasma-generated species, the unpredictable composition of the ambient background gas can alter the physicochemical processes at play, reducing the repeatability of any downstream treatment. To understand and ultimately control

the composition of RONS within the plasma, considerably more insight is required into the complex interactions occurring beyond the capillary. While the physics of the plasma jet is now well understood, the impact of the quiescent background air on the physicochemical processes at play has been mostly overlooked due to the complexity of the interaction. Several studies have probed the interaction via qualitative methods, such as Schlieren imaging,[2,3,27,35,123] observing that plasma generation has a marked impact on the fluid dynamics of the system. Particle image velocimetry has been used to quantitatively study a free submerged axisymmetric plasma jet and characterise the plasma-induced turbulence.[35] Both qualitative and quantitative methods confirm that the presence of a discharge generated at kHz frequencies within flowing gas results in perturbation of the jet flow and the early onset of turbulence.[35,118,119,121]

Chapter 3 Methodology

In 2016, Whalley and Walsh published the first use of PIV on an APPJ expanding in ambient air.[103] They showed the velocity fields measured downstream of the jet and the similarity to traditional jets. However, the lack of seeding in the plasma plume debarred a complete measurement of the velocity fluctuations and the turbulence generated along the jet. This provided the context to investigate the early part of the plasma plume through a novel seeding method of particles in the jet. Moreover, the exit of the capillary and the laminar region are key in the generation of turbulence.[140] The plasma jet configuration chosen was close to the one presented by Whalley and Walsh.[103] The details of the experimental configurations and settings are described in this chapter. Firstly, the plasma jet configuration and power sources are detailed. Then the Schlieren photography and Rayleigh scattering technique are described. Finally, the Laser-induced fluorescence technique and calibration are developed.

3.1 Atmospheric pressure plasma jet configuration

An atmospheric pressure plasma jets design is of great importance to plasma generation. Its configuration consists of a dielectric capillary with externally/internally mounted electrodes. The first important factor to be considered is the choice of capillary diameter and material. The capillary diameter directly affects the plasma densities and the Reynolds number.[68] Moreover, consideration needs to be taken for experimental techniques such as PIV, which require the presence of seeding particles and limitations in the spatial resolution of the measuring equipment.

A dielectric material is an electrical insulator that can be polarized by an applied electric field. The slight shift of the electric charges in the dielectric induces a dielectric polarization. This polarization creates an internal electric field compensating for the externally applied electric field. The dielectric material must be chemically inert and have a low dielectric constant which is favourable for an electric field. Quartz is a good choice as a dielectric material for a DBD plasma jet configuration. Its chemical inertness prevents etching, its dielectric constant k of ~3.6, and a low dissipation of electromagnetic energy. The inner diameter selected was 3 mm, as 1 mm was unsuitable for PIV measurements due to spatial resolution, and 5 mm requires higher flow rates. The aforementioned factors were considered throughout the investigations presented in this contribution.

In PIV techniques, seeding particles are required in the measurement chamber, usually in the form of vaporised olive oil, which can influence the breakdown of the plasma. A tungsten pin electrode was implemented inside the quartz capillary at 15 mm from its exit throughout this contribution. The pin drives the discharge in both helium and seeded helium; it allows for lower driving voltages and minimises the risk of arcing[62]. Tungsten has low electrical resistivity and thermal conductivity, limiting the influence of heat transfer to the gas. Figure 12 shows the APPJ, along with its components used. The pin electrode was crimped with a copper terminal lug to facilitate the connection with the high voltage (HV) cable. A 3D printed support held the quartz capillary with the pin electrode at its centre and had a gas connection for the helium injection.

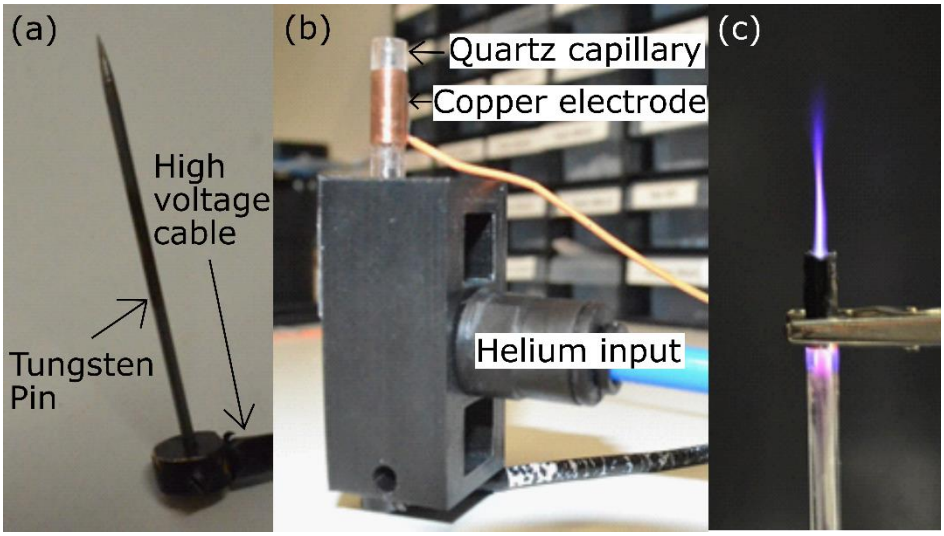

Figure 12: APPJ components; tungsten pin (a), 3D printed support with quartz capillary, tungsten pin electrode inside and a copper electrode near the exit (b), helium fed APPJ (c).

A thin film copper ring electrode with a width of 10 mm adhered to the outer surface of the capillary, 5 mm from its exit, and 5 mm from the powered pin electrode, to facilitate breakdown. The copper electrode was ***grounded*** for the study in Chapter 4 and served as a ***floating ground*** for Chapters 5 and 6.

The generation of the plasma discharge produces heat that transfers into the resting medium in which the jet propagates. To measure the influence of plasma generation on gas temperature, an Omega FOB100 fibre-optic thermometer was used. The dielectric temperature probe was positioned in the plasma at various points downstream of the jet orifice, and the temperature was recorded. The temperature was found to vary little with spatial position, with a maximum of 10 K above ambient located close to the capillary orifice; such observations are in line with previous studies.[103] The effect of the temperature is assumed overall constant, as the measurements were not 'cold-start,' meaning that the discharge was initiated before the measurements. The relative humidity of the air was measured at 40.00% ± 2% at 23.5°C ± 0.5°C with the AM2302 (wired DHT22) temperature-humidity sensor. The influence of the

relative humidity being close to constant in the laboratory was considered negligible on the plasma discharge and jet behaviour.

3.2 Power-source

A homemade power source was built to generate a sinusoidal high voltage output. The custom power supply role was to change the DC input signal into an AC signal with a considerable increase of voltage and control over the frequency. The inputs were generated with a DC power supply (ISO-TECH IPS 603) and a function generator (TG2000 20 MHz DDS). The outputs connect to a high voltage probe (Tektronics P6015A, 75 MHz, 20 kV, 1000:1) which in turn connects to the tungsten pin electrode. The waveforms of the high-voltage sinusoidal signal shown in Figure 13 were measured with a high voltage probe and were recorded with an oscilloscope (Tektronix DPO 5054 500 MHz 5 GS/s). Throughout this contribution, the applied voltage considered is the applied peak-to-peak voltage. The applied voltage was in the range of 10-14 kV peak-to-peak and a frequency of 20 kHz. The frequency was chosen close to the resonant frequency of the power source. The plasma generation was obtained with a minimum applied voltage of 8 kV peak-to-peak with a sinusoidal waveform. However, for the plume to be consistent in intensity and shape, a minimum of 10 kV peak-to-peak applied voltage was preferred.

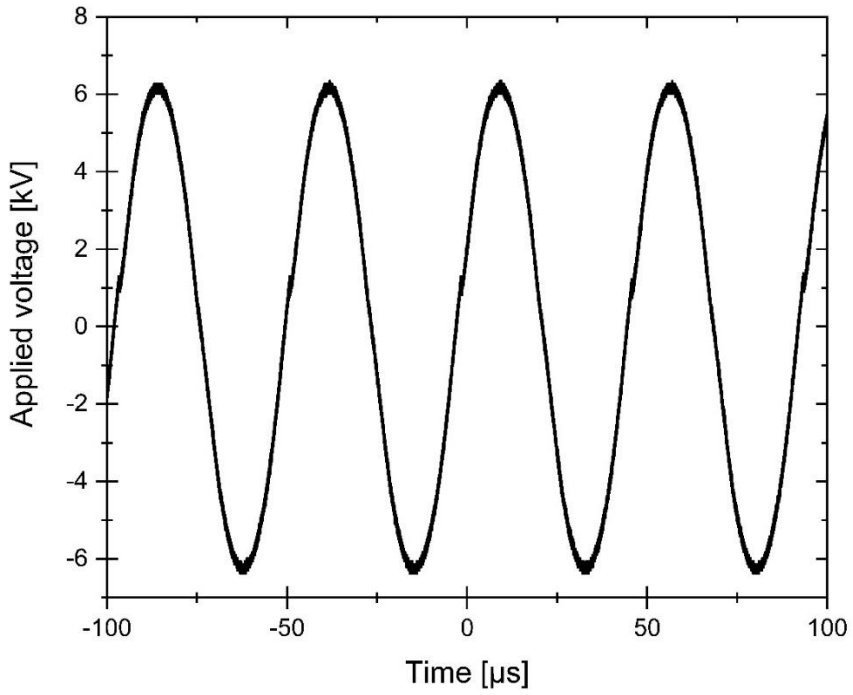

Figure 13: Sine applied voltage waveform with plasma on.

The discharge current (and consequently power) was not measured. A current probe placed between the power source and jet electrode showed the characteristic 'current spike' of a DBD jet superimposed on a sinusoidal displacement current. However, the signal intensity was too low to obtain a reliable measurement. The power sent into the plasma source was measured with the DC power supply to be in the 5 – 10 W range depending on the output voltage.

A secondary homemade power source permitted the generation of positive and negative pulses. The input was generated with a high voltage DC power supply (EK series 600W regulated high voltage power supply). The top hat signal with a high voltage probe (Tektronics P6015A, 75 MHz, 20 kV, 1000:1) was recorded using an oscilloscope (Tektronix 5054, 500 MHz, 5 GS/s) and shown in Figure 14. The inability to measure the current signal did not allow the calculation of the applied power. The input power in the high voltage power source was

kept constant at the average value of 35W. It was composed of an input voltage of 6.3-6.7 kV and input currents of 5.2-5.5 mA. The repetition frequency was controlled with a pulse generator (Thurbly Thandar Instruments TGP110 10MHz) in the range of 8-15 kHz, and pulse widths were kept in the duty cycle range of 0.2 – 80%.

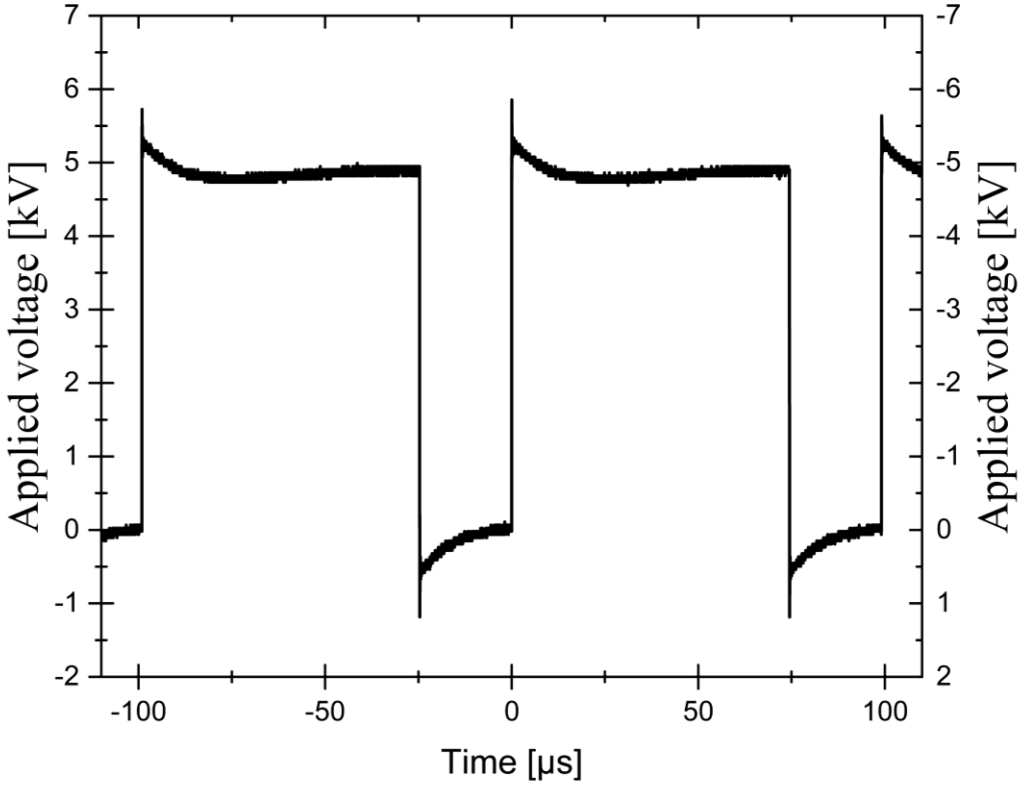

Figure 14: Positive and negative pulse applied voltage waveform with plasma on.

3.3 Schlieren photography

Schlieren photography is a qualitative technique for visualising density inhomogeneity in a flow. The changes in the fluid density and thus changes in the refractive index are translated into a variety of light intensity captured by a camera. A point-shaped light source emits a collimated light through the flow under consideration. An image of the light source is formed on the knife-edge positioned at twice the focal distance of the curved mirror. The light refracts

differently due to the density gradient, showing lighter and darker areas due to positive and negative gradients.[7]

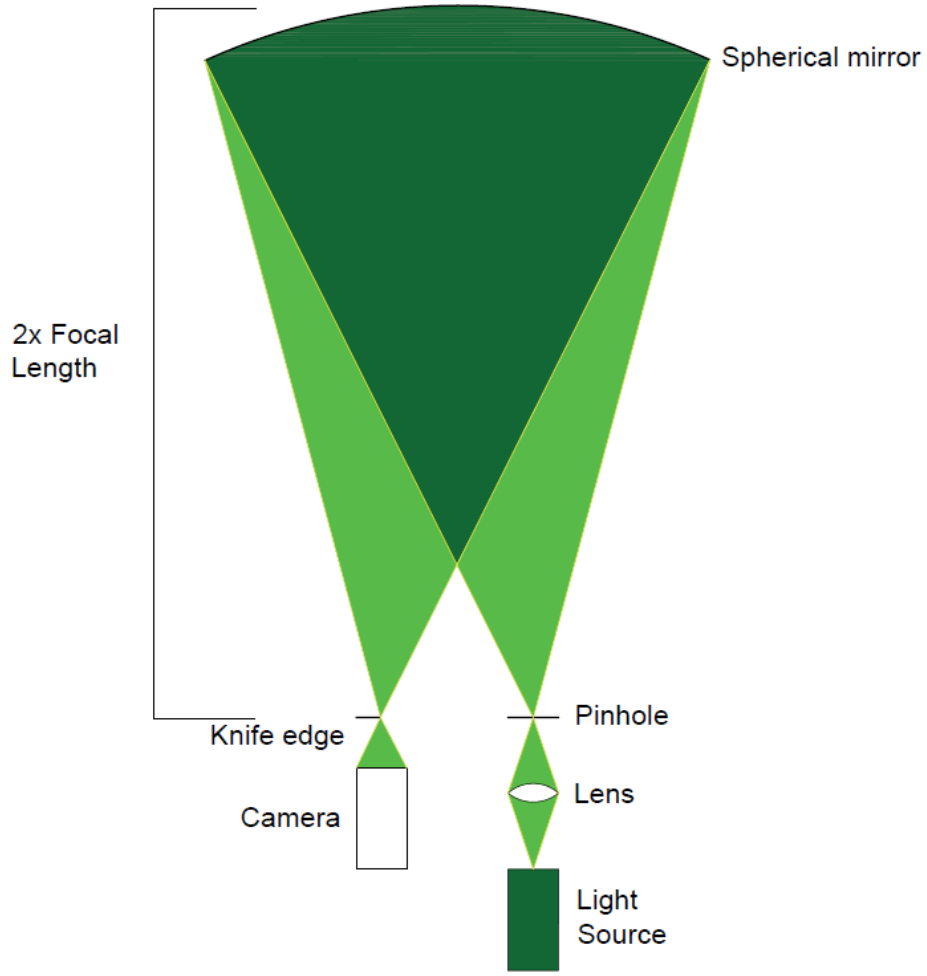

Figure 15: Schlieren Photography configuration schematic.

The Schlieren photography configuration has a simple setup, as described in Figure 15. The configuration requires a camera, a collimated light, a converging bi-convex lens (diameter 9 mm, a focal length of 20 mm), a knife-edge, and a curved mirror. For the light source to be point-shaped, a converging lens focuses the light source on a pinhole. The collimated light is focused on the position of the knife edge. The distance between the knife edge and the mirror is two times the mirror's focal length, equal to 4.87 m.

This qualitative study does not provide new data; however, it serves as a calibration tool to pick the correct flow rates and input voltages for the plasma jet configuration. There are

benefits to using this visualisation technique to validate the jet parameters. It is a convenient setup and serves as a base to compare to, especially with seeding in the PIV experiment.

3.4 Particle image velocimetry system

Particle image velocimetry is a non-intrusive laser measurement technique for research and diagnostics of fluid flows. It consists of an illuminated flow field seeded with particles of nominal size in the order of microns within a thin light sheet. The recording device captures dual images separated by a short time interval using a synchronisation between the camera and the laser pulses. This enables the determination of two in-plane components of the velocity by fragmenting the image into many interrogation areas; and then using a cross-correlation analysis technique, described in section 3.3.2.

The exciting aspect of PIV that concerns the study of atmospheric pressure plasma jets is its ability for time- and space-resolved measurements on two components of the velocity. This brings more valuable insight into jet flow mechanics over unsynchronised and pointwise velocity measurement techniques. Moreover, the non-disruptive aspect is fundamental not to perturb the flow and the plasma discharge.

This technique allows tracking particle movements in a defined volume using pulsed lasers with a time delay between the pulses as low as 1 microsecond. An enclosure is filled with seeding particles, in this case, it is vaporised olive oil, and then two pulsed lasers illumine the target area with an expanding beam. The High-speed camera is set at a 90° angle (perpendicular) to the light sheet and captures each laser light pulse in separate images.

After the capture phase of the flow in motion, the vital next step is the digital image processing phase. It contains all the operations done on the frames until the extraction of the

velocity components. It can be described in three steps pre-processing, processing, and post-processing; The first step, pre-processing, relates to image restoration (repairing undesirable effects) and image enhancement (contrast, suppression of background). The second step is processing the frames to generate velocity vectors; this follows a cross-correlation analysis method described below. The final step of post-processing contains the operations done, the generated vectors (filtering, etc.).

PIV measurements are sectioned into two categories; low-image-density PIV, where the distance between particles is much larger than the displacement, and high-image-density, where the distance between particles is smaller than the displacement. In this study, the latter is used; however, the higher density creates ambiguity for matching pairs between two frames; thus, it becomes necessary to use a statistical approach. This involves spatial correlation analysis, where the multiple potential pairs in the interrogation area are given a probability.

As PIV relies on the scattering of light off seeding particles suspended in the studied fluid, the nature of the particles is critical. They need to be non-toxic, non-corrosive, non-abrasive, non-volatile, and chemically inert not to alter the experiment. The accuracy of the PIV technique is closely linked to the ability of the particles to follow the fluid motion accurately. Thus a compromise must be evaluated between reducing the particle size to augment the flow tracking properties and increasing the particle size to improve light scattering.[141,142]

Table 2: The scattering cross-section as a function of the particle size.[141]

Diameter d_p	Scattering cross section C_s	
Molecule		$\simeq 10^{-33}$ m^2
1 μm	$C_s \simeq (d_p/\lambda)^4$	$\simeq 10^{-12}$ m^2
10 μm	$C_s \simeq (d_p/\lambda)^2$	$\simeq 10^{-9}$ m^2

The scattering cross-section depends heavily on the size of the particle, as shown in Table 2. The scattering from particles with size from 1 to 10 μm are ideal for use in PIV; however, in this range, various types of seeding are being used.[141] For sufficiently small particles, the tracking capability of suspended particles in a fluid flow is influenced only by the particle shape, diameter d_p, particle density ρ_p, fluid density ρ_f, and fluid viscosity μ or kinematic viscosity ν_v = μ/ ρ_j. Other external forces such as gravitational, centrifugal and electrostatic are considered negligible.[141] The Stokes number (S_k) characterises the behaviour of particles suspended in a fluid flow; it defines the tracing accuracy. The Stokes number is a characteristic non-dimensional frequency of the particle response. One way to express this parameter is a relationship between a characteristic time of the particle (such relaxation time), a characteristic dimension of an obstacle (the diameter of an obstacle), and the velocity of the flow.

$$S_k = \left(\frac{\omega}{\nu_v}\right)^{\frac{1}{2}} d_p \qquad (3.1)$$

Equation (3.1) defines the Stokes number; this value characterises the behaviour of the particles, where ω is the angular frequency of the turbulent motion, d_p is the particle diameter, and ν_v is the kinematic viscosity. An $S_k \geq 1$ means a poor tracing ability from the particle, mainly through an abrupt velocity change. Whereas for $S_k \leq 1$, the particles will follow the flow closely. Ultimately, $S_k < 0.1$ indicates a high accuracy at following the fluid flow.

With this definition, the Stokes number of various types of seeding is shown in Table 23. Olive oil droplets were chosen as the seeding for the PIV measurements in this study for some reasons: they are convenient to generate; low cost; entirely usable at ambient temperature; have a uniform size of 1-2 μm, which is in the cross-section range; and have a Stokes number lower than 0.1 (Table 3).

Table 3: Particle response in a turbulent flow.[141]

Particle	ρ_p (kg m^{-3})	Gas (10^5 Pa)	Density ratio s	Viscosity ν (m^2 s^{-1})	f_c (kHz)	Sk_c	d_p (μm)
TiO_2	3500	Air (300 K)	2950	1.50×10^{-5}	1 10	0.0295	1.44 0.45
Al_2O_3	3970	Flame (1800 K)	20250	3.00×10^{-4}	1 10	0.0113	2.46 0.78
Glass	2600	Air (300 K)	2190	1.50×10^{-5}	1 10	0.0342	1.67 0.53
Olive oil	970	Air (220 K)	617	1.45×10^{-5}	1 10	0.0645	3.09 0.98
Microballoon	100	Air (300 K)	84.5	1.50×10^{-5}	1 10	0.1742	8.50 2.69

The time-resolved PIV system from TSI Incorporated is shown in Figure 16. The measurements were taken inside a large, sealed chamber seeded with oil droplets with a nominal size of 1 µm. The chamber ensured that any external draughts did not influence the plasma jet flow. The seeding follows the flow closely as the Stokes numbers in this study were < 0.1, with tracing errors being < 1%.[7] A double pulse frequency-doubled Nd:YLF laser operating at 527 nm with a pulse duration of 100ns was used to generate a 1 mm thick light sheet projected into the seeding chamber and across the plasma jet orifice. A high-speed Phantom Miro Lab 340 camera was positioned outside the seeding chamber perpendicularly to the laser sheet and synchronised with the lasers such that each frame captured a single laser pulse. The configuration uses frame-straddling to achieve a short delay between frames; it entails triggering the first laser pulse at the end of the exposure time of one frame and the second pulse at the start of the exposure of the second frame, described in Figure 17. t_0 is the starting time of the capture of a set of two frames, Δt is the delay between the two laser pulses, and f is the frequency of the acquisition. The PIV system allows adjustment of the frequency of acquisition between 200 Hz up to 1 kHz.

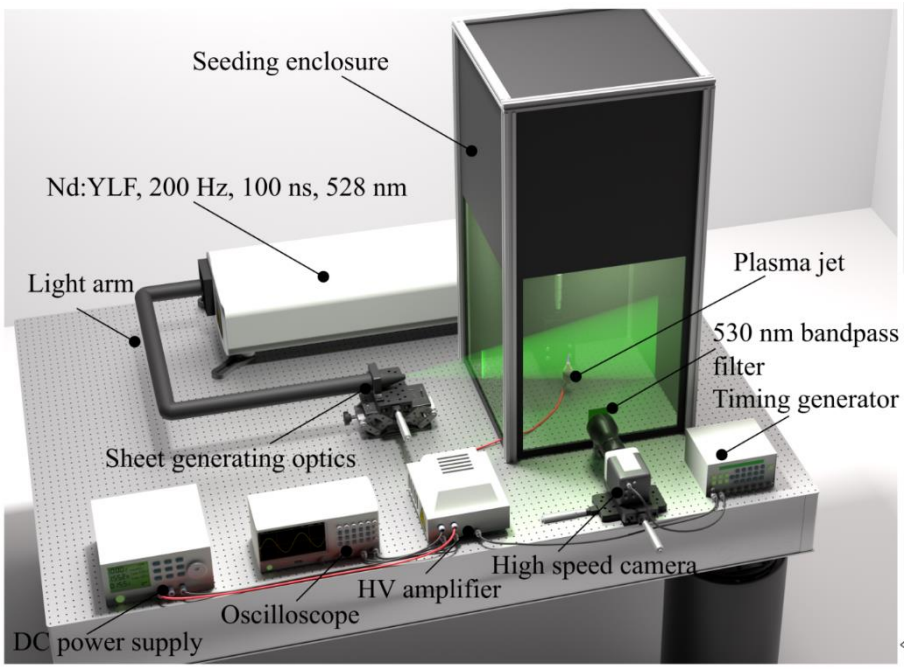

Figure 16: Particle image velocimetry setup.

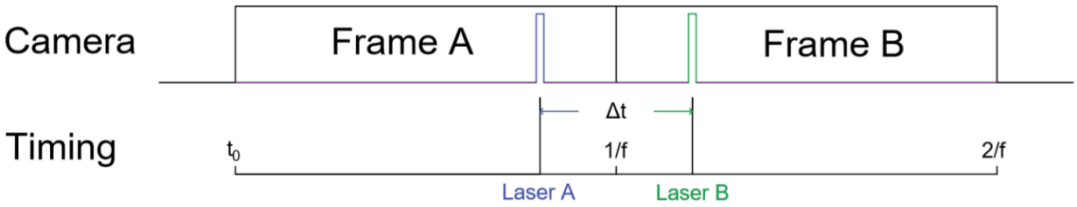

Figure 17: Particle image velocimetry capture schematic.

An oil droplet generator (Model 9307-6) from TSI was used to generate the seeding particles (oil droplets) in the chamber. It consists of an Atomizer optimised for the generation of olive oil droplets. It allows the generation of enough seeding to fill the enclosure with a volume > 2 m^3 and a reasonable size distribution. The atomiser consists of a reservoir of olive oil, drawn into a vertical section before being atomised onto a wall to remove large droplets and excess fluid. Compressed air then transports the particles to the exit of the generator and into the PIV chamber. The influence of the seeding particles in the PIV chamber over the generation of plasma or the flow behaviour is seen as negligible. The seeding particles follow the motion of the flow closely, and the helium flow pushes the particles away, which poses a

major challenge for PIV measurements on a plasma jet. An absence of seeding particles results in an erroneous calculation of vectors by the PIV software. Many possible solutions to seed the actual helium flow without influencing the plasma generation characteristics were investigated to overcome this challenge.

Based on the earlier works of Whalley and Walsh, it was known that an insufficient number of seeding particles were entrained within the laminar region of the jet to obtain reliable PIV measurements.[103] Thus, the first challenge was to provide a reliable solution of depositing seeding particles in the jet. As shown in Figure 18(a), the jet flow pushes all the seeding particles already present in the enclosure away, demonstrating the aforementioned challenge. To find a solution, multiple components were considered for seeding the feed gas, such as solid dielectric particles, olive oil particles, glycerine smoke, and ultrasonic humidifiers. Each approach produces particles that will affect the plasma discharge to some degree and follow the flow differently. Also, the particle size distribution needs to be reliable. After searching and testing many different approaches, the single jet atomiser from TSI served as the most reliable method of seeding the jet.

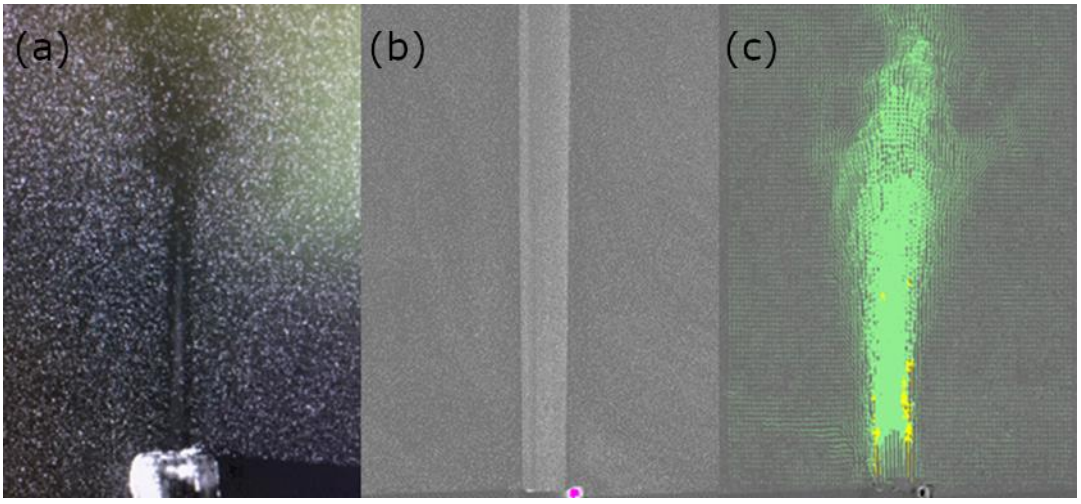

Figure 18: Picture of unseeded (a) and seeded jet (b) with processed velocity vectors (c).

The same type of olive oil used to seed the enclosure was used in the atomiser for practical and consistency purposes. Initially, the helium was directly injected into the atomiser and exited through the dielectric capillary of the plasma jet. However, the single jet atomiser required a minimum flow rate to produce seeding particles, limiting the range of available flow rates to generate the plasma jet. The minimum flow rate was much higher than what was desired for plasma jet experiments, resulting in a fully turbulent flow at the lowest possible flow rate. To overcome this challenge, the exit of the atomiser was directed into a secondary chamber, where a portion of the seeded gas flow was exhausted through an external extraction unit, enabling much lower flow rates to be directed through the plasma jet.

Ultimately, it was determined that a single jet atomiser (Model 9302) from TSI filled with olive oil could be used to seed the jet with minimal influence on the plasma jet characteristics. Helium gas with a purity of 99.999% fed the atomiser; the seeded gas is then directed towards the quartz capillary. The addition of oil droplets to the helium gas flow can disrupt the discharge; while such changes are difficult to assess, the breakdown voltage and length of the plasma plume were found not to change significantly.

While the seeding allowed the use of the PIV and permitted the capture of quantitative data, it was also an issue. Over a long experimental campaign, it was found that the concentration of seeding in the box decreased over time due to the box not being perfect and slight variations in the amount of helium injected into it. To avoid this, seeding was injected into the chamber before each experimental run, to improve repeatability.

While going into the jet, the seeding concentrated on a more complex issue than the seeding going into the chamber. The concentration was important as the inner diameter of the tube was only 3 mm, thus having too many particles made it hard to differentiate them; the

concentration had to be reduced. Also, the difference in intensity between background seeding and jet seeding was significant, becoming an obstacle for the cross-correlation analysis in the mixing layer between the flowing and quiescent gas. To prevent this situation, a secondary helium flow at a much lower flow rate was injected into post-seeded helium to dilute the seeding density. A picture highlighting a well-seeded jet is shown in Figure 18 (b); where the seeding of the jet can only just be distinguished from the background, the post-processing analysis of a turbulent jet showed reasonable results, Figure 18 (c).

While the detection was one issue, the plasma generation could easily be affected by dense seeding. It was difficult to draw a good comparison between the no-seeding and a seeding case, as the PIV cannot work without seeding. A picture of the plasma plume with an input of helium of 4 SLM is shown in Figure 19. Plasma generation with a high concentration of seeding in the helium influenced the plasma plume length resulting in a reduction of 14 mm for a 10 kV and 12 kV applied voltage. The reduction is less for the 14 kV case. Moreover, the captured intensity differs between the two cases. This observation indicated that the minimum possible seeding density to obtain accurate PIV data should be used in the feed gas flow.

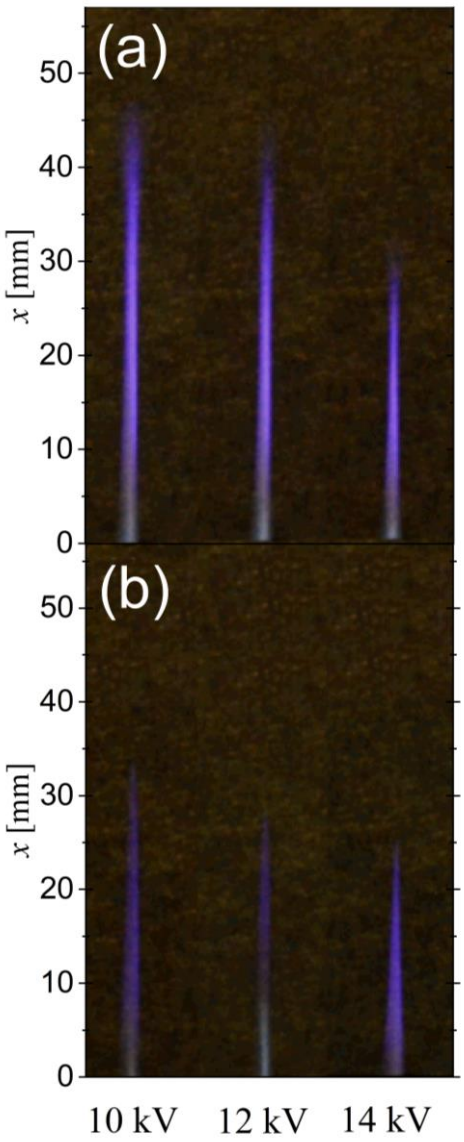

Figure 19: Comparison of plasma plume length and intensity for a sinusoidal driven helium APPJ with an input voltage of 10 kV, 12 kV, and 14 kV without seeding (a) and with seeding(b).

The particles used as seeding are charged by collisions with charged particles in the plasma. This type of behaviour is typical for plasma spray, where specific particles are introduced in a plasma and charged to be deposited on a surface.[143] Previous works have considered the density of seeding particles in a similar seeded jet (air only - no plasma) and determined that there is an approximate density of ~1.6×10^{11} particles.m^{-3} using a Mie-scattering approach.[144] Notably, this is approximately six orders of magnitude below the

anticipated electron density of the plasma. Also, the seeding particles being small (1-2 μm) limit their influence.[145] Hence, the seeding particles used in this study are assumed to have little influence on the key characteristics of the discharge.[143]

The practical consideration for the capture of high-quality PIV data requires several steps. First, the centre of the plasma jet and the jet flow should be at the intersection of the laser sheet and the camera field of view. This step is of paramount importance, and a misplacement would imply the laser sheet deviation from the centre of the jet, thus missing the core of the jet. The second step is focusing the laser and the camera on the position of the targeted flow; following this step, a calibration image can be recorded and used for processing purposes. When the system is fully aligned and spatially calibrated, a sequence of approximately 50 frames of data is captured and processed to ensure the system is operating as expected. This is done before embarking on a long experimental data collection campaign.

To obtain velocity vectors from the jet flow recorded images, a cross-correlation procedure is implemented within the PIV software and described in Figure 20. The processing can be used to obtain information on the displacement of the detected particles. In the typical case of an interrogation area size of 32 x 32, a 6 - 8 px displacement is considered suitable for accuracy[7]. If the displacement does not fit the criteria, a change of the time delay between laser pulses (Δt) allows for adjustments to be made. In this study, the interest lies in the time-averaged velocity fields; thus, the frequency was lowered to 200 Hz, and the number of images per set of experiments was between 400 - 500 images (e.g., 800 – 1000 frames). The maximum number of images is limited by the camera memory, as each frame is approximately 8 mb in size, and the space available on the computer hard disk given thousands of images are created in each experimental run. As an example, the data displayed in Chapter 4 was obtained from

60 000 recorded images. Increasing the duration of the experiment and thus the number of recorded frames decreases the uncertainty.

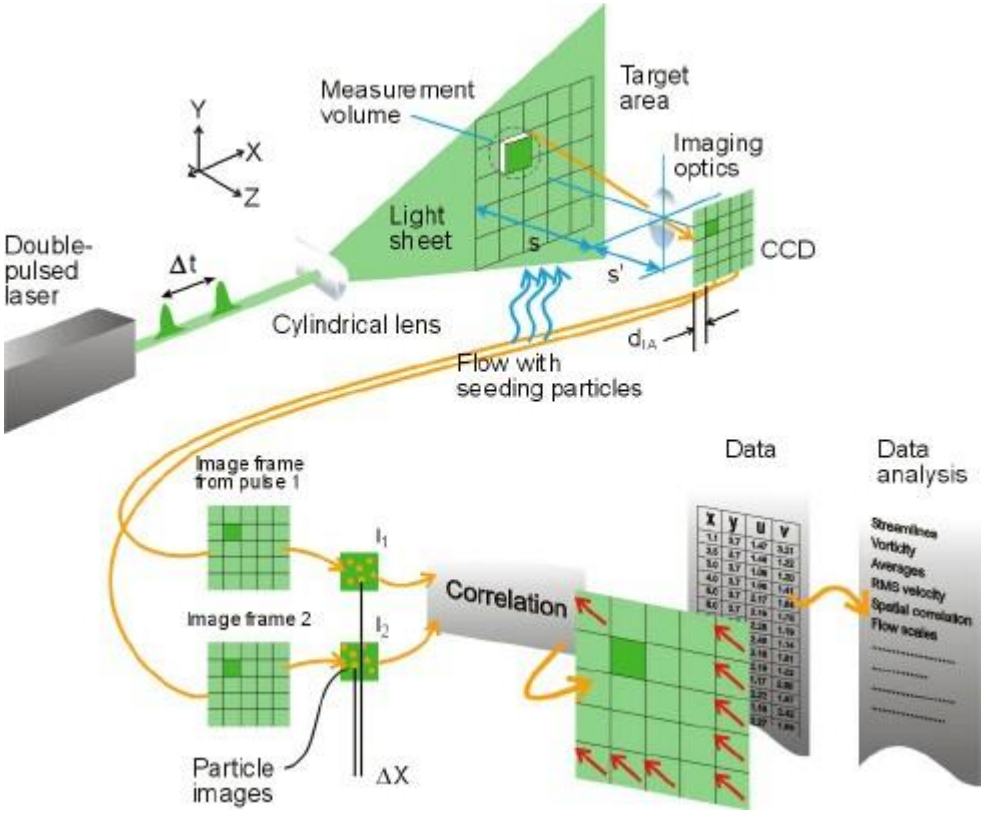

Figure 20: Particle Image Velocimetry principle schematic.[146]

After capturing all the frames, careful processing of the data was required to extract the velocity parameters. Using the TSI software, the processing steps are split into three distinct categories: pre-processing, processing, and post-processing. Pre-processing corresponds to the manipulation of the recorded raw frames by the addition/subtraction of filters. Subtraction of a calibration image or a minimum intensity can improve the ability to detect particles significantly. In the processing phase, a grid is generated to identify areas of interrogation in the images. The implementation of a grid over each frame is shown in Figure 20; the cross-correlation method consists of identifying a similar signal from an interrogation area from two successive frames (A and B) captured with a chosen delay Δt. A high flow velocity induces a high displacement, forcing a larger grid size, which generates more uncertainties as more

groups of particles would be present in each grid square. On the contrary, insufficient displacement would not be detected, which would increase measurement uncertainties.

After the processing of each pair of frames, a vector map is generated, the number of vector fields obtained is equal to half of the frames captured, highlighting the importance of capturing a high number of frames. Within the TSI software, three types of vectors are created following the processing stage; these represent an excellent match, a poor match, or an artificially generated vector; they are distinguished by a colour scheme, respectively; green, red, and yellow. The presence of bad vectors is considered a major problem, and, typically, vector maps with >5% bad vectors were rejected. The streamwise and radial velocity components with their spatial position in each image pair could be extracted from the vector maps. To obtain the final time-averaged velocity profile, all the vector maps from a single experimental run were averaged, generating an ensemble-average velocity map.

3.5 Rayleigh scattering

Another technique used in this study to understand the fluid dynamics and particularly the mixing of helium and air downstream of the jet capillary was the Rayleigh scattering technique. The Rayleigh scattering is the scattering of light by particles that are very small in relation to the wavelength of the emitted light. The Rayleigh scattering experiment consists of observing the elastic scattering of electromagnetic radiation by particles size up to a tenth of the wavelength (λ) of the electromagnetic radiation.[147–151] The particle polarises under the influence of an electric field, inducing a dipole moment that oscillates, generating radiations in all directions.[152]

In the case of a helium plasma jet impinging into quiescent ambient air, the helium molecules scatter significantly less light than air. As an example, the scattering cross-section at a wavelength of 532 nm is 4.45×10^{-31}m^2 for argon,[153] and 5.16×10^{-31} m^2 for air.[154] In comparison, the square of the optical polarizability ratio of helium and argon is $\left({}^{\alpha_{He}}/_{\alpha_{Ar}}\right)^2 = 1.56 \times 10^{-2}$ showing helium barely scatters light.[155,156] In fact, in a mixture of air and helium, the scattering light emitted by helium is close to negligible compared to the total intensity.[157] Therefore, it can be assumed that since the only scattered light comes from the air, this optical technique can provide quantitative data on the mixing of the helium jet into the ambient air. Observations of the influence that the plasma discharge has on the mixing of the helium and air entrainment would complement the PIV and LIF measurements. Linking the fluctuations and production of turbulence to the entrainment of air and mixing of the neutral gas flow with ambient air.

In the most common case, isotropic polarisation, where the diameter of the particle $d_p \ll \lambda$, and a point at a distance $z \gg \lambda$, the intensity of the scattered light is given by:

$$I_{Sc} = I_0 \frac{8\pi^4 \alpha^2}{\lambda^4 z^2} (1 + \cos^2 \xi) \qquad (3.23)$$

Where I_0 is the intensity of the incident wave and ξ is the scattering angle, and α is the polarizability. The dependence of the intensity with the wavelength is $\frac{1}{\lambda^4}$, showing the importance of having $d \ll \lambda$ to avoid perturbations.

The configuration of the Rayleigh scattering setup is shown in Figure 21. A Nd:YAG pulsed laser (Nano S 130-10 Litron Lasers) was employed with a frequency of 1 kHz, a pulse energy of 220 mJ, a pulse duration of 4 ns, and at a wavelength of 532 nm. The round collimated laser followed a beam expander to become expanded vertically, a laser dump is situated at the

end of the optical path. The area of interest was situated at the intersection of the APPJ and the laser sheet. The signal was captured with an intensified charge-coupled device (iCCD) Andor iStar iCCD DH734-18U-03 connected to the Andor Solis software. The background A viewing dump was situated on the opposite side of the camera to avoid perturbations. The background and the signal were captured as an accumulation of 25 images at a frequency of 840 Hz. For each image recorded, the iCCD camera was configured to accumulatively capture 500 laser pulses, using an optical gate width equal to 10 ns for each exposure of 1 s.

To generate a laser 'sheet,' a plano-concave cylindrical lens (dimensions 10x12 mm^2, a focal length of -9.7mm) transforms the beam from a collimated beam to an expanding one along the z-axis. A second lens, a plano-convex cylindrical (dimensions 30x32 mm^2, a focal length of 70 mm), collimates the beam into a rectangular shape. The original beam is spherical with a diameter of 3 mm; the optical path transformed it into a 3 mm x 20 mm rectangular beam. Finally, a plano-convex spherical lens (diameter of 50.8mm, focal length of 100 mm) sends the beam into the laser dump. The position of each lens is crucial for the correct collimation of the beam. The iCCD camera is situated at a 90-degree angle and focused on the intersection of the laser and the jet. Precautions were taken to avoid the perturbations of unwanted reflections of the laser, which consist of covering the different sections on the optical path.

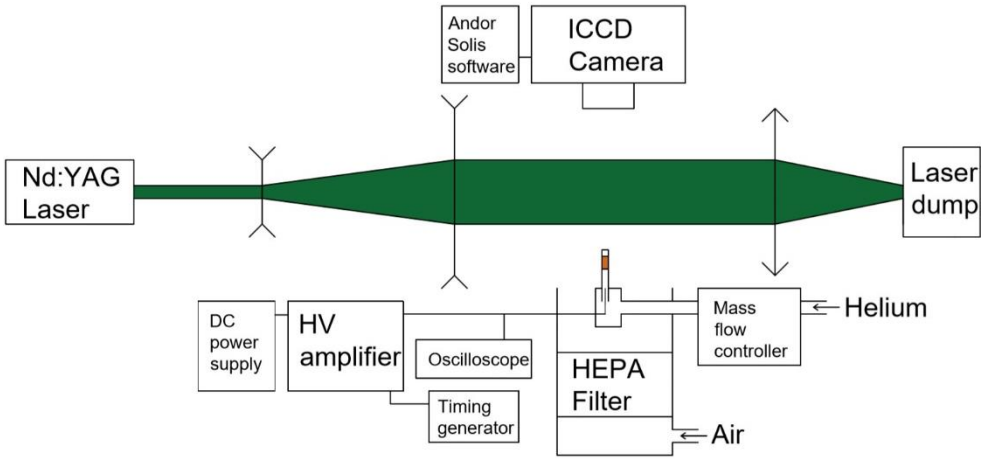

Figure 21: Rayleigh scattering configuration setup.

The challenge of light scattering from dust in the environment is highlighted in Figure 22. The reflections from dust, observed as bright dots on the image of Figure 22(a), are of high intensity and can damage the ICCD camera. To solve this problem, a weak flow of compressed air was emitted upward through a high-efficiency particulate air (HEPA) filter situated under the jet, as shown in Figure 23. The injected airflow was deemed too weak to perturb the jet. This modification of the setup enables the Rayleigh scattering data to be acquired without risk to the camera. Figure 22(b) shows the scattering data with HEPA filtered air in the measurement region.

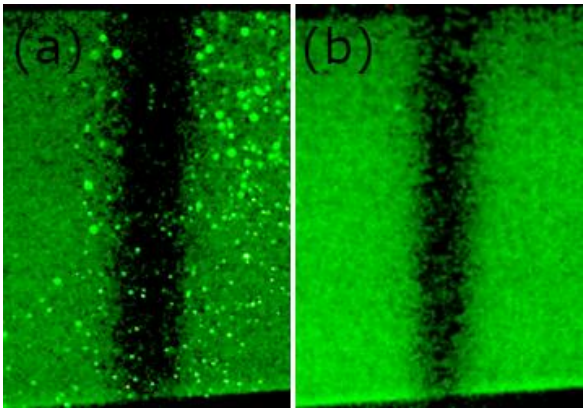

Figure 22: Rayleigh scattering of a helium jet with dust particles (a) and airflow (b).

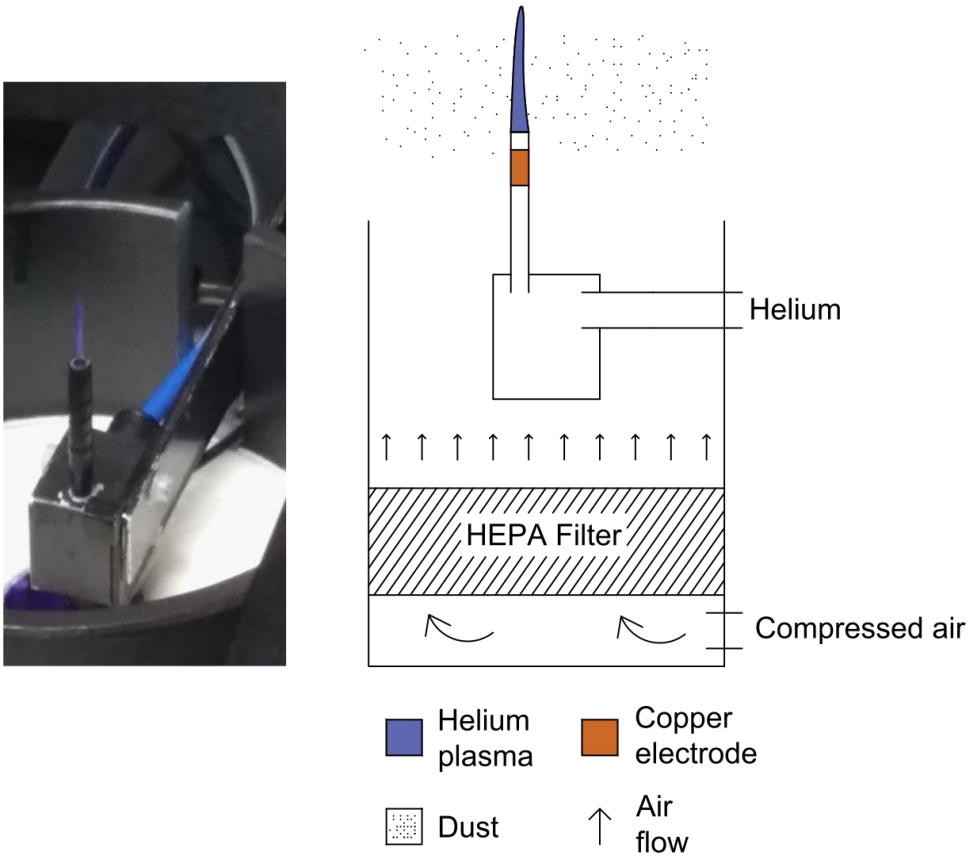

Figure 23: Picture of the APPJ configuration for Rayleigh scattering measurements (left) and diagram of the method to avoid dust in the area of interest (right).

The ICCD camera captured an accumulation of images corresponding to an intensity value for each pixel per image. A typical set of raw data and a schematic depiction of the helium and air scattering cross-section are shown in Figure 24. The scattering of ambient air can easily be distinguished from the non-scattering of helium in the jet.

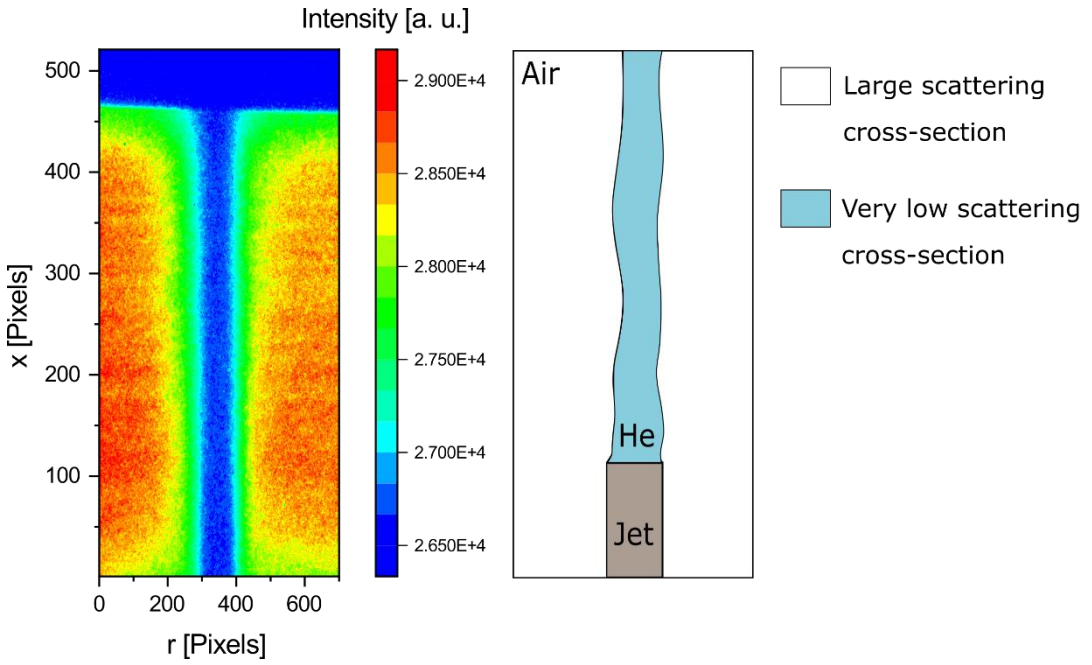

Figure 24: Rayleigh scattering measurements of ambient air (left)and schematic of the scattering cross-section regions in the APPJ (right).

The scattering intensity in a region away from the jet was chosen to represent 100% air to obtain a quantitative value for the admixture of air in the helium flow. The scattering intensity in a point close to the jet orifice in a pure helium flow was chosen as being representative of a 0% air condition. In contrast, it is not entirely correct, as the helium flow is never entirely free of trace air components, it was deemed that reflected light from the environment would be by far the greatest source of light in this region, thus providing a reliable 0% air case. The relative scattered intensity from the pure air region to the pure helium region provided an estimation of the mixing of ambient air into the helium jet flow.

3.6 Laser-induced fluorescence

Laser-induced fluorescence (LIF) is a time- and space-resolved spectroscopic method for species-specific gas phase analysis. It is a combination of absorption and emission spectroscopy where a ground state atom or molecule is excited to a higher energy level by

absorbing laser light. Subsequently, the excited chemical species spontaneously emit photons on its transition back from an excited state to a lower energy state. When an excited atom or molecule relaxes from a higher energy level to a lower one, it emits light that can be captured. The wavelength of this emitted light is specific to the excited chemical species structure.

The LIF measurement system used in the investigation is shown in Figure 25. The system was used to measure OH radical density and obtain an indication of air entrainment within the plasma plume by measuring the radiative decay time of the laser-excited OH(A) state. The system comprises a tunable dye laser (Sirah Cobra Stretch with second harmonic generation unit) pumped by a 6 ns pulsed Nd:YAG laser with a wavelength of 532 nm, pulse energy of 120 mJ, and a repetition rate of 10 Hz. Some LIF excitation schemes have been proposed for the measurement of OH radicals in atmospheric pressure plasmas.[137,158,159]

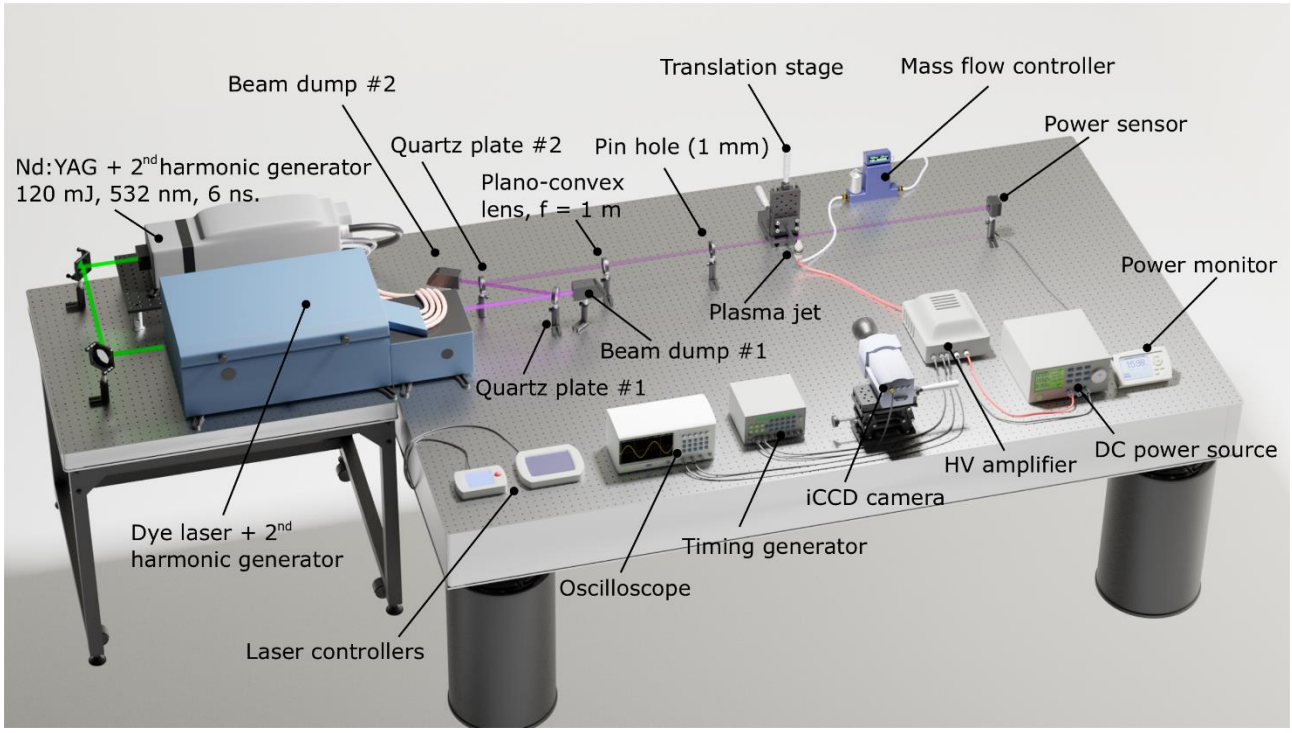

Figure 25: Diagram showing the layout of the Laser-Induced Fluorescence experiment.

In this work, the dye laser was tuned to generate an output at a wavelength 282.58 nm to excite the $P_1(2)$ transition from the $f_1(2)$ rotational level of OH X($v'' = 0$) to the $F_1(1)$

rotational level of OH A(v' = 1). Figure 26 shows the LIF intensity measured against the wavelength. A previous study has used a similar excitation scheme due to the $P_1(2)$ transition being spectrally separated from adjacent lines and the $f_1(2)$ level having the largest relative population in the temperature range under investigation.[160]

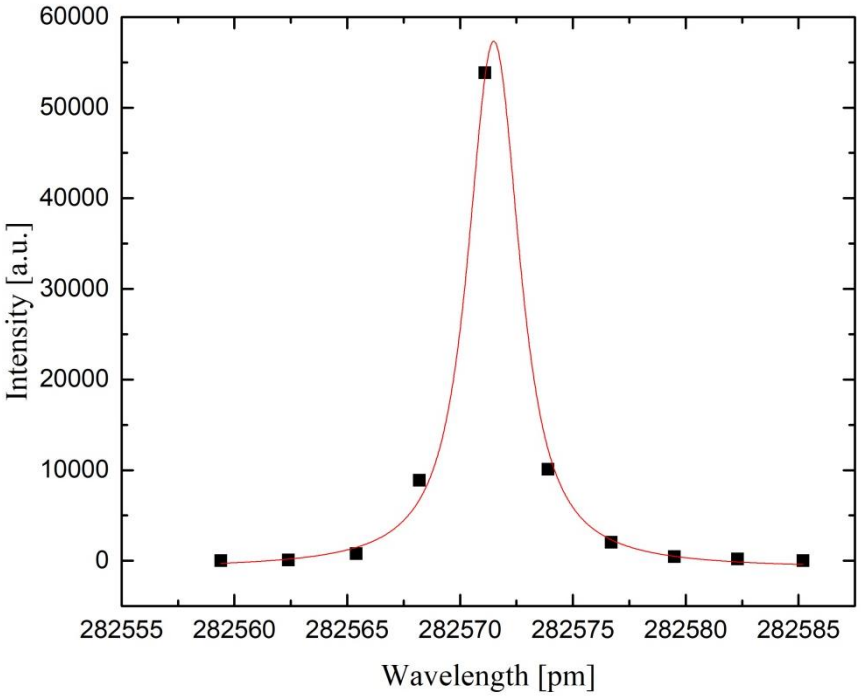

Figure 26: LIF intensity of the $P_1(2)$ transition of OH against wavelength at a laser energy per pulse of 10 µJ with a Voigt fit.

The 282.58 nm beam emitted from the dye laser was measured to have pulse energy above 17 mJ, a value several orders of magnitude above the linear range. LIF measurements are typically made (1 – 10 µJ).[161] Operation beyond the linear region greatly complicates the interpretation of the results, as the ground state rotational level is significantly depleted by light absorption and partially refilled by fast rotational redistribution. This alters the LIF outcome dependent on the unknown gas composition and temperature. An optical arrangement similar to that employed by Ries et al. was adopted to attenuate the laser energy to a suitable range.[162] Two quartz plates were angled to split the beam with a small fraction being reflected towards

the plasma jet and the majority of the beam passing through to beam dumps mounted behind each plate. Following attenuation, the beam was directed through an uncoated quartz plano-convex lens with a focal length of 1 m, and a pinhole of 1 mm was positioned to act as a spatial filter, further attenuating the beam. The maximum laser pulse energy was found to be approximately 15 µJ; small changes to the Q-switch delay of the pump laser were subsequently used to vary the pulse energy between 1 and 15 µJ. Laser power was measured using a Thorlabs PM100D optical power and energy meter equipped with a thermal volume absorber power sensor.

An Andor iStar740 iCCD camera was fitted with a Jenoptik UV 105 mm f/4.5 imaging lens to capture the fluorescence of excited OH molecules. The camera arrangement was positioned to face the plasma jet perpendicular to the laser beam. For each image recorded, the iCCD camera was configured to accumulatively capture 500 laser pulses, using an optical gate width equal to 8 ns for each exposure. Following the approach of Verreycken et al.,[160] no bandpass filter was used during LIF measurements to avoid the need for additional corrections in the calibration procedure. A consequence of this approach is the potential for the interference of the fluorescent signal from other emissions within the plasma and the Rayleigh scattering signal. Background subtraction of the emission captured with the plasma energized and laser de-tuned was used to correct light emitted by the plasma and any scattered light. To ensure the measurements were conducted within the linear LIF region, the measured LIF intensity was plotted against laser energy, and a linear fit was applied shown in Figure 27. It was determined that the linear range was between 1 µJ to 10 µJ, a value in close agreement with several past LIF investigations.[160,162]

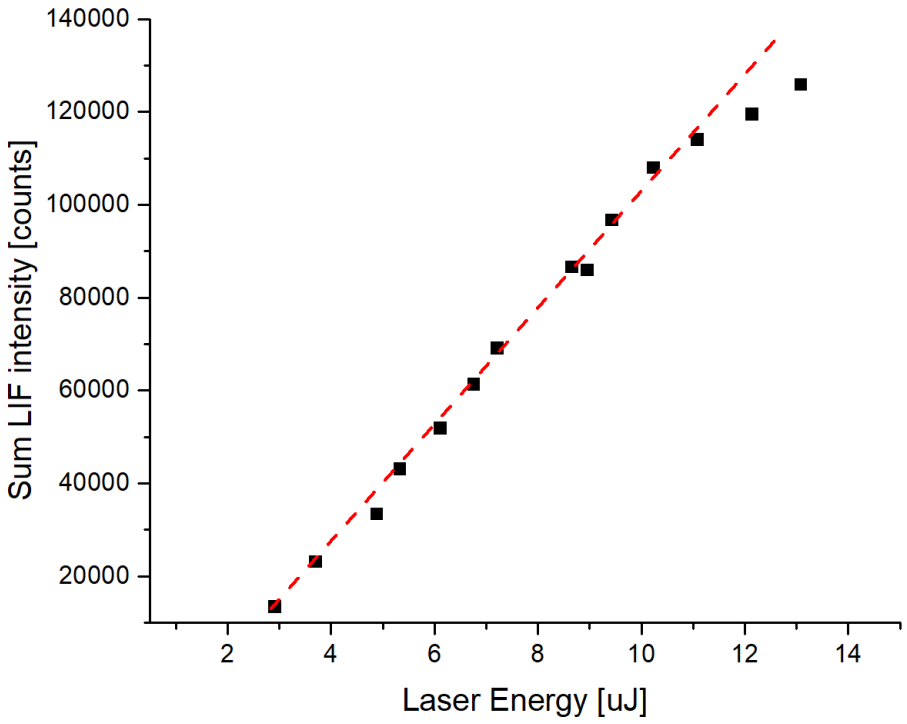

Figure 27: LIF saturation curve. Sum of LIF intensity against the laser energy [µJ] measured with a linear fit.

The discharge is not synchronized with the laser; consequently, all values are therefore time averages with respect to the discharge. For LIF measurements, the actual density of OH will fluctuate with the applied voltage, reaching a maximum as the ionisation front passes the observation point and falling to a minimum at the instant before the emergence of the next ionisation front. However, the lifetime of OH in helium is relatively long, with the works of Ries *et al.* indicating that the half-life of ground-state OH in a similar helium jet is almost 300 µs.[162] As the excitation frequency is 20 kHz, two discharge events per 50 µs period can be expected. It may be concluded that the time-variation in OH density is minimal over this period, and synchronization to the laser pulse is not necessary.

Absolute calibration of the LIF signal to determine the density of ground-state OH can be achieved via several methods, including UV absorption, chemical modelling, and Rayleigh scattering.[160,163] In this investigation, the Rayleigh scattering approach was adopted due to its

high degree of accuracy, and a similar methodology to that described by Verreycken et al. was adopted.[160] Calibration by Rayleigh scattering requires detailed knowledge of the rotational and vibrational energy transfer rates, which vary significantly depending on the nature of the quenchers present; thus, an accurate appreciation of the gas composition is essential. Careful consideration must be applied in the case of a plasma jet as the gas composition varies as a function of distance from the jet orifice. Also crucial for the determination of absolute OH density is the decay time of the laser-excited fluorescent state. This was measured at each spatial position by applying a time delay to the iCCD camera from 6 ns (i.e., immediately after the laser pulse) up to 2000 ns; the fluorescent intensity from 500 laser shots was at each time point accumulated to form a single image. From each image, the sum of LIF intensity in a 0.36 mm^2 interrogation area on the jet centreline was determined and plotted as a function of delay time; an exponential fit was applied to determine the decay rate at each spatial position.

In addition to the gas composition, the gas temperature can also affect the interpretation of the LIF data. An Omega FOB100 fibre-optic thermometer was used to investigate the influence of plasma generation on the gas temperature. The dielectric temperature probe was positioned in the plasma plume at various points downstream of the jet orifice, and the temperature was recorded. The temperature was found to vary little with spatial position, with a maximum of 10 K above ambient located close to the capillary orifice; such observations are in line with previous studies.[35]

The calibration process closely followed that reported previously by Verreycken et al.[160] The jet capillary was supplied with Nitrogen gas at a flow rate of 2 SLM to obtain Rayleigh scattering data for calibration. Although it was not strictly necessary, the nitrogen flow helped to ensure dust from the ambient environment did not enter the measurement region of interest. The laser power varied from 2 to 15 µJ in a 1 µJ increment. The sum of the Rayleigh

scattered signal intensity in a rectangular region of interest measuring 0.36 x 0.36 mm was calculated. The measured Rayleigh scattered signal, S_{Ray} (#counts), can be written as:

$$S_{Ray} = \eta N_n \frac{\partial^{\beta=0}\sigma_0}{\partial\Omega} V_{Ray} I_L t_L \tag{3.2}$$

Where η is the calibration constant (#counts sr J^{-1}), N_n is the density of scattering particles (m^{-3}), $\partial^{\beta=0}\sigma_0/\partial\Omega$ is the differential cross-section for Rayleigh scattering ($m^2\,sr^{-1}$), V_{Ray} is the volume from which Rayleigh scattering is collected (m^3), I_L is the laser irradiance ($W\,m^{-2}$), and t_L is the temporal length of the laser pulse (s), which was measured by replacing the power meter shown in Figure 25 with a fast photodetector. After taking into account, the non-uniformity of the laser energy density, Equation (3.2) becomes:

$$S_{Ray} = \eta N_n \frac{\partial^{\beta=0}\sigma_0}{\partial\Omega} E_L \Delta x \tag{3.3}$$

Where E_L is the laser energy (J), and Δx is the length of the detection volume (m). Following this, the calibration constant η was obtained from the slope α, of the measured Rayleigh intensity as a function of laser energy multiplied by pressure:

$$\eta = \alpha k_B T \frac{\partial^{\beta=0}\sigma_0}{\partial\Omega} \Delta x \tag{3.4}$$

Where k_B is the Boltzmann constant, and T is the temperature (K). Using the calibration factor, the intensity of the laser-induced fluorescence S_{LIF} can be expressed as:

$$S_{LIF} = \frac{1}{4\pi} \int \eta E n_{exc}(x, y, z, t) A \, dxdydzdt \tag{3.5}$$

Where E is the energy gap according to the chosen transition, A is the Einstein emission coefficient (s^{-1}), and $n_{exc}\,(x, y, z, t)$ is the density of OH in the excited state.

The overlap integral g_{int} (1/m^{-1}) represents the overlap between the spectral profile of the absorption transition Y_A (1/m^{-1}) and the spectral profile of the laser L_L (1/m^{-1}), using the frequency $\nu = 1/\lambda$, and both functions are normalised to unity.[160]

$$g_{int} = \int_{-\infty}^{+\infty} Y_A(\nu) L_L(\nu) d\nu \tag{3.6}$$

Finally, Table 4 shows the relevant experimental parameters used in the LIF measurements.

Table 4: Experimental parameters used in LIF measurements and absolute density calibration

Parameter	**Description**	**Value**
λ_L	Laser wavelength	282.58 [nm]
$\Delta\lambda_L$	Linewidth of the laser	0.95 [pm]
g_{int}	Overlap integral	0.017 [1/m^{-1}]
A_L	Area of the laser beam	0.0746 [mm^2]
E_L	Laser energy per pulse	10 [μJ]
τ_L	Temporal FWHM of the laser pulse	6 [ns]
Δx_v	Length of the detection volume	0.359 [mm]
Δy_v	Width of the detection volume	0.359 [mm]
Δs	The spatial FWHM of the laser beam at the observation point	0.1795 [mm]

To characterise the presence of OH in the APPJ, the measurements were done streamwise and radial for two applied voltages 10 and 14 kV. Two travel translation stages with an end-mounted micrometer were used to control the displacement of the APPJ with

respect to the laser beam, measurements were done with 0.5 mm step radially and 1 mm step streamwise. This involved a high number of measurements with repeats providing an accurate depiction of the spatial presence of OH in relation to the APPJ expanding in ambient air. The background image was captured with the helium jet without the plasma discharge, verifying the absence of fluorescence signal without the plasma discharge.

The iCCD camera captured 25 images composed of 500 accumulated acquisitions. The intensity of the fluorescence signal was estimated from the total count number of a selected area; this area called an interrogation area, had a size of 0.36 mm^2. The intensity is then plotted against the time after excitation revealing the fluorescence intensity decay pattern.

The decay time is calculated from the decrease of intensity over time after the laser excitation. The signal is captured at multiple time intervals to provide an accurate depiction of its decreasing trend. Figure 28 shows the decreasing signal in intensity for several delay times.

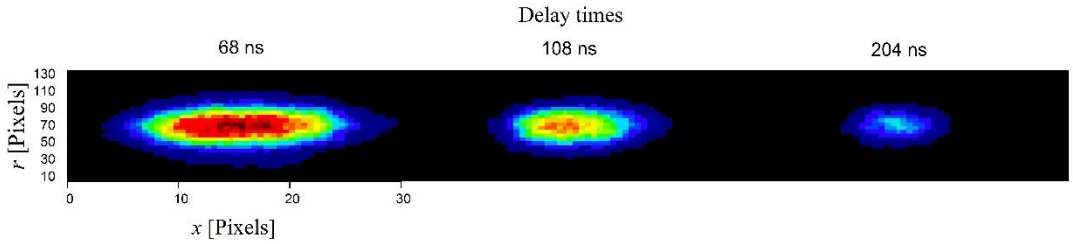

Figure 28: LIF relative intensity measurements of OH fluorescence in an APPJ for several delay times after excitation.

Plotting of the normalised LIF intensity against the delay time is shown in Figure 29. The addition of an exponential decay fit allows for the estimation of the laser-induced fluorescent signal decay rate. This parameter is crucial to quantify the ground state density and estimate the progression of air entrainment in the jet.

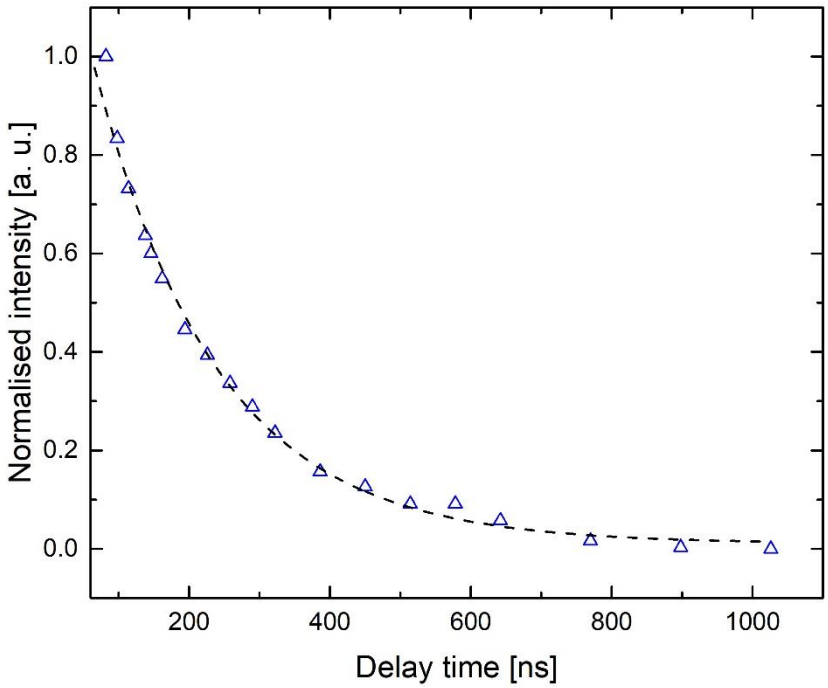

Figure 29: Normalised LIF intensity against the delay time, with an exponential decay fit.

Chapter 4 Quantitative assessment of the fluid dynamics at play in an atmospheric pressure plasma jet

Some of the results in this chapter were presented in a Conference poster in the European Physical Society conference on plasma physics, 2018; Y. Morabit, R. D. Whalley, E. Robert, M. I. Hasan & J. L. Walsh. **'Quantitative insights into the fluid interactions downstream of an atmospheric pressure dielectric barrier plasma jet'**

4.1 Introduction

The study of turbulence is one of the most intriguing subjects of our time. It comes down to the applied forces on a gas, moving in a 'chaotic' way, creating eddies, and being overall challenging to predict. Subsequently, many studies have considered the impact of forced driving on flow gas jets due to their wide number of practical applications in areas such as combustion. However, the use of plasma as a means to perturb a jet flow field has only recently been considered. In the case of an APPJ, with a laminar flow (Re < 2300) the origin of the plasma-induced transition-to-turbulence remain unknown. The plasma-induced velocity increase by no more than 10% of the maximum velocity U_m, this velocity increase is not high enough to provoke a transition by itself.[103] The shear layers of the jet are very vulnerable to small perturbations, which can propagate and amplify in the jet.[103,140] The observation of the velocity flow field of the plasma jet provides further insight into the presence of perturbations, velocity fluctuations, and the onset of turbulence.

One of the key elements influencing the intensity of the plasma discharge is the applied voltage. Several studies showed that increasing the applied voltage lead to a reduced laminar

region length, and earlier onset of turbulence.[2,27,103] The consequences of the applied voltage on the plasma-induced velocity increase of the gas flow and the generation of disturbances in the shear layer of the jet are raised questions. Moreover, the stability of the laminar region under the plasma-induced disturbances is not clear. Another important element is the injected gas flowrate, affecting the Reynolds number and distinguishing plasma- and flowrate-induced behaviours.

This chapter explores the impact of the applied voltage and flow rate of an APPJ on the visible plasma plume, the flow field of the expanding jet in ambient air. Measurements of the velocity flow field were performed using PIV. Estimations of transition-to-turbulence point and turbulence fluctuations providing insight into the instabilities in the plasma jet.

The figures presented in this chapter are part of a much larger set of data; the entirety of the data is presented in Appendix A not to encumber the analysis and the discussion.

4.2 Experimental methodology

The plasma jet used in this study was described in section Chapter 3 , the metallic strip electrode was ***grounded***. The applied voltages examined in this study were sine waves 10, 12, and 14 kV_{pk-pk}, with a frequency of 20 kHz. Helium gas with a purity of 99.999% flowed through the capillary at a range of 2.5 – 3.7 SLM, giving a maximum exit velocity, U_m, between 11.7 – 17.4 m s^{-1}.

PIV measurements were undertaken using the experimental setup and method described in section 3.4 . The operating frequency was 200 Hz, the time delay between consecutive laser pulses (Δt) was set between 8 and 16 μs, a value chosen to capture the movement of oil droplets over a grid with spatial dimensions of 24x32 μm^2 with a 50% overlap between adjacent

interrogations windows. Each dataset comprised of 1000 frames that were used to make 500 individual velocity vector maps; in the case of time-averaged measurements, all 500 vector maps were averaged and presented as a single figure.

The Schlieren photography experimental setup and method were described in section 3.3 .

4.3 Preliminary qualitative observation of the plasma jet

To confirm the behaviour of the plasma jet matches those reported in the recent literature, qualitative observation of the flow and the influence of the plasma discharge was obtained. The primary focus of these efforts was on observing the reduction of the laminar length provoked by the plasma discharge in the helium jet. To achieve this in a practical way, the choice was the use of Schlieren photography. In addition, the observation of the plasma plume length using standard photography was performed. This section focuses on the qualitative insight, and provide a comparison point for the PIV results shown in the next section.

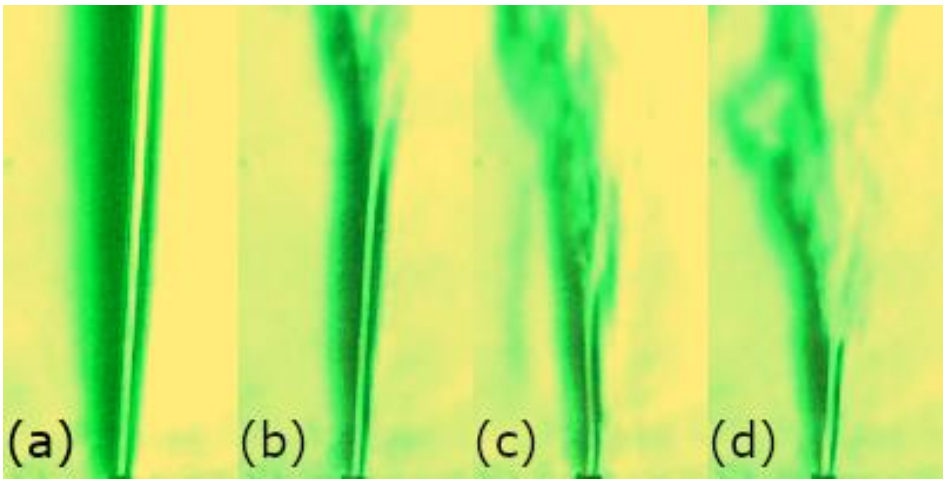

Figure 30: Schlieren Photography of an APPJ expanding in ambient air with an input helium flow rate of 2.5 SLM, (a) no plasma, with an applied voltage of (b) 10 kV, (c) 12 kV, and (d) 14 kV.

The Schlieren visualisation observation is shown in Figure 30, where the APPJ is expanding in ambient air, with an input flow rate of helium at 2.5 SLM, with (a) no plasma, and with an applied voltage of (b) 10 kV, (c) 12 kV and (d) 14 kV. The effect of the applied voltage on the flowing helium noticeably shortens the laminar region and has been previously reported.[27] The reduction of the laminar length is considerable for the highest applied voltage of 14 kV, as the length of the laminar region is reduced to 7.5 mm. For comparison, the length of the laminar region is 17.5 mm and 10 mm respectively for 10 kV and 12 kV cases. Whereas the case without plasma is laminar over the entire field of view, which extends beyond 60 mm. These particular voltage conditions were selected as they showed significant variations in flow behaviour while remaining within the field of view of the PIVs high-speed camera.

In order to complement the qualitative observations with Schlieren Photography, pictures of the plasma plume under the same generation conditions were taken. The pictures of the visible plasma plume propagating into the ambient air for a range of flow rates 1-8 SLM and applied voltages of 10 kV, 12 kV, and 14 kV are shown respectively in Figure 31-33-. The trend of the plasma plume length against the flow rate is similar for all applied voltages; the

plume increases in length with the increasing flow rate, although for 12 and 14 kV the plasma plume length decreases and shows signs of an unstable and turbulent plume-end. These observations are coherent with previous results.[3] In the 10 kV case, the plasma plumes are well defined and have a sharp end; this reveals an expected laminar behaviour of the flow around the plasma plume.[2] At 12 kV input, the sharpness of the plume is altered at 8 SLM, whereas in the 14 kV case it starts at 3 SLM onward; this is an indicator of the presence of turbulence and reduction of the laminar length.

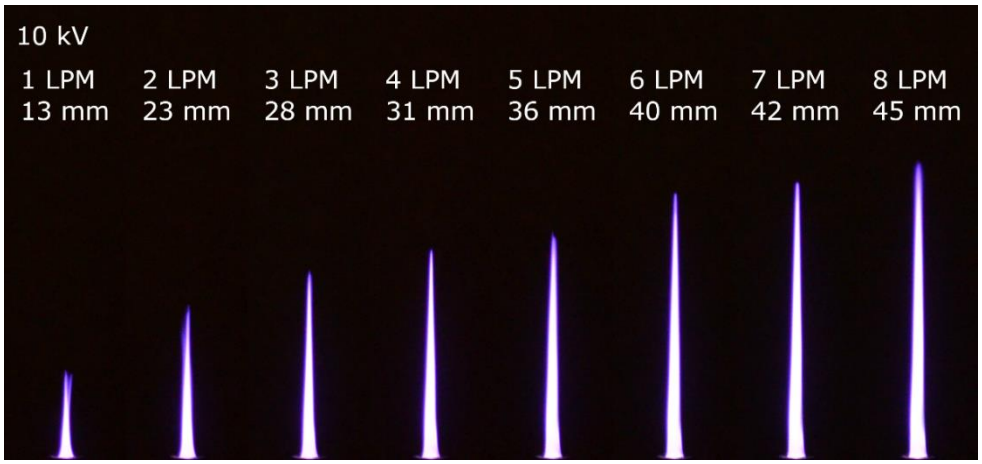

Figure 31: Photography of sine-driven APPJ plasma plume with an applied voltage of 10 kV.

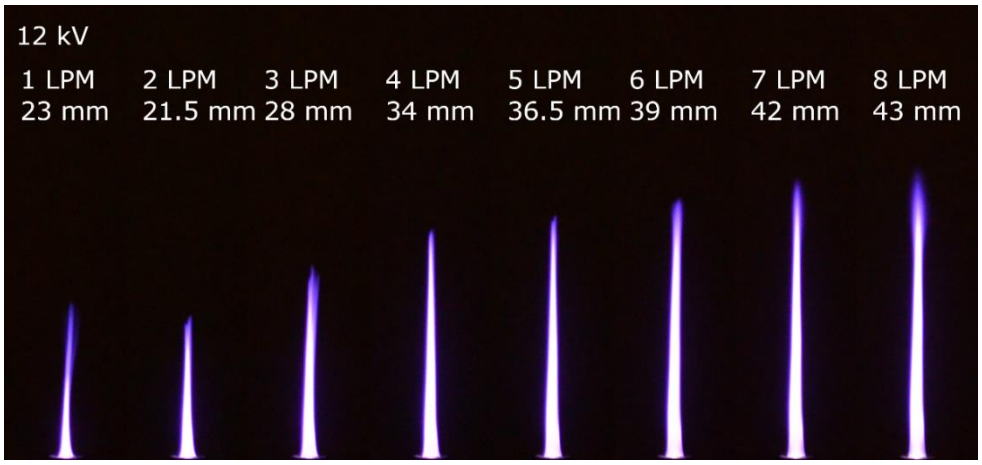

Figure 32: Photography of sine-driven APPJ plasma plume with an applied voltage of 12 kV.

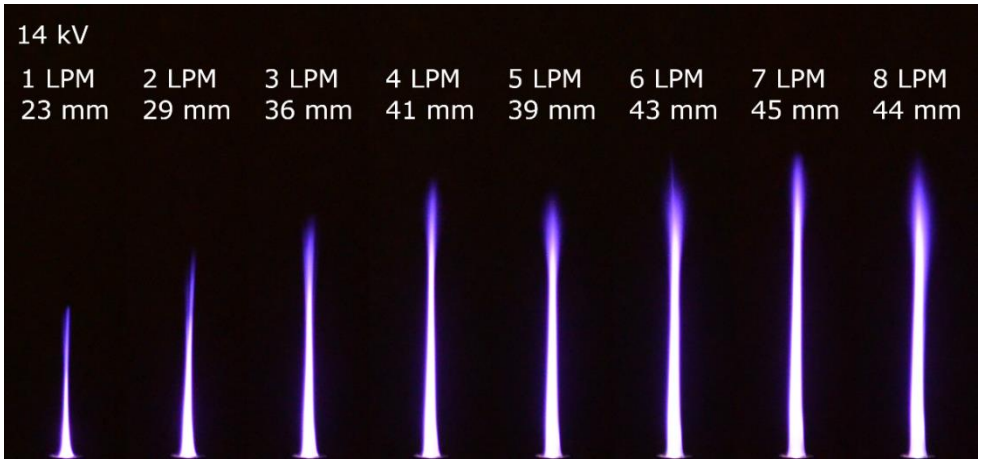

Figure 33: Photography of sine-driven APPJ plasma plume with an applied voltage of 14 kV.

4.4 Plasma-induced velocity increase

The plasma-induced velocity increase was mentioned as one of the factors at the source of the transition to turbulence if the APPJ expanding in ambient air. Although the velocity increase is unlikely to generate by itself a transition to turbulence in the case of a low Reynolds number jet, the velocity increase could be the source of perturbations in the jet. Figure 34 shows the measured velocity at the exit of the capillary with the PIV for several flow rates and applied voltages. An increase of 2 to 6 % is observed for the 10 kV case, a 3 to 7 % for the 12 kV case, and 5 to 9 % for the 14 kV case. The higher the applied voltage, the more important the plasma-induced velocity, however, an increase < 10 % of the initial velocity of the jet does not make the jet transition into a turbulent state.

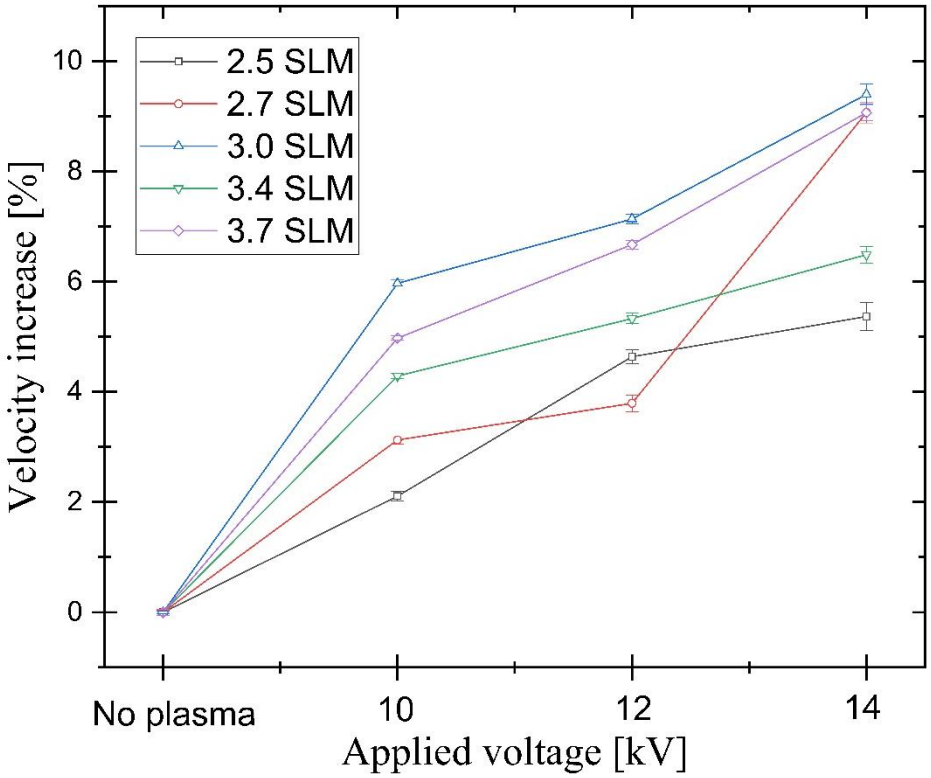

Figure 34: Plasma-induced velocity increase against the applied voltage of an APPJ.

4.5 Plasma jet velocity flow field

The velocity profile measurements taken with the PIV system followed the method described in section 3.4. Figure 35 shows the ensemble-averaged normalised velocity vector maps of the APPJ expanding in ambient air, for the cases with (a) no plasma and with an applied voltage of (b) 10 kV, (c) 12 kV, and (d) 14 kV. The measurements were done at a constant flow rate of 2.5 SLM (*Re* = 147.5) and are normalised by the diameter of the jet capillary (D = 3 mm), following the standard fluid dynamics approach of using non-dimensional units. Such low Reynolds (< 250) flows are known to be very susceptible to disturbances.[103] The flow is laminar in the case without plasma and travels across the field of view without the presence of obvious instabilities or significant velocity fluctuations. In the case (b), (c) and (d) where plasma is energised, the difference can be observed, with a clear reduction in the length of the laminar region as the applied voltage increases. This turbulent region can be identified by a

strong velocity gradient and an increase in the spread of the jet. As the voltage is increased a 'bending' of the flow is observed, in a coaxial jet, inevitable misalignments of the pin electrode in the capillary will result in a non-homogenous discharge and consequently a non-uniform distribution of force from the plasma acting on the flowing gas. The normalised velocity fields measurements with applied voltage of 10, 12 and 14 kV_{pk-pk} and flow rate of 2.5, 2.7, 3.0, 3.4 and 3.7 LPM are shown in Figure 36. The influence of the plasma discharge on the behaviour of the jet is similar to the one described in Figure 35 at each flow rate. However, the increase of the flow rate provoked a longer laminar region at fixed applied voltage. These results imply that the plasma-induced perturbations in the jet at a fixed applied voltage are similar and that their influence is dependent on the momentum of the fluid.

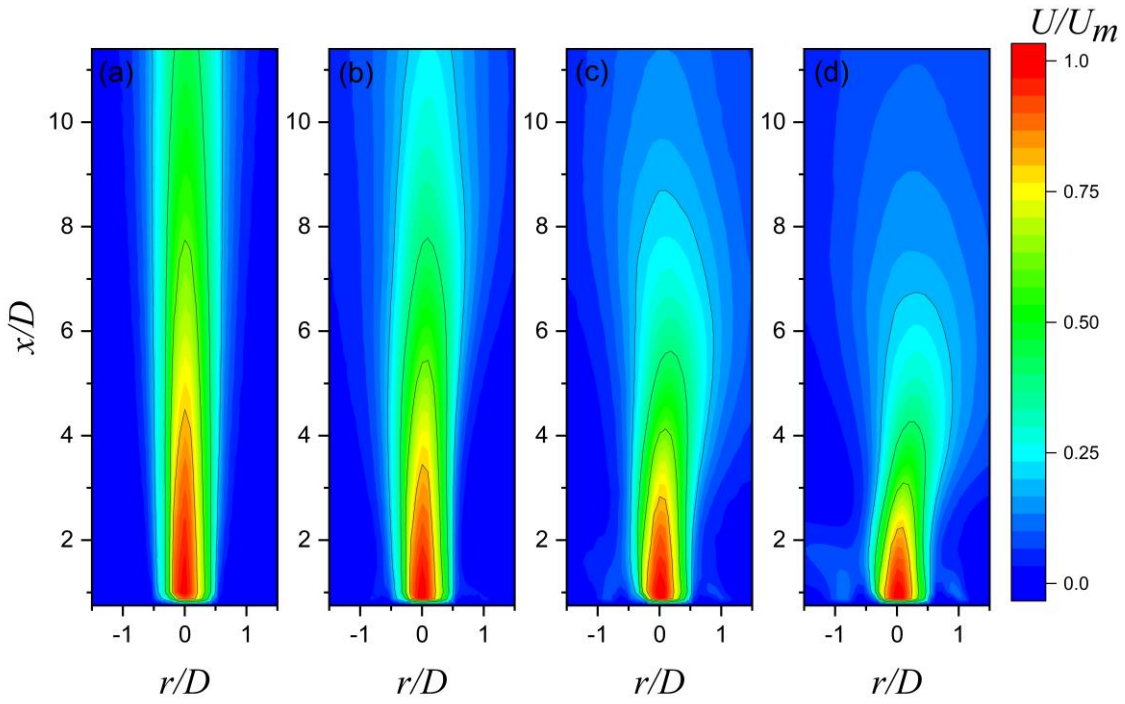

Figure 35: Ensemble-averaged normalised velocity contour for an APPJ (a) without plasma, with an applied voltage, (b) 10 kV, (c) 12 kV, and (d) 14 kV.

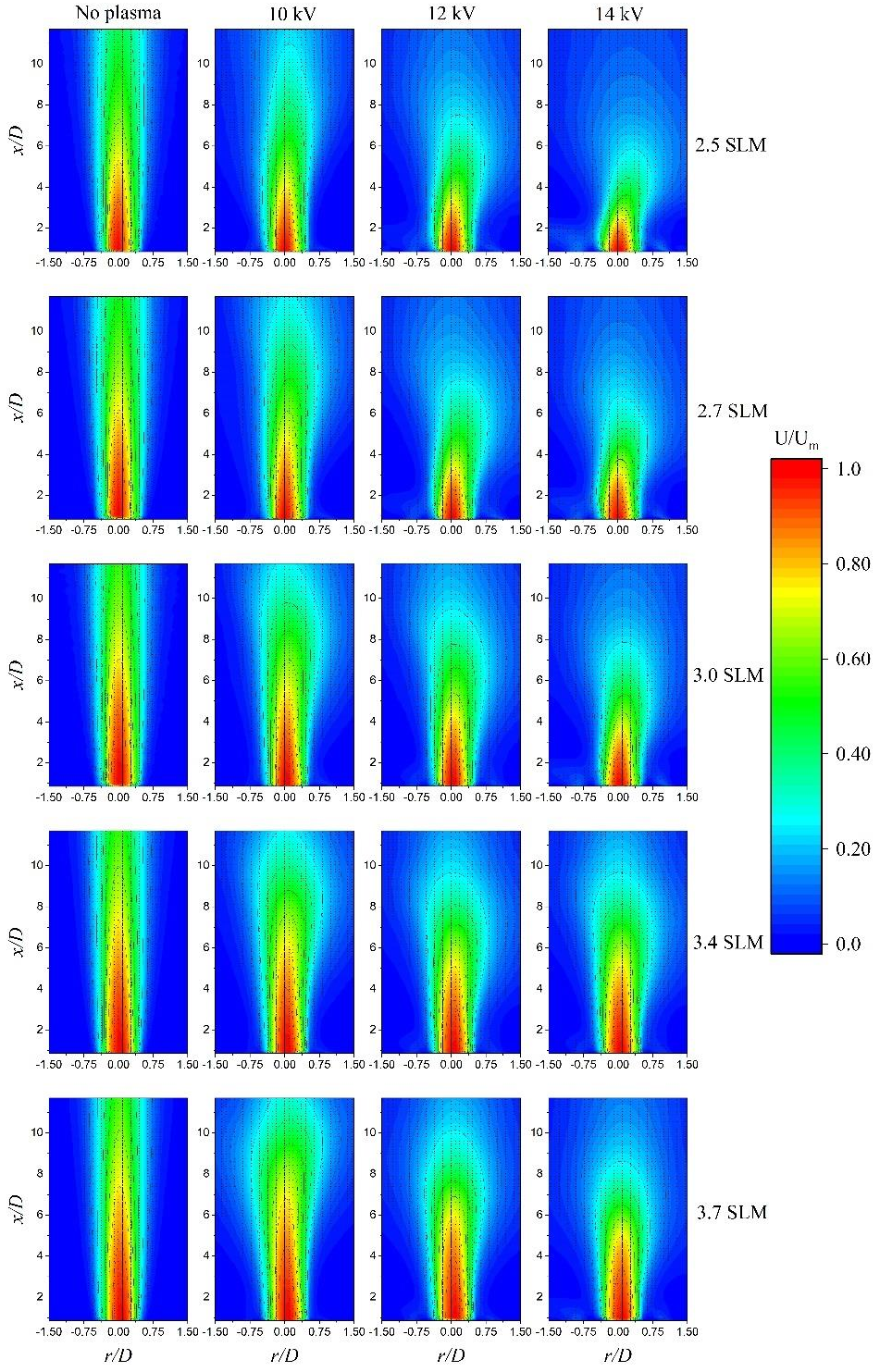

Figure 36: Ensemble-averaged normalised velocity contour for an APPJ without plasma (first column), with an input voltage of (second column) 10, (third column) 12 and (fourth column) 14 kV at a flow rate of (first line) 2.5, (second line) 2.7, (third line) 3.0, (fourth line) 3.4, and (fifth line) 3.7 SLM.

From the velocity contour, the centreline velocity values were extracted, Figure 37 shows the plot of the normalised streamwise centreline velocity U_m/U_c in the jet. The case without plasma serves as a point of comparison to characterise the influence of the plasma. It can be seen, that without plasma, the jet spreads out gradually and axisymmetrically, the mean velocity decreases linearly along the jet-axis following a normal jet development; thus, the jet is already in the transition phase. As a purely laminar flow would exhibit no obvious drop in velocity over the field of view considered here. The plasma cases have an early development similar to the case without plasma, then the plasma cases distinguish themselves with a drop in the centreline velocity before slowly stabilizing. The velocity decay is faster for higher applied voltages, suggesting the intensity of the turbulent behaviour is greater. To identify the transition-to-turbulence point, the moment the centreline velocity differs from the no plasma case and show a strong velocity gradient. The higher the voltage input, the sooner the transition to turbulence happens, and the steeper the gradient becomes in the turbulent region.

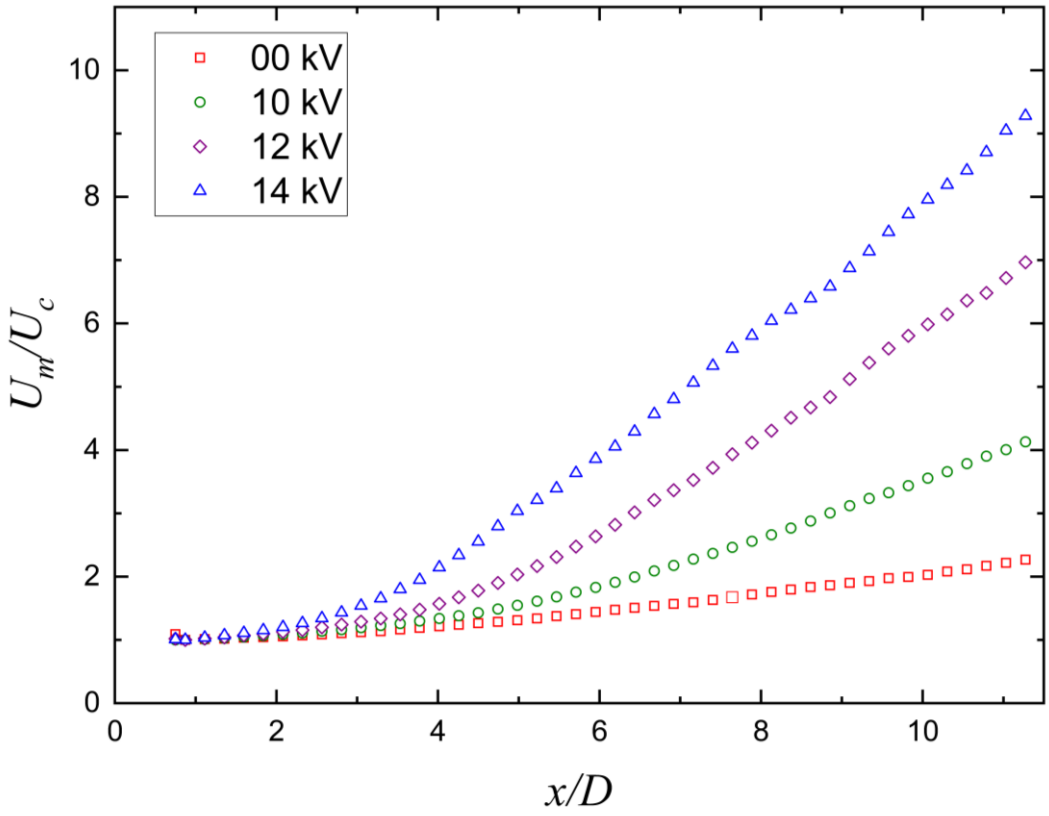

Figure 37 Streamwise decay of the ensemble-averaged normalised centreline velocity plotted against x/D. The APPJ without plasma (red square), with an input voltage of 10 kV (green circle), 12 kV (purple diamond), and 14 kV (blue triangle). The flow rate of helium is 2.5 SLM.

Focusing exclusively on the turbulent region, by only looking at the evolution of the velocity after the transition-to-turbulence of the APPJ. The normalised centreline velocity decay in the turbulent region is shown in Figure 38, only the plasma cases are present since the no plasma case in these conditions was laminar for the entire field of view. The turbulent region is defined with the $(x-x_t)/D$ streamwise axis, where x_t is the transition-to-turbulence point obtained from the normalised centreline velocity decay. The gradient of the velocity decay for an input voltage of 10 kV is noticeably smaller than the 12 and 14 kV independently of the flowrate. Except for the difference in the region's length, similarities are apparent under different initial conditions, such as 3.0 and 3.7 SLM at 14 kV, or the ensemble of the flow rates

at 10 and 12 kV. This result shows that the perturbations induced by the plasma are similar in intensity independently of the flowrate.

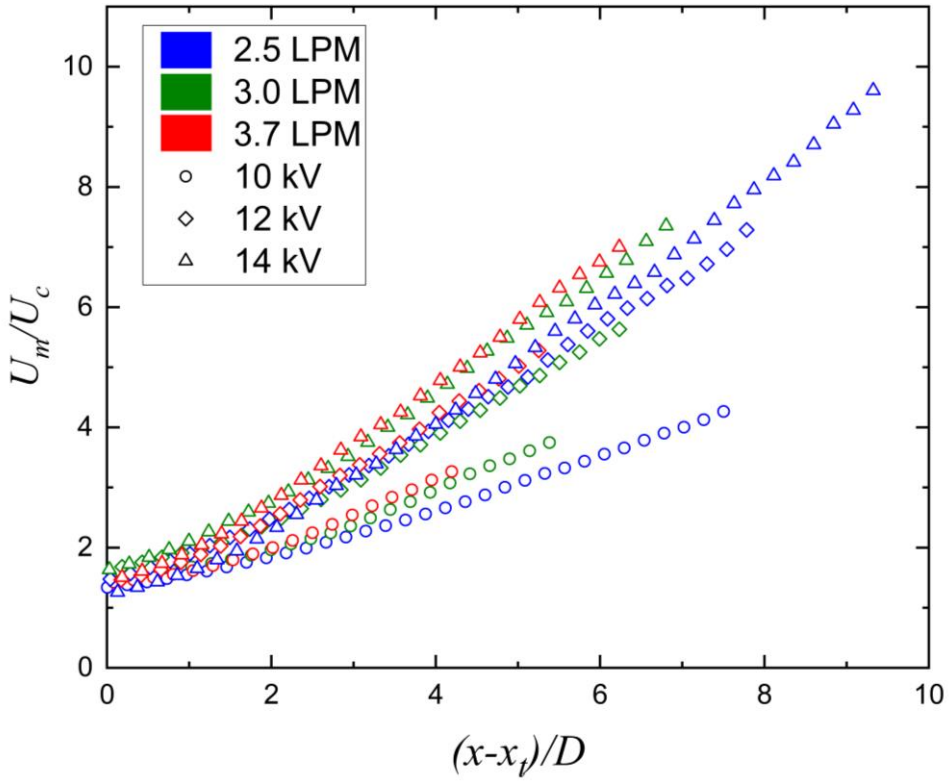

Figure 38: Streamwise decay of the ensemble-averaged normalised centreline velocity in the turbulent region plotted against $(x-x_t)/D$. (Circle), (Diamond) and (Triangle) represent respectively 10 kV, 12 kV, and 14 kV. (Blue), (Green)and (Red) represent the flow rates 2.5, 3.0, and 3.7 SLM, respectively.

To further understand the jet behaviour, the radial velocity at the various streamwise position are plotted in Figure 39 showing the radial normalised velocity profile at positions 6, 18, and 27 mm in the jet (x/D = 3, 6, 9) for: (a) without plasma, (b) 10 kV, and (c) 14kV and a flowrate of (Blue) 2.5, (Green) 3.0 and (Red) 3.7 SLM. The initial profile is Gaussian-like for all the cases as expected for a submerged jet in the transitional region. The influence of the flow rate was observed as a faster decrease of the velocity in the jet. The no plasma case has a slight evolution with a small decrease of velocity and wider jet spread. In the plasma-on cases, the Gaussian-like shape flattens as the jet transition into a turbulent state. The difference between the no plasma case and the 10 kV is a sharper decrease of velocity and a wider spread

at 18 mm and accentuate at 27 mm. In the 14 kV case, the velocity profile at 18 mm has a more advanced development than the 10 kV counterpart. At 27 mm, in the fully developed turbulent region, the shape of the velocity profile is almost flat and similar for all flow rates. The profiles show the jet evolving from a laminar non-buoyant to a turbulent buoyant state, with a similar pattern found in the literature.[164,165]

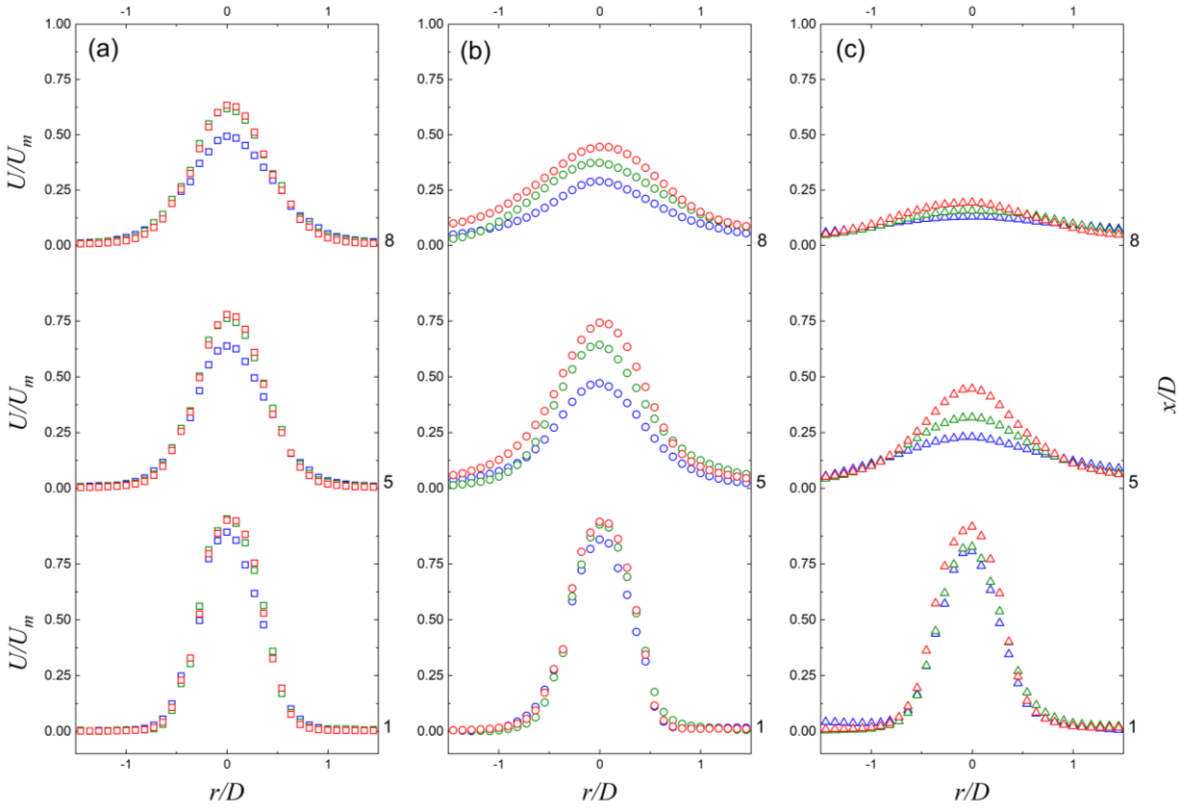

Figure 39: Ensemble-averaged normalised velocity profiles against the normalised radius r/D, at positions 3, 6, and 9 x/D for an APPJ (a) without plasma, with an applied voltage of (b) 10 kV, and (c) 14 kV. (Blue), (Green)and (Red) represent the flow rates 2.5, 3.0, and 3.7 SLM, respectively.

The growth of the jet radial was shown with the radial velocity profile, another means to observe this growth is the fluctuations of the jet radius. The half-radius is defined as $r_{0.5}/D = r/D(U_m/2)$ and reveals the growth of the jet spread along the jet axis. Figure 40 shows the half-radius fluctuations $r_{0.5}$ normalised by D for the applied voltages 0 kV, 10 kV, 12 kV, and 14 kV. The pattern is extremely similar to the normalised centreline velocity decay. The jet without a plasma discharge shows a linear increase in the half-radius along the jet-axis. In the

plasma-on cases, the initial increase of the half-radius is identical to the non-plasma case, although a gradient change is observed in the jet at different positions depending on the applied voltage, the higher the applied voltage the wider the spread. These gradients are consistent with the transition-to-turbulence of the jet. For the 12 and 14 kV cases, at respectively 30 and 26 mm, a bump can be observed, this is directly correlated to the shape of the jet in the presence of vortices and development of 'spade' shape, described in section 2.3.

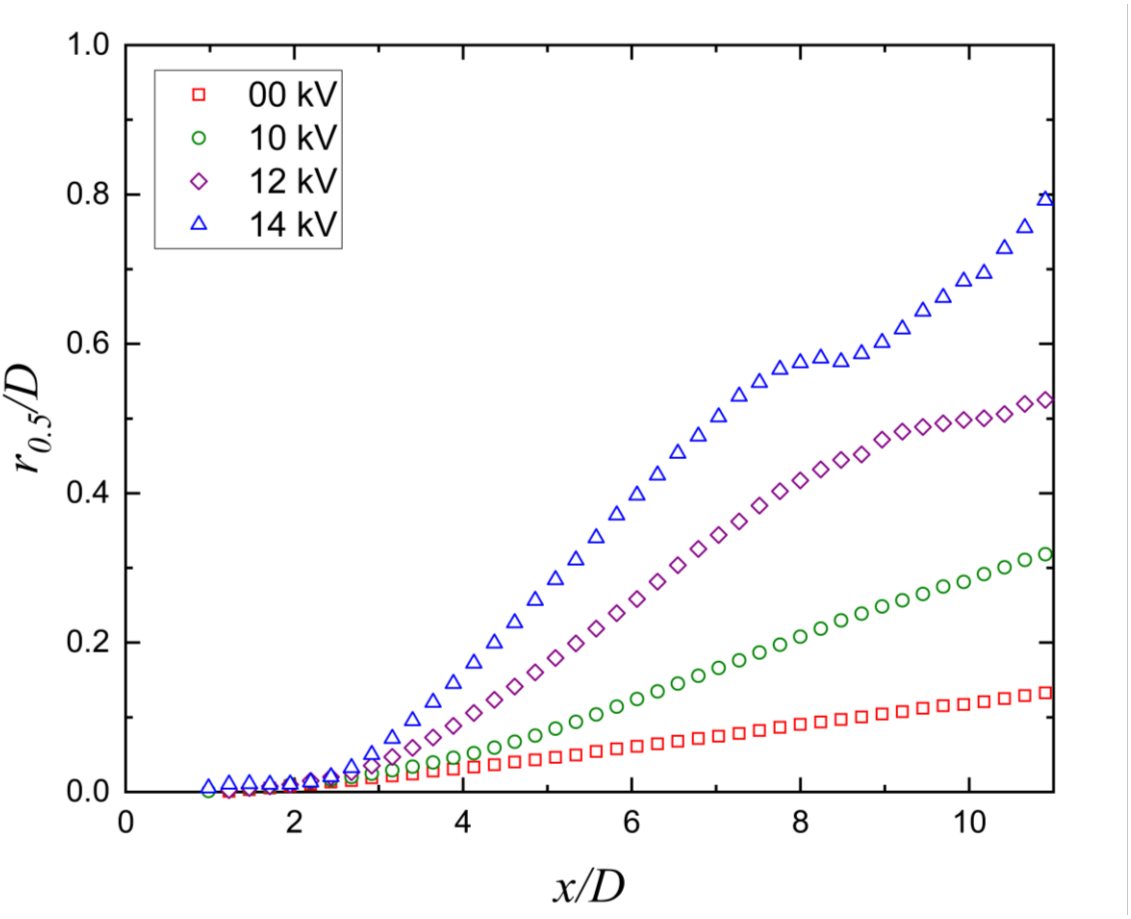

Figure 40: Normalised half radius fluctuations plotted against x/D. The APPJ without plasma (red square) and for input voltage 10 kV (green circle), 12 kV (purple lozenge), and 14 kV (blue triangle). The flow rate of helium is 2.5 LPM (Re = 147.5).

4.6 Transition-to-turbulence point

The half-radius variation and the centreline velocity decay offer a reasonable assumption of the transition-to-turbulence point; situated at the position of the change of gradient in the velocity decay. Figure 41 shows the transition-to-turbulence point from visual estimation with Schlieren Photography and the PIV measurements, and the visible plasma plume length measured. The uncertainty on the Schlieren measurements are higher as expected; however, the comparison reveals a close match with the PIV measurements. This observation comforts the assumption that the injection of seeding particles into the jet has little to no impact on fluid dynamic behaviour. As demonstrated in section 4.3 and 4.4, the laminar length decreases with the increase of the applied voltage at a fixed flow rate of 2.5 SLM, whereas the length of the plasma plume increased. Although the turbulence generated in the APPJ expanding in ambient air increased at 14 kV, the plasma plume is longer due to the increased applied voltage.

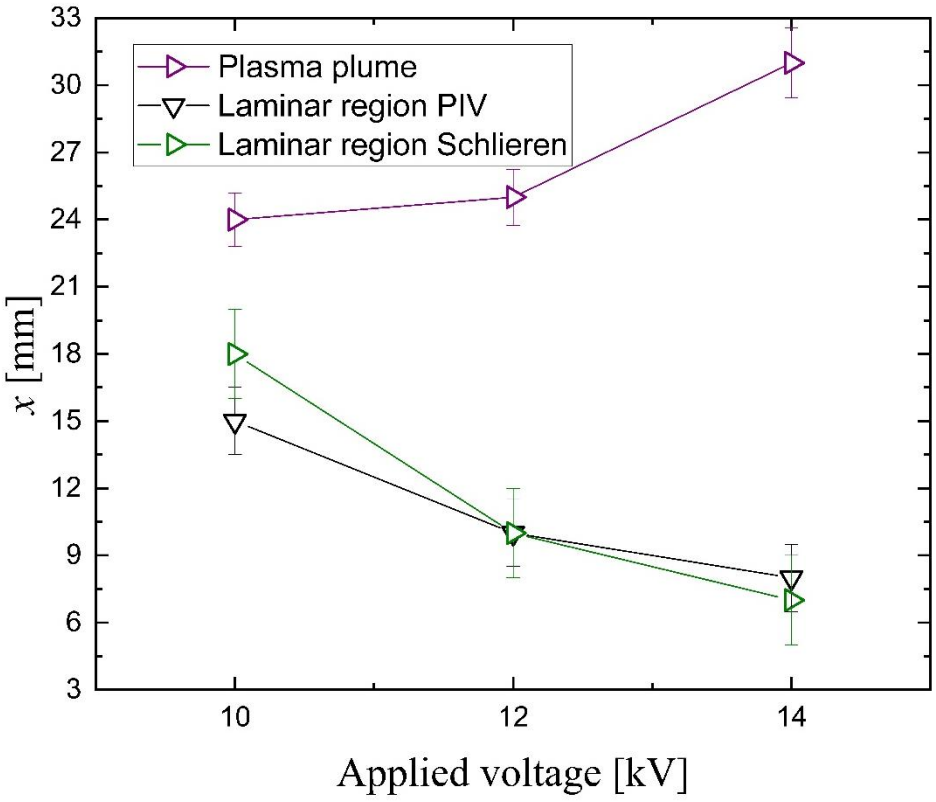

Figure 41: A comparison of plasma plume length, laminar region length obtained with Schlieren Photography, and PIV against the applied voltage for a flow rate of 2.5 SLM.

The measurement of the laminar region length was done for the entire set of PIV experiment, in all investigated cases the laminar length region increases with the flow rate and decreases with the applied voltage, the results are shown in Figure 42. The influence of the applied voltage is consistent in the sense that the 12 kV case is always between 10 and 14 kV. The lowest flow rate has the smallest laminar region length, whereas the highest flow rate has the longest.

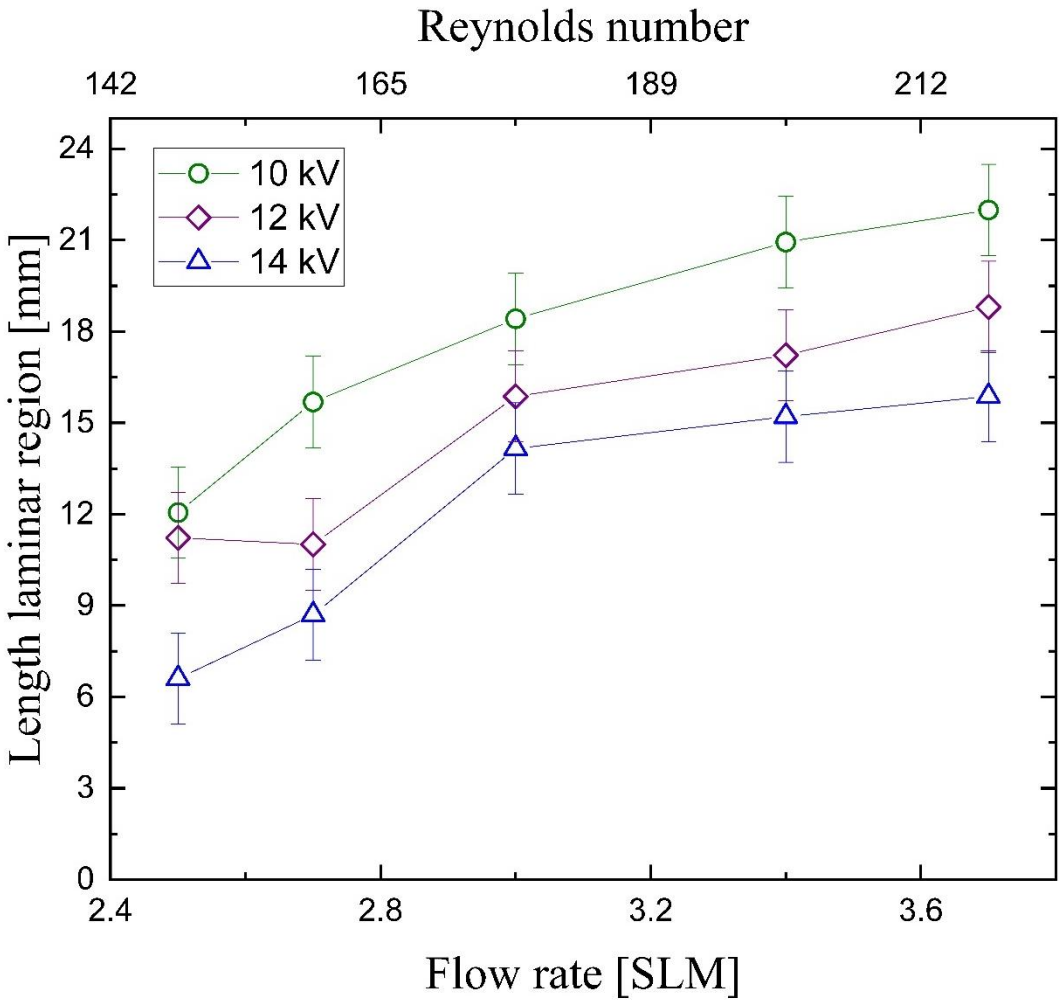

Figure 42: Length of the laminar region plotted against the flow rate and Reynolds number. For voltage input of 10 kV, 12 kV, and 14kV.

4.7 Radial and streamwise intensity of turbulent fluctuations

The turbulent intensity of velocity fluctuations streamwise and radial, Reynolds stress, and turbulent kinetic energy are calculated as described in section 2.3. In all the investigated cases, without the plasma, slight velocity fluctuations are observed on the edges of the early developing jet, with plasma, a trend is observed, for higher applied voltage the fluctuations are more intense and happen earlier in the jet. Figure 43 show the several components mentioned, $\boldsymbol{u}_x'$, $\boldsymbol{u}_r'$, $-\boldsymbol{u}_x'\boldsymbol{u}_r'$ and $\boldsymbol{k}$ for an applied voltage of 14 kV and a flow rate of 2.5 SLM. The radial component is very weak at the exit of the jet and that the highest intensity is mainly on the

edges of the jet until the transition to a turbulent state. The streamwise component is also very weak at the exit of the jet, except on the edges where the fluctuations are developed in two channels in the fragile shear layer of the jet. The intensity layers are concentric with the centre being the peak and are situated before the measured transition-to-turbulence point, revealing the presence of turbulence in the laminar region of the jet. Notably, the streamwise component is around four times higher than the radial component. The comparison with the no plasma case shows that the fluctuations are directly caused by the plasma discharge. The Reynolds stress demonstrates the production of turbulence in the jet, since it is the product of the streamwise and radial turbulent intensity of velocity fluctuations, it gives more importance to the radial component which is much smaller intensity. Figure 43 shows the Reynolds stress, where the two zones of turbulence production are identified, these zones are situated in the laminar region and on the edges of the jet, no intensity is seen in the centreline. The turbulent kinetic energy is very similar to the streamwise turbulent intensity of velocity fluctuations, as the component is stronger than its radial counterpart. Looking at the absolute value, the fluctuations show an unstable state in the laminar region, the several components show an origin of the fluctuations in the shear layers of the jet close to the capillary, and growth in size gradually evolve up to a peak situated in the laminar region.

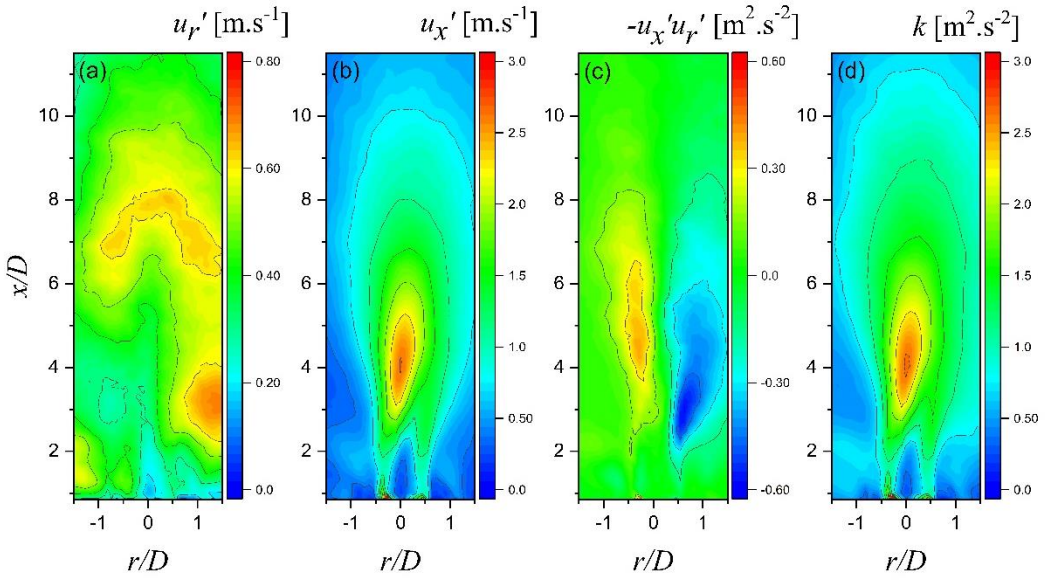

Figure 43: (a) Radial and (b) streamwise turbulence intensity of velocity fluctuations, (c) Reynolds stress, and (d) turbulent kinetic energy contour for an APPJ with an applied voltage of 14 kV and a flow rate of 2.5 SLM.

In order to put the turbulence intensity of velocity fluctuations into perspective, in relation to the flow velocity, the components are normalised with the centreline velocity; $\boldsymbol{u_x'/U_c}$, $\boldsymbol{3u_r'/2U_c}$, $\boldsymbol{-u_x'u_r'/U_c^2}$ and $\boldsymbol{k/U_c^2}$ following the literature and are shown in Figure 44.[35] The results are very different from those previously observed in Figure 43. The normalised radial component intensity increases in the jet from the transition-to-turbulence, the intensity is layered, and reach the highest value the furthest. The normalised streamwise component has a slight intensity close to the capillary on the edges of the jet, and form not well define concentric intensity layers as the intensity extends outside the field of view. However, the small region of peak intensity corresponds to the transition-to-turbulence point measured, when the absolute streamwise component intensity was higher in the laminar region. The relative intensity was found to be higher with lower flow rates, as shown in Appendix A. The intensity of the normalised Reynolds stress is in the turbulent regions, where two zones are identified on the edges of the jet and the centre of the jet is excluded, due to the absence of radial fluctuations. The turbulent kinetic energy calculated has intensity layers in the V shape which gradually

increase in intensity in the jet. The normalised turbulence components emphasized the turbulent region where the fluctuations are intense in comparison to the centreline velocity. In opposition to the absolute turbulence components which revealed the strong fluctuations in the laminar region of the jet. This development is coherent with the generation and propagation of perturbations on the shear layer par to the jet, close to the capillary, described in section 2.2.

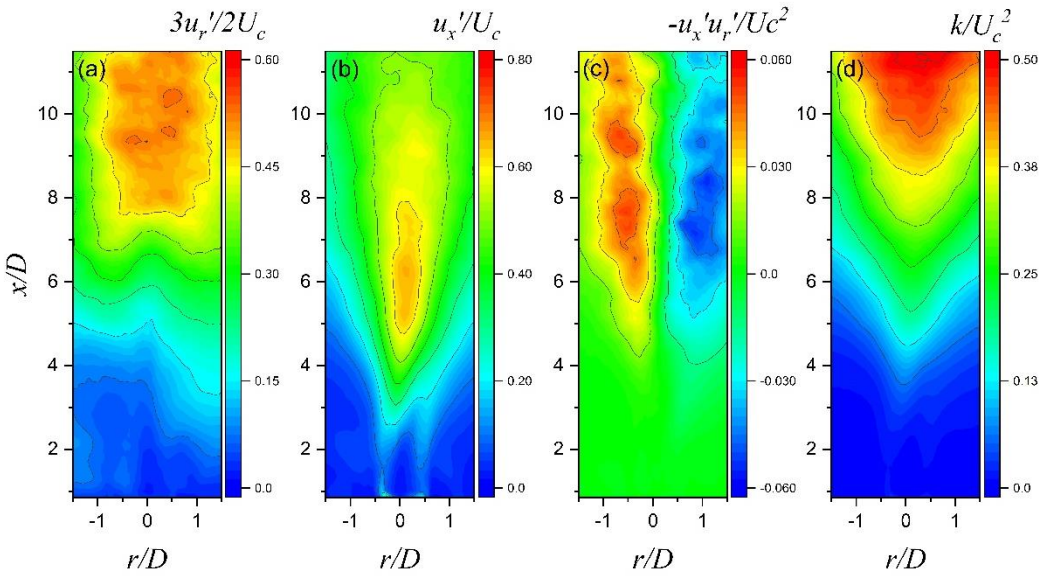

Figure 44: Normalised (a) Radial and (b) streamwise turbulence intensity of velocity fluctuations, (c) Reynolds stress, and (d) turbulent kinetic energy contour for an APPJ with an applied voltage of 14 kV and a flow rate of 2.5 SLM.

4.8 Conclusion

This chapter explored the effect of the plasma discharge on the flow field of a sinusoidal-driven APPJ. The measurements of the velocity flow field with the PIV provided quantitative insights on the flow structure and the plasma-induced velocity fluctuations. Firstly, the qualitative observation of the visible plasma plume and flow structure assessed the effect of the applied voltage and the flow rate on the APPJ. Secondly, the measure of the velocity at the exit of the capillary offered valuable information on the plasma-induced velocity increase, however, the increase observed was <10% of the exit velocity. In the case of very low

Reynolds, this information is important, as the transition into a turbulent state cannot be induced by the velocity increase itself. Then the velocity and turbulence components provided insights on the generation of turbulence in the APPJ.

The centreline velocity decay showed the effect of the plasma-induced turbulence on the velocity and its consequential transition into a turbulent state. The laminar region decreased when higher voltages were applied, showing a connection between the intensity of the turbulence and the applied voltage. On the opposite, the flow rate effect was also assessed, and a stronger flow rate was more difficult for the plasma to disturb. The influence of the applied voltage and the flow rate was characterised for the sine-driven APPJ.

Furthermore, the calculation of the turbulent kinetic energy k and the turbulence intensity of velocity fluctuations, and the Reynolds stress showed the important generation of turbulence in the laminar region of the jet. The information on the stability of the laminar region is crucial, it reinforces the idea that perturbations are generated in the shear layer of the jet at the exit of the capillary and propagate and grow along the jet. Moreover, it reveals the possibility of strong air entrainment and mixing in the laminar region which was unexpected. These perturbations are expected to be produced by the EHD and gas heating phenomenon occurring in the discharge. An increase of the applied voltage participates in a stronger effect from both, with an expected stronger electric field and higher gas temperature.[166] The gas heating is expected to be the major component affecting the stability of the jet.[103] However, the information from the velocity measurements does not allow a finer deduction.

Since the influence of the applied voltage on the structure of the APPJ was assessed, an increase in the entrainment of air and mixing of the noble gas is expected. Consequently, the

next chapter looks at the gas mixing and chemistry in the APPJ in order to provide a further understanding and control of the complex interaction of APPJ and the ambient air.

Chapter 5 Turbulence and entrainment in an atmospheric pressure dielectric barrier plasma jet.

Some of the results presented in this chapter have been published in Plasma Process and Polymers, 2020; Y. Morabit, R. D. Whalley, E. Robert, M. I. Hasan & J. L. Walsh. **'Turbulence and entrainment in an atmospheric pressure dielectric barrier plasma jet.'**[167] *Plasma Processes and Polymers* 2019;e1900217 DOI: 10.1002/ppap.201900217

5.1 Introduction

This chapter investigates the entrainment of air into the APPJ and explores the hypothesis that the plasma-induced perturbations present in the laminar region increase the entrainment of air.

In order to characterize the production of chemical species in the jet, multiple invasive and non-invasive diagnostic techniques have been proposed, including tunable diode laser absorption spectroscopy (TDLAS),[168] mass spectroscopy (MS),[169] Fourier transform infrared spectroscopy (FTIR),[170] Laser-Induced Fluorescence (LIF) and Two-photon Absorption Laser-Induced Fluorescence (TALIF).[162,171,172] Of all the techniques investigated, LIF based methods are particularly convenient as they provide the high spatiotemporal resolution required to accurately investigate the complex downstream chemistry in a plasma jet while facilitating the quantification of absolute radical densities. Regardless of the diagnostic technique used, it is clear that a significant proportion of the reactive chemical species produced within the downstream region of the jet are a result of reactions between the noble gas plasma and

molecular gas impurities entrained from the surrounding environment, which is typically humid air. Given that the interplay between the propagating plasma plume and the ambient environment has a considerable impact on the physicochemical properties of the plasma jet and, therefore, on the application efficacy, understanding the underpinning mechanisms of how air becomes entrained within the flowing noble gas channel is of vital importance.

5.2 Experimental and computation methodology

The plasma jet used in this study was already described in section Chapter 3 and the metallic strip electrode acted as a ***floating ground*** electrode. Two applied voltage cases were examined in this study, 10 and 14 kV with a frequency of 20 kHz. Helium gas flowed through the capillary at 2 SLM, giving a maximum exit velocity, U_m, equal to 9.4 $m.s^{-1}$.

The PIV measurements to quantify the flow field disturbed by the plasma discharge were undertaken using the experimental setup described in section 3.4. Δt was set to 30 μs, the spatial dimensions of the grid were 350 μm^2. Each dataset comprised of 800 frames, 400 vector maps were averaged and presented as a single figure.

The Rayleigh scattering technique is described in section 3.5. The LIF technique is described in section 3.6.

5.3 Preliminary measurements

The precedent Chapter focused on the fluid dynamics of the APPJ, and the velocity fluctuations. These results were obtained with a grounded electrode, unfortunately, the limitations of the Rayleigh scattering and LIF configurations forced the use of a floating

electrode to avoid arcing. This change affects the plasma discharge heavily, thus to provide supplementary data, measurements with a floating electrode were done.

Without a plasma discharge, the undisturbed helium flow appeared laminar over the entire measurement region, confirmed by the ensemble-averaged centreline velocity (U_c) profile in Figure 45 (d). On the application of a 10 kV sinusoidal waveform, a weak discharge was observed to form, indicating gas breakdown had been achieved; under such conditions, little obvious change to the velocity profile was observed. An increase in applied voltage from 10 kV to 14 kV led to an increase in the length of the visible plasma plume. Comparing Figure 45 (b) and (c) highlights the impact of the applied voltage on the flow structure downstream of the jet orifice, with the higher applied voltage resulting in a significant reduction in the length of the laminar flow region. From the ensemble-averaged centreline velocity, an abrupt change in gradient is observed at approximately 8 x/D, indicating a transition to turbulence.

In absolute terms, the generation of plasma with an applied voltage of 14 kV was found to increase U_m by 0.94 m s^{-1}, representing a relatively modest increase of approximately 10% compared to the 0 kV case. Such increases in velocity are in line with those predicted by others and are a consequence of gas heating and electrohydrodynamic forces induced by the plasma, with the latter mechanism being the most likely dominant factor.[60,103] Past studies on turbulence generation in axisymmetric round jets have revealed that turbulence initiates due to instabilities within the shear layers at the jet exit that become amplified as they travel downstream.[115,119,127,128,140] As the instabilities grow, they cause velocity fluctuations, Reynolds shear stresses, and thus the production of turbulence.[103] Many previous studies have explored 'excited' jets that employ alternative means to perturb the jet flow with an eye to investigating the mechanisms of turbulence generation.[113,117,118,121,173,174]

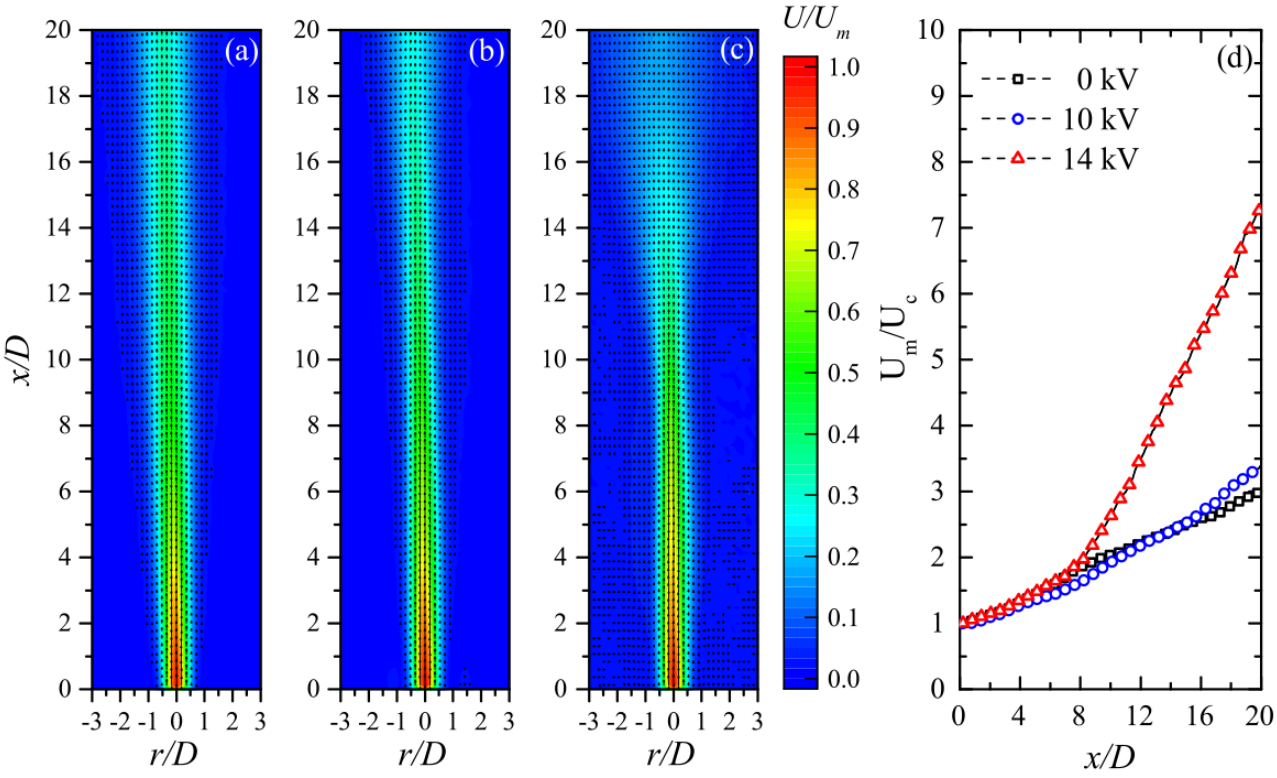

Figure 45: Ensemble averaged particle imaging velocimetry measurements of the plasma jet obtained at applied voltages of (a) 0 kV, (b) 10 kV, and (c) 14 kV, (d) shows the ensemble-averaged centreline velocity (U_c) normalised to U_m.

5.4 Entrainment and mixing

While the growth of small-scale instabilities within the jet shear layer has a significant impact on the laminar to turbulent transition, they also provide a mechanism to enhance entrainment of quiescent air into the laminar region of the plasma jet.[174] The turbulence kinetic energy *k* was calculated from the time-averaged intensity of the turbulence fluctuations in the jet, from which the eddy viscosity μ_T was calculated as described in Appendix D1. The eddy viscosity profiles for the two plasma cases investigated in this work are shown in Figure 46(a-b). Close to the jet orifice, a region of low μ_T exists, which can be explained by the fact that this is the laminar region where the amplitude of velocity fluctuations is small, leading to low turbulent kinetic energy *k*, and consequently, a low μ_T. The second zone (observed from 4 –

10 x/D in Figure 46) coincides with the transition region, as inferred in Figure 45(d), where the value of μ_T peaks. This is attributed to the large scale fluctuations/eddies starting to appear in the shear layer of the jet, leading to high turbulent kinetic energy *k*, considering that such large fluctuations live long enough to be transported downstream, the dissipation rate of the turbulent energy ε is relatively low in this region, thus leading to a peak of μ_T. The third zone (e.g. > 10 x/D) coincides with the turbulent region which has a moderate value of μ_T. The large eddies generated in the transition region break into smaller eddies in the fully turbulent region, the small eddies are dissipated into heat due to the physical viscosity of the fluid.[175] In this sense, the turbulent kinetic energy *k* is high, while the turbulent dissipation rate ε is also high, leading to a moderate value of μ_T.

From Figure 46(a-b), it is clear that the eddy viscosity for the 14 kV case has a larger magnitude compared to the 10 kV case, which is consistent with the PIV results presented in Figure 45. When comparing the average value of μ_T in zone one (x/D < 4) for both cases it is found that μ_T for the 10 kV case is approximately 70%-80% of that for the 14 kV case, indicating that the plasma's perturbation of the flow in the laminar region is more significant for the 14 kV case in comparison to the 10 kV case.

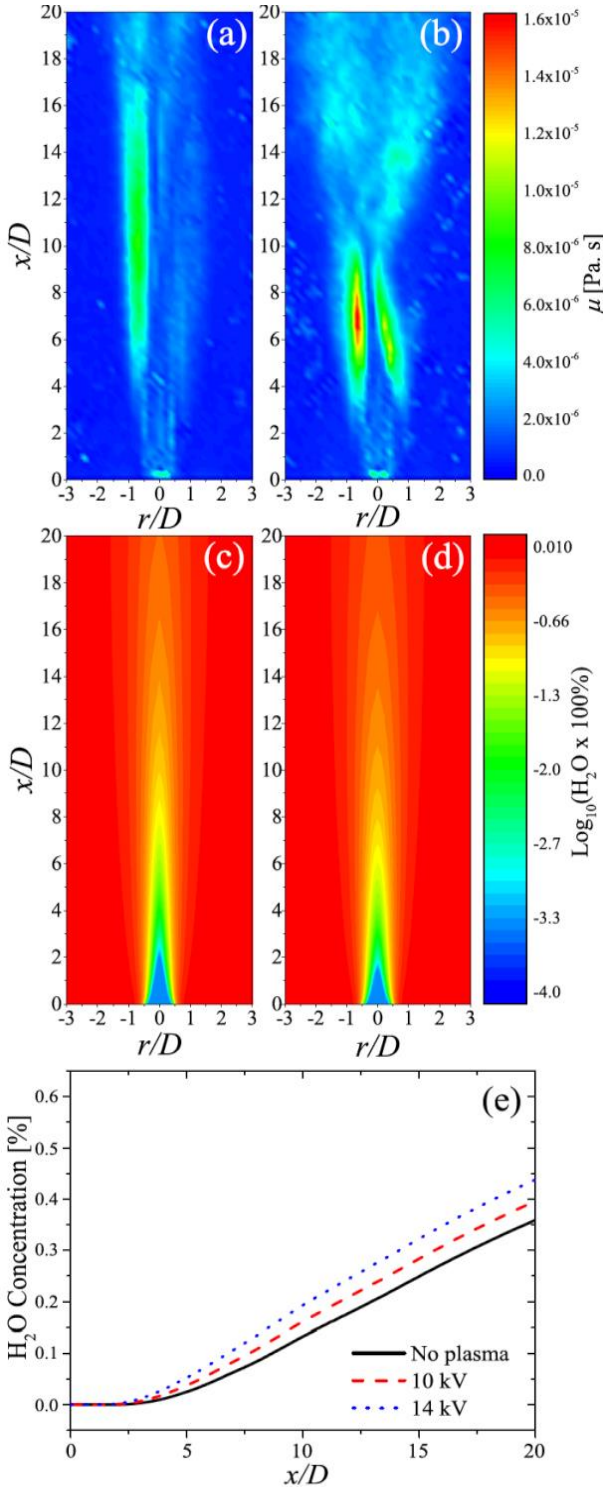

Figure 46: Eddy viscosity calculated from PIV measurements for the (a) 10 kV and (b) 14 kV excited plasma jet and the calculated percentage of H_2O in the helium flow under (c) 0 kV and (d) 14 kV conditions; (e) shows the percentage of H_2O along the jet centreline.

A higher value for the eddy viscosity indicates a higher value of eddy diffusivity, D_T, which adds to the physical diffusion coefficients, leading to increased entrainment of air into

the helium flow. To highlight the impact of the plasma-induced entrainment, Figure 46(c) and (d) show the computed percentage of H_2O in the gas mixture for the 0 kV and 14 kV cases, respectively. Notably, the 0 kV case represents an unperturbed laminar flow where quiescent air is entrained due to physical diffusion only. While in the case of the perturbed flow, air entrainment occurs due to physical diffusion plus the "effective" eddy diffusion due to turbulence. The centreline concentration of H_2O at the jet exit in both cases was set to 0.00004% in the computer simulation, a value obtained from the helium gas provider. Moving downstream to 2 x/D, the level of H_2O in the unperturbed 0 kV case was found to increase to be approximately 0.0005 %. In contrast, the H_2O concentration in the perturbed case was found to be 0.0034 %, representing a 7-fold increase. Further downstream at 6 x/D, the H_2O concentration in the unperturbed case was found to be 0.046%, compared to 0.082% in the perturbed case, representing a 1.8-fold increase. When moving downstream, the difference between the unperturbed case and the 14 kV perturbed case diminishes as a result of the increasing density of the gas mixture, which lowers the value of the eddy diffusivity.

In order to further investigate the impact of the plasma-induced turbulence on the mixing of the neutral gas, the use of Rayleigh scattering was used to provide an estimation of the helium mole fraction downstream of the jet orifice. Unfortunately, the measurement could not be done with 2 SLM, results obtained with 4 SLM are shown in Figure 47.

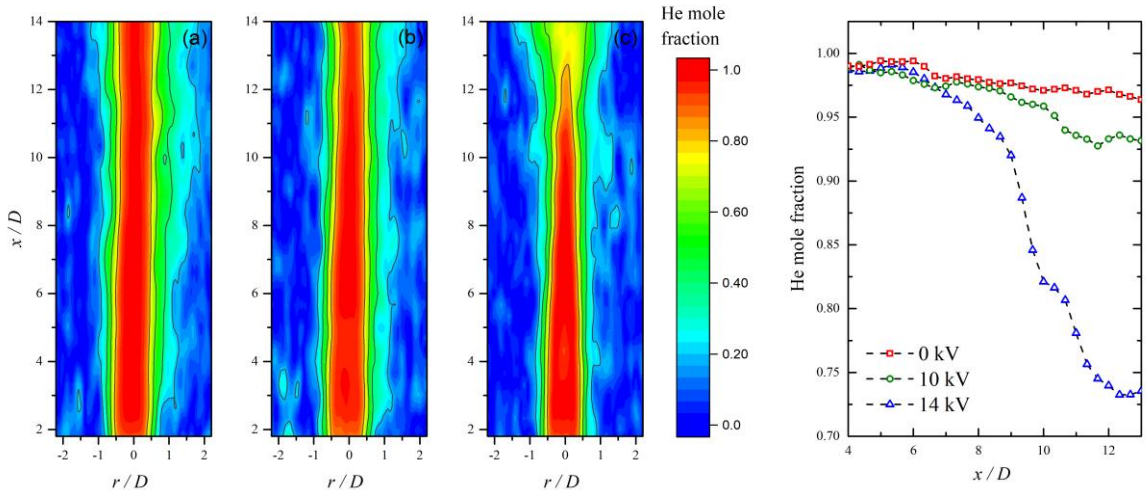

Figure 47: Averaged measurement of helium mole fraction of an APPJ with an applied voltage of (a) 0 kV, (b) 10 kV, and (c) 14 kV at 4 LPM. Part (d) shows the helium mole fraction along the centreline of the jet.

The calculated helium mole fraction obtained from Rayleigh scattering measurements conducted at a flow rate of 4 SLM with an applied voltage of 0 kV, 10 kV, and 14 kV is shown in Figure 47. The averaged measurement of helium mole fraction along the APPJ, shown in Figure 47 (d), highlights the influence of plasma generation on air entrainment into the flowing helium. The results are in line with those presented in chapter 4 that show an increased applied voltage enhances the generation of turbulence in the jet, even in the laminar region, and decreases the length of the laminar region. Without plasma, the helium mole fraction at the centre of the jet decreases at a very slow rate, it is attributed to the diffusion of air. The width of the very high helium mole fraction section of the jet does not reduce significantly, shown with the colour Red in the contour. In opposition, for the plasma-on cases, the width reduces along the jet, and it is entirely reduced for the 14 kV case. The longer laminar region length is consistent with observations on the influence of higher flow rate on the structure of the jet, shown in chapter 4. Furthermore, an applied voltage of 14 kV influences the helium mole fraction significantly with a reduction of up to 20% in comparison with the 10 kV case. A

significant decrease in the helium mole fraction can be observed even within the laminar region, reducing from 0.98 to 0.80. As this region is before the laminar-turbulent transition point, this finding indicates that diffusion alone cannot account for the entrainment of air within the flowing helium, the turbulent entrainment plays a major role in the 14 kV case.

5.5 OH fluorescence decay rate and absolute density

The decay rate of the LIF signal from OH provides a sensitive indication of the helium-air mixing ratio as the quenching rate of the laser-excited state is strongly influenced by the density of quenching species present within the flowing helium gas (e.g., N_2, O_2, H_2O).[158] The measured LIF decay rate described the plasma-induced entrainment and quantifying the absolute OH density downstream of the jet exit.

Figure 48 shows the normalized LIF intensity measured for delay times between 60 and 1500 ns for both applied voltages along the plasma jet expanding outside the capillary into the ambient air. The first delay was found the highest intensity signal. The decay rate increased significantly when moving downstream of the jet orifice, signifying an increased density of quenching species. Furthermore, it was observed that for any given spatial location, the LIF intensity decay rate was greater with a higher applied voltage, indicating that applied voltage has a significant impact on the entrainment of air into the helium flow, a finding in close agreement with those obtained from Rayleigh measurements.

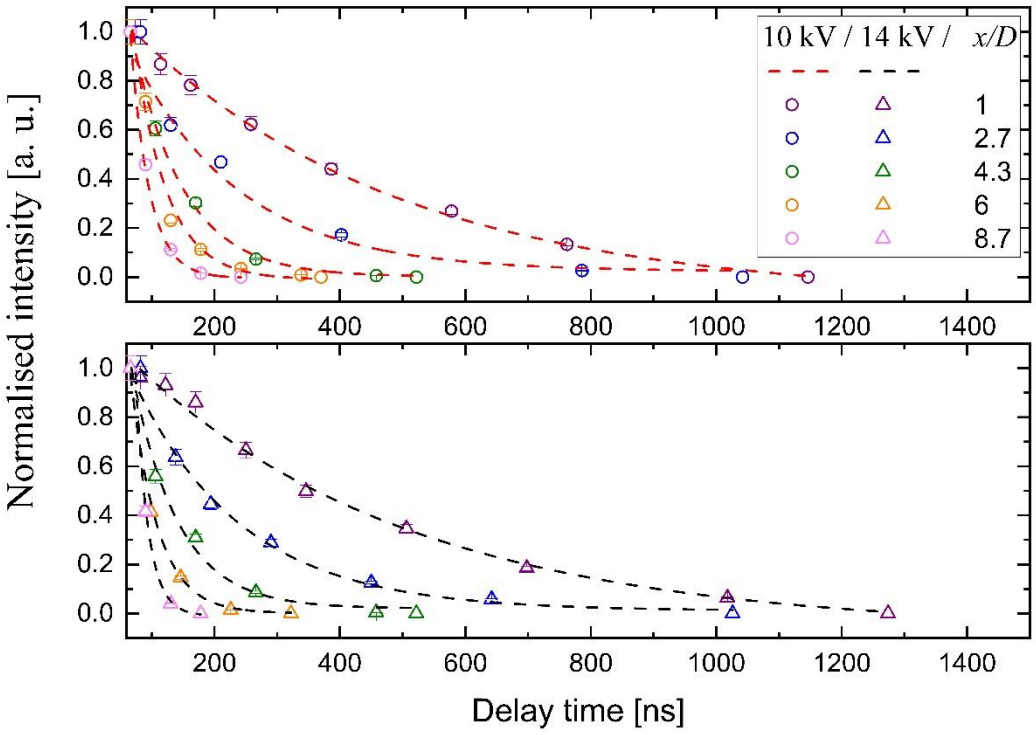

Figure 48: LIF normalised intensity against delay time, with exponential decay fit for (top) 10 kV and (bottom) 14 kV at various positions x/D along the jet.

The decay rate was obtained with an exponential decay fit of the LIF intensity plotted against the delay time, as described in section 3.6. Figure 49 shows the measured LIF decay time as a function of downstream spatial position for both the 10 kV and 14 kV cases; compared with a computed LIF decay time model described in Appendix B. Additionally, the hypothetical decay time for an unperturbed laminar helium flow is shown. The LIF decay time is shorter at all spatial positions under both 10 and 14 kV excitation compared to what would be observed under idealized laminar conditions. The plasma generation increases air entrainment, which acts to increase the density of quenchers and thus increase the quenching rate of the OH fluorescent state. This result provides experimental evidence supporting the hypothesis that plasma generation increases the entrainment of air within the APPJ at all spatial positions. The calculated decay times closely match the measured data points, with both cases showing excellent agreement.

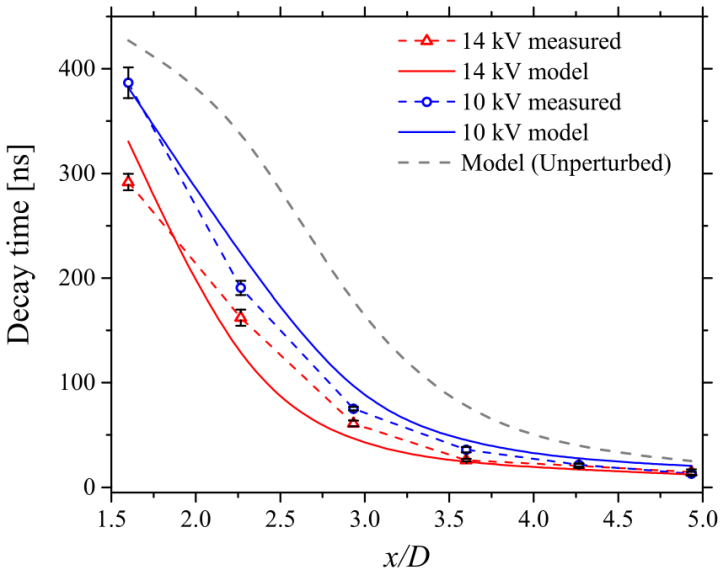

Figure 49: Comparison between measured and calculated decay time of the laser-induced fluorescent signal as a function of downstream distance from the jet orifice.

Figure 50 shows the 2D LIF emission profile was compiled for both the 10 kV and 14 kV. The centreline LIF intensity obtained from the 2D profile was compared to a computed LIF intensity using a model described in Appendix B. Consistent with the observations made in many previous studies, an increase in applied voltage was observed to increase the peak OH density within the plasma plume.[163] Given that hydrogen-based species densities increase when the air/water vapour fraction increases,[135] it becomes likely that an increase in the applied voltage results in an increase in OH density as a result of not only more intense discharge conditions but also increased entrainment of air and H_2O. Critically, the position of peak OH density was found to vary depending on the applied voltage.

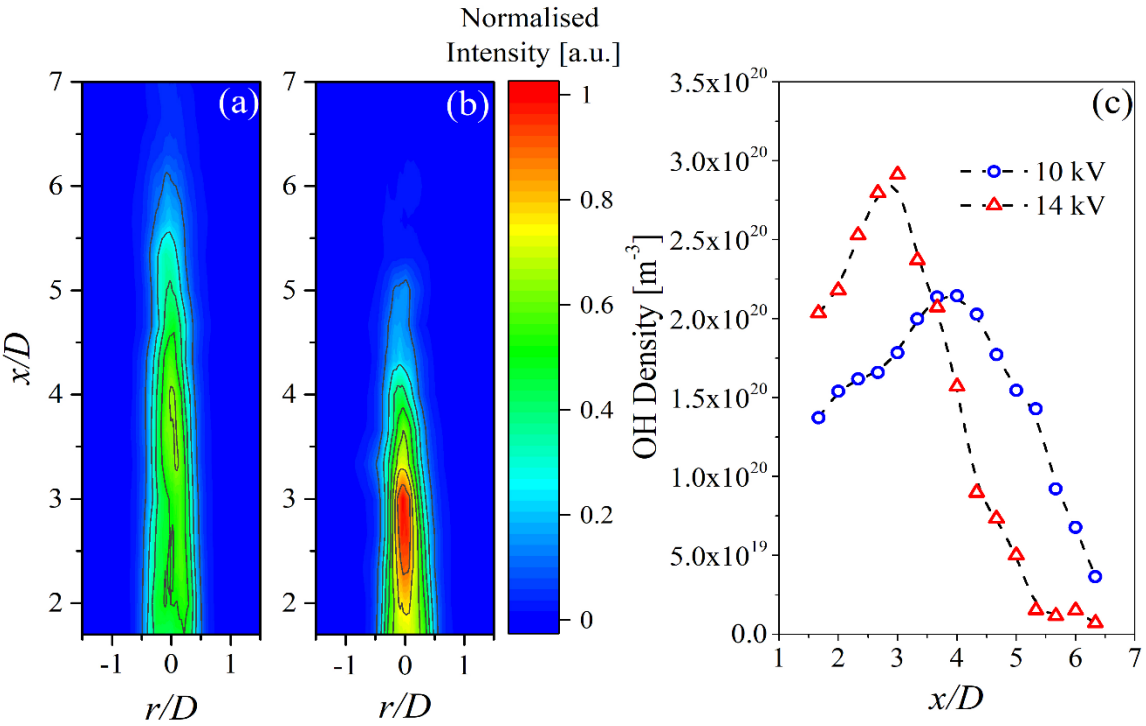

Figure 50: Composite 2D normalised LIF intensity for (a) 10 kV, and (b) 14 kV case. Absolute centreline OH density for the 10 kV and 14 kV case as a function of distance from the jet orifice.

This phenomenon is attributed to the interplay between the physical properties of the plasma (i.e., n_e and T_e) and the fluid dynamics of the APPJ. With an applied voltage of 14 kV, perturbations within the jet shear layer caused by plasma generation induce an early transition to a turbulent flow regime. Under such conditions, the generation of OH close to the jet exit is locally enhanced due to enhanced H_2O entrainment combined with the relatively intense discharge conditions. Beyond the local maxima, the elevated air mole fraction as a result of the induced turbulence acts to quench the discharge and thus impedes OH generation. Conversely, at the lower applied voltage of 10 kV, the discharge is comparatively less intense, meaning less air entrainment, and a weaker plasma is formed, both factors contributing to limit OH production. However, less shear layer perturbation causes less air entrainment into the helium flow; thus, the discharge can propagate further from the orifice. Consequently, the

concentration of ground-state OH is significantly higher far downstream from the jet exit in the 10 kV case compared to the 14 kV case.

The presented findings have considerable implications from a practical perspective as it has been demonstrated that the density of OH at a given downstream position is strongly influenced by both the discharge characteristics and its interaction with the quiescent background gas. While it is generally assumed that a higher plasma generation voltage results in enhanced production of OH, the results clearly show that this only holds true close to the jet orifice. With increasing voltage comes increasing turbulence and air entrainment, which ultimately begins to quench the discharge and negatively affects downstream OH production. Counterintuitively, there is an order of magnitude more OH created in a plasma jet generated using 10 kV compared to one generated using 14 kV excitation at a position of 5.3 x/D (i.e. 16 mm from the jet exit).

To provide further insights on the spatial distribution of the generation of OH in the plasma jet, a measurement using LIF in the radial direction was obtained. The resulting 3D profile at 2.7 x/D from the exit of the tube is shown in Figure 51, it shows the density of OH in the plasma jet, a specificity observed in the presence of a gap of intensity in the heart of the jet, it is explained by the ‘doughnut’ shape of the plasma bullet. Figure 52 shows a position further along the jet, at 7.7 x/D from the tube exit; this corresponds to the non-visible part of the plasma plume. The intensity measured of OH shows a more restrained shape, with a peak density that is only half that measured at x/D= 2.7. It can also be explained by the plasma ‘bullet’ shape as it becomes more ‘homogeneous’ away from the capillary and reduces in size while travelling.

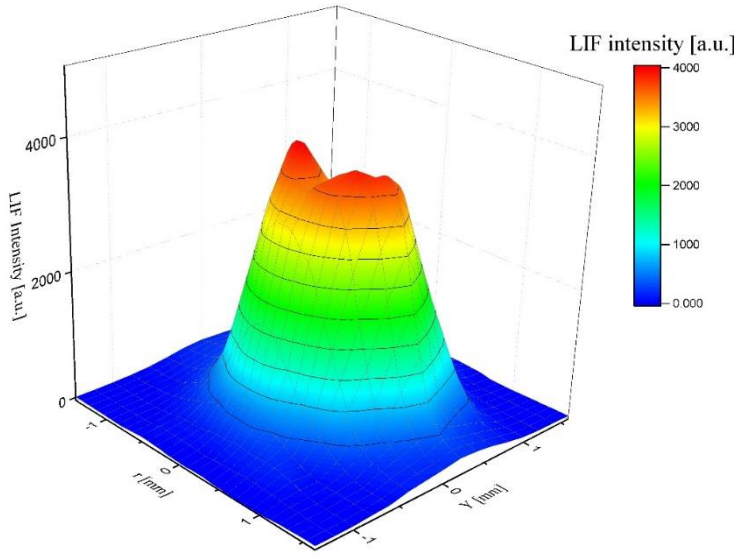

Figure 51: LIF intensity measurements across the jet at a position of 2.7 x/D (8 mm) from the tube exit.

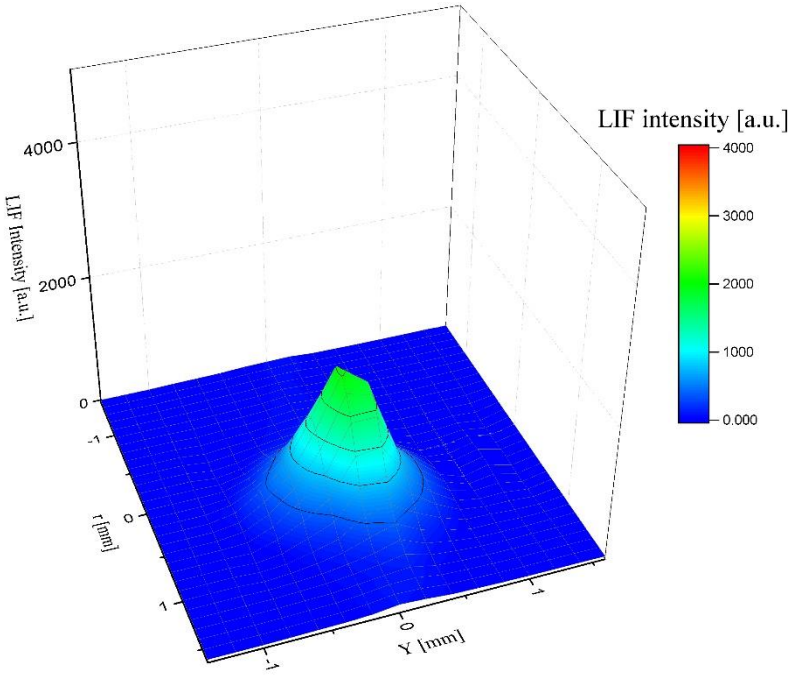

Figure 52: LIF intensity measurements across the jet at a position of 8.7 x/D (23 mm) from the tube exit.

5.6 Conclusion

This Chapter has employed PIV, LIF, and Rayleigh scattering to explore the interplay between the propagating plasma plume and the quiescent background air in an axisymmetric dielectric barrier discharge jet. The Rayleigh scattering measurements of the helium mole fraction along the APPJ showed the influence of the plasma generation on the mixing of the neutral gas into the ambient air. The decrease of helium mole fraction in the laminar region of the APPJ reveals the major influence of the plasma-induced air entrainment in comparison to the diffusion of air. The helium mole fraction showed a significant decrease for the 14 kV applied voltage case in comparison to the 10 kV. These observations are in line with the conclusion of Chapter 4, where the plasma-induced turbulence was identified in the laminar region.

The measured decay time of the LIF state of OH was compared against a predicted decay time and found to be in good agreement. The OH production is strongly influenced by the interplay between the propagating plasma and the background air. Moreover, the increase of H_2O in the jet can be correlated to the production of OH. At high applied voltages, OH density increases close to the exit but is rapidly reduced downstream as a result of the elevated air content quenching the discharge. This point has been further shown with spatial profiles along the jet.

In summary, this study demonstrates an intricate link between the physicochemical properties of the plasma and its interaction with the quiescent air. Following the conclusions of the last chapter, the chemical reactions are heavily affected by the plasma-induced turbulence in the laminar region. While the purpose of the APPJ does not change, the understanding behind its usage is clearly in question. As many applications rely on the presence of reactive oxygen and nitrogen species, which are predominantly formed when the plasma

interacts with the background environment. The presence of air entrainment in the laminar region transforms the chemistry fundamentally. The results of this study provide valuable insight into the underpinning mechanisms governing these interactions.

Chapter 6 Impact of pulse characteristics on the fluid dynamics of an APPJ.

Some of the results presented in this chapter have been used to create a draft paper to be submitted to J. Phys D.

Y. Morabit & J. L. Walsh. **'Optimization and control of low-temperature atmospheric pressure pulse driven plasma jet.'**

6.1 Introduction

A pulse-driven APPJ offers more control over the electrical parameters generating the plasma discharge. While most jets are excited using sinusoidal excitation configurations, it is difficult to investigate the electrical parameters. The operating frequency is often constrained by the power supply and cannot investigate the impact of polarity and duty cycle. This study offers to investigate sub-µs pulsed-driven APPJ where parameters can easily be varied to overcome these challenges. The first parameter that comes to mind is the repetition frequency, as the fluid dynamic study of jets disturbed with artificial perturbations revealed a crucial role in jet stability.[103,121] The Strouhal number is a non-dimensional parameter linking; a characteristic frequency, which in the case of the APPJ is the repetition frequency. The momentum thickness of the shear layer of the jet assumed 1% of the diameter as it is a very low Reynolds number jet;[103] and the maximum velocity at the exit of the capillary U_m. The Strouhal number has a dominant excitation frequency for a value of 0.017[103,121]. A pulse-driven APPJ easily permits the change of the repetition frequency and the construction of a spectrum to identify the excitation frequencies. The polarity of the generated pulse affects the plasma

generation as well as the resulting chemistry. Observation of the plasma plume of a positive pulse-driven APPJ showed an increase in the length of the plasma plume for a pulse width of 1-3 µs and then decreases for longer pulse widths. The plasma plume length increases for a negative pulse for pulse widths up to 120-124 µs and decreases drastically for longer pulse widths.[23] Moreover, Uchida *et al.* observed a similar trend for a positive pulse-driven APPJ. The plasma plume length decreased from 60 to 47 mm when excited using pulses with pulse width between 40 and 160 µs (20-80% Duty cycle).[176] Moreover, the pulse width choice was expected to affect the plasma-induced turbulence.

In this chapter, the investigation of the influence of polarity, pulse width, and repetition frequency on the APPJ expanding in ambient air is conducted. The ability to control the electrical parameters of the exciting pulse to exert a level of influence over the turbulence generation and air entrainment in an APPJ was demonstrated. Firstly, the observations made on the impact of the repetition frequency on the intensity of the plasma-induced turbulence in the jet were examined. Then the influence of pulse polarity and the pulse width over the developing plasma plume in ambient air was observed, and the measurements of the velocity flow field. The input parameters revealed a discrepancy between the fluid dynamic and the observable plasma plume, demonstrating a link between the reduction of the plasma plume and the plasma-induced turbulence. The addition of a target in front of the expanding APPJ situated the study results in more realistic use. The APPJ fluid dynamic structure optimisation is paramount to control the chemistry in the plasma region and downstream.

6.2 Experimental methodology

The plasma jet used in this study was already described in Chapter 3 The power source applies a rectangular voltage pulse to the pin electrode with an average input power of 35 W (6.8 kV peak, 5.4 mA on average).

In the first section, the impact of the repetition frequency, the variation of the repetition frequency required compensation on the applied voltage to keep an average input power of 35 W, and the applied voltage varied between 6.3 and 6.7 kV while the current varied between 5.3-5.5 mA. The helium input flow rate was 3.7 SLM (Re = 218, U_m = 17.6 m.s^{-1}). The pulse width was 32 µs.

In the rest of the chapter, the flow rate was chosen closer to the experiments of the previous chapters. The repetition frequency was 8 kHz, the helium input flow rate was 3 SLM (Re = 177, U_m = 14.1 m.s^{-1}).

The PIV measurements to quantify the flow field disturbed by the plasma discharge were undertaken using the experimental setup described in section 3.4. Δt was set to 30 µs, the spatial dimensions of the grid were 350 µm^2. Each dataset comprised of 800 frames, 400 vector maps were averaged and presented as a single figure.

A TB4 hardboard, described as a 4.76 mm thick plastic-coated cardboard panel with a foam core, was used as a target downstream of the jet at a distance of 60 mm from the jet exit.

6.3 Impact of the repetition frequency

As shown in earlier chapters, an APPJ driven by an AC voltage dramatically reduces the laminar region length.[51] The commonly cited parameters affecting the generation of

turbulence in an APPJ are gas heating and electro-hydrodynamic forces that induce a velocity increase. The impact of the excitation frequency on these phenomena is still an area under investigation. Considering the initial parameters of our APPJ configuration and the empirical Strouhal number value for which the dominant excitation frequency can be deduced. The velocity at the exit of the tube was U_m = 17.6 m.s^{-1} and the repetition frequency f_0 = 10.00 kHz.[35,121]

To verify the influence of the dominant excitation frequency, the velocity field of the jet was measured for repetition frequencies in the range of 9-11 kHz, under constant power conditions. This was achieved by reducing the applied voltage as repetition frequency was increased to ensure a constant dissipated power of 35 W. For each frequency, the ensemble-averaged centreline velocity decay along the jet is extracted to observe the transition into a turbulent state.

Figure 53 shows the ensemble-averaged normalised centreline velocity decay for a pulse-driven APPJ with an input of 35 W for several frequencies in the range of 9 to 11 kHz. From the figure, it is clear to see that the laminar region is similar for all the cases. Moreover, the 10 kHz case shows the earliest onset of turbulence, occurring at a position of 17 x/D. Using the data presented in Figure 53, the laminar-to-turbulent transition point has been plotted. Figure 54 shows a spectrum of the transition-to-turbulence, which are the consequences of plasma-induced turbulence. This spectrum reveals the influence of the repetition frequency on the stability of the APPJ in the range chosen. The dominant excitation repetition frequency identified in this study is at the predicted 10 kHz, considering that the measurements were done with a step of 333 Hz. However, the 10 kHz case has a laminar region 4 mm (1.3D) shorter than the closest cases 9.67 and 10.33 kHz. The difference in length becomes more important (7 mm or 2.3D) with the cases 9.33 and 11 kHz; this difference represents more than 10% of

the laminar region length. Thus, the effect of the plasma-induced turbulence on the transition-to-turbulence of the APPJ depends on the repetition frequency, and it supports the hypothesis that plasma generation acts as an artificial perturbator in the developing jet.

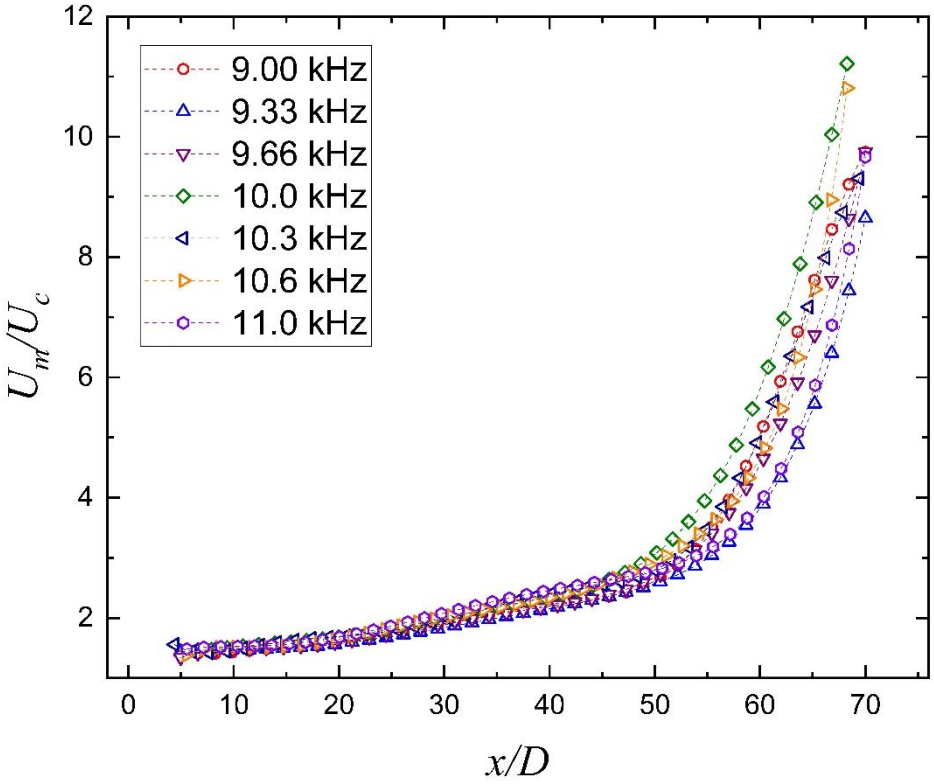

Figure 53: Ensemble-averaged normalised centreline velocity decay for a pulse-driven APPJ with an input power of 35 W and a range of repetition frequency (9-11 kHz). The flow rate is 3 LPM.

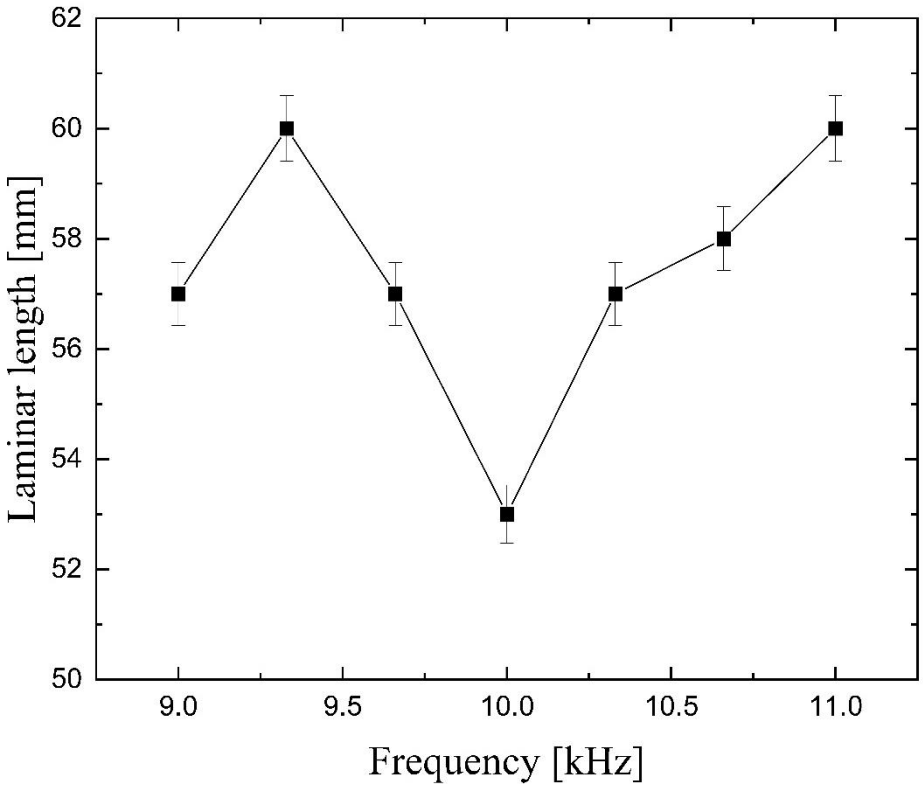

Figure 54: Measured laminar region length of an APPJ against the repetition frequency.

6.4 Impact of the polarity and pulse width

After identifying the influence of the repetition frequency on the APPJ by affecting the production of turbulence and reducing the laminar region, the effect of the pulse width and the polarity were examined. Figure 55 shows the plasma plume generated with the pulse-driven APPJ for positive (a) and negative (b) pulses for a range of pulse widths spanning 0.5 - 96 µs at a fixed repetition rate of 8 kHz (i.e., duty cycles ranging from 0.4 to 76.8%). The length of the plasma plume for positive pulses increased until a pulse width of 2 µs was reached, then slowly decreased in length, following similar trends reported in the literature.[23,176,177] In the negative pulse case, the plasma plume increased in length over the entire range of pulse widths, similar to the results reported in the recent literature.[23] The difference in the visible plasma plume between the two polarities can be explained by the faster propagation speed of the plasma bullet due to a stronger localised electric field and a higher ionisation rate in the positive

case.[84,178] Firstly, in the positive pulse-driven APPJ, the very short pulse width of 0.5 µs did not fully develop the plasma plume. Secondly, at a longer pulse width, the increased intensity of the applied electric field enables the development of the plasma plume, increasing its length. The decreasing trend of the plasma plume for longer pulse widths is independent of the electric field.[97] However, the reduction of the helium proportion along the plasma jet works against the local electric field sustaining the propagation of the plasma bullets due to air, which requires a higher electric field to sustain the plasma bullet.[179] Thus, the hypothesis is that the increasing pulse width induces turbulence and the reduction of the helium mole fraction, consequently limiting the length of the plasma plume. In the negative pulse-driven APPJ, at small pulse width, the short duration of the electric field did not allow the plasma plume to develop fully. The development was smaller than the positive pulse counterpart. At longer pulse widths, the increase in the length of the plasma plume is explained by the increased duration of the applied electric field, allowing the plasma bullet to propagate further.

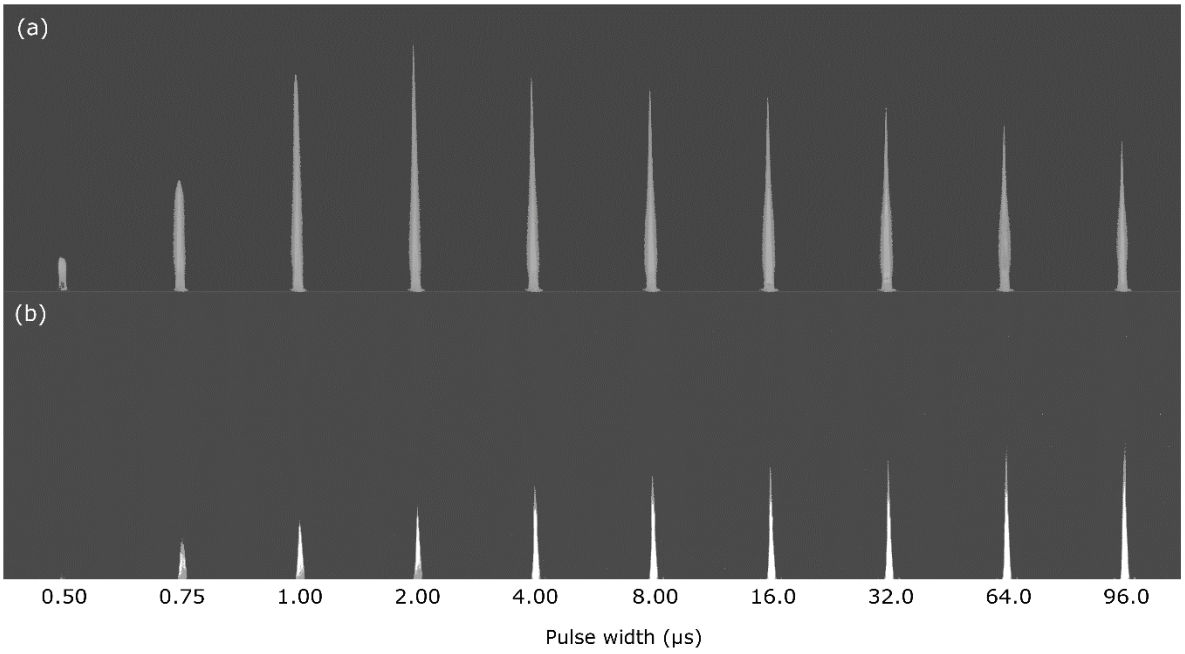

Figure 55: Picture of (a) positive and (b) negative pulsed-driven APPJ plasma plume for various pulse widths.

To understand the impact of pulse width on the length of the plasma plume, as shown in Figure 56, the flow rate of the APPJ was set to 3 LPM, corresponding to a jet exit velocity of U_m = 14.1 m.s^{-1}. A pulse repetition frequency of 8 kHz was chosen in line with the predicted dominant excitation frequency from the Strouhal number equation. It also helped increase the turbulence in the APPJ and obtained earlier transition-to-turbulence within the camera's field of view. The pulse width range explored was limited to a maximum of 125 µs to avoid damages to the power source. The pulse widths values chosen were 0.5, 1, 2, 4, 8, 16, 32, 64, 96 µs corresponding to 0.4, 0.8, 1.6, 3.2, 6.4, 12.8, 25.6, 51.2 and 76.8 % duty cycle, respectively. From Figure 57, in the case of a positive pulse-driven APPJ, the earlier transition-to-turbulence of the longest pulse widths 64 and 96 µs, and the 32 µs case, which has a slower decrease, is apparent. The other cases followed the same trend as the case without plasma. For the negative pulse-driven APPJ, the 96 µs case was distinguished with an early transition-to-turbulence at 46 mm, although the 64 and 32 µs cases show a transition at 70 mm.

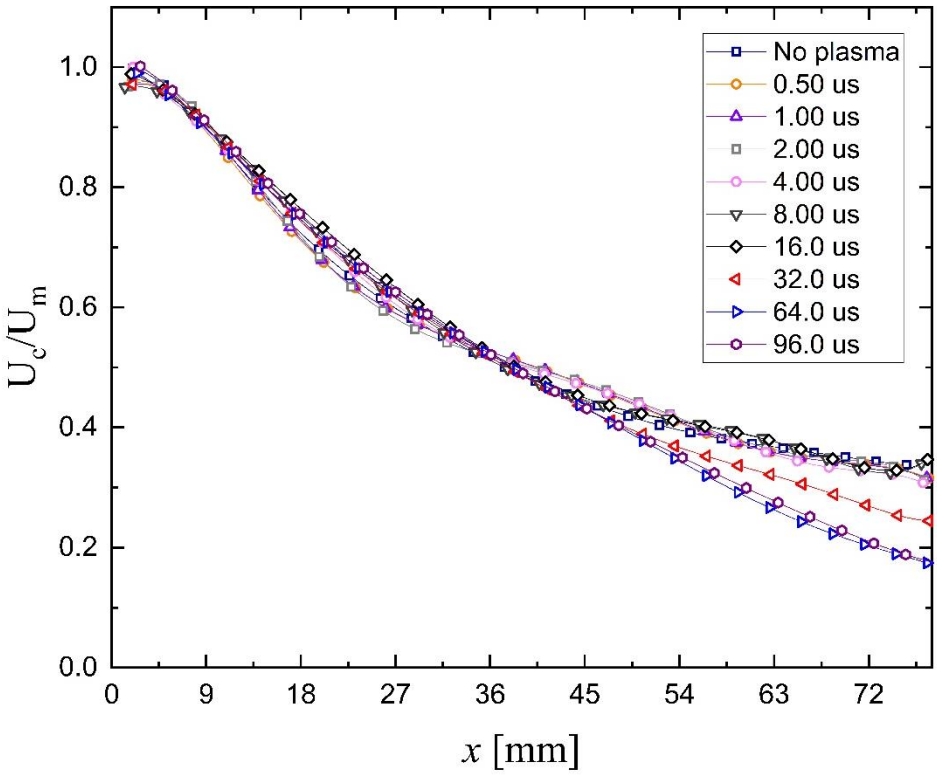

Figure 56: Ensemble-averaged normalised centreline velocity decay for a positive pulse driven APPJ with an input power of 35 W, a repetition frequency of 8 kHz, for pulse width in the range of 0.50 to 96 µs. The flow rate is 3 LPM.

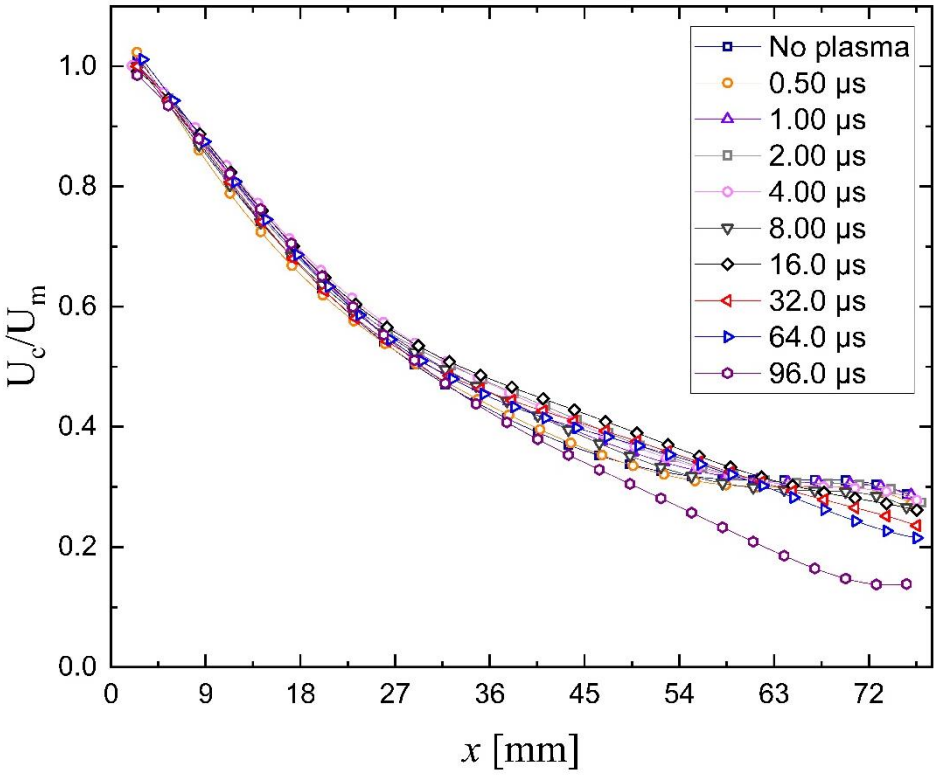

Figure 57: Ensemble-averaged normalised centreline velocity decay for a negative pulse-driven APPJ with an input power of 35 W, a repetition frequency of 8 kHz, for pulse width in the range of 0.50 to 96 µs. The flow rate is 3 LPM.

Figure 58 shows the length of the visible plasma plume measured against the pulse width. A peak is observed at 65 mm for the positive case at a pulse width of 2 µs, followed by a linear decrease of the plasma plume length for longer pulse widths, as shown in Figure 55. The negative case shows a logarithmic increase, reaching near its maximum plasma plume length at 8-16 µs. Despite the observed difference in plasma plume length between the polarities, the trend of the laminar region length is similar. For both polarities, the transition-to-turbulence was identified for pulse widths longer than 32 µs. In the positive-pulse case, the reduction of the laminar region length has a similar pattern as the reduction of the plasma plume length, showing that the visible plasma plume length is affected by the increased plasma-induced turbulence. The consequential air entrainment and gas mixing oppose the propagation of the plasma bullet by decreasing the helium mole fraction along the APPJ.

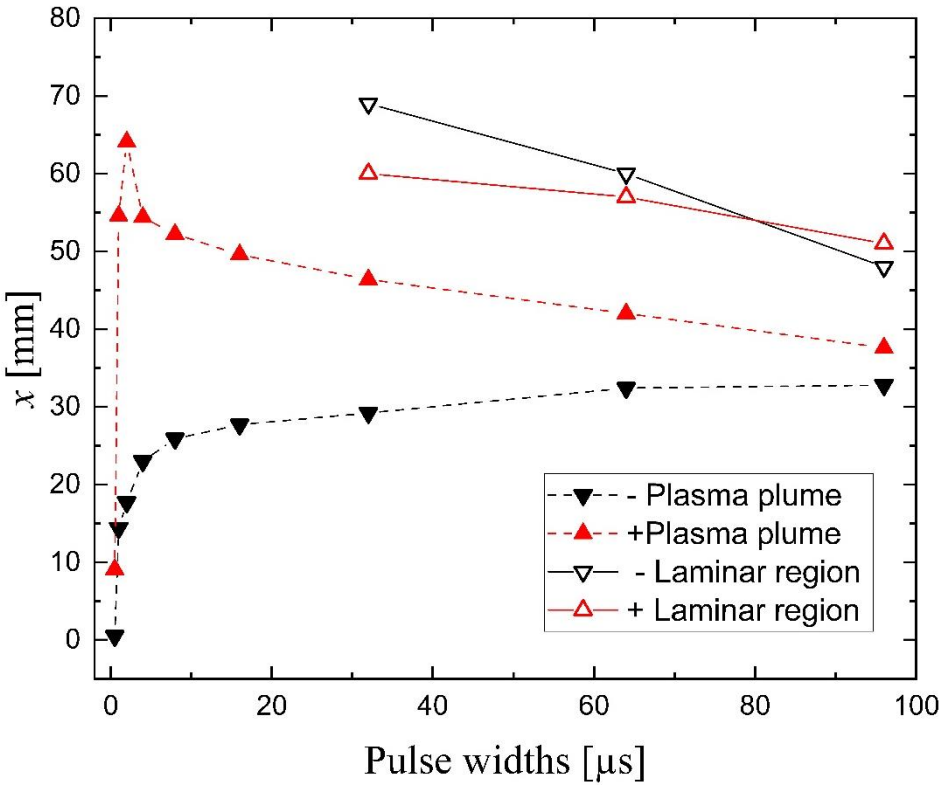

Figure 58: Length of the pulse-driven plasma plume generated with positive (red full triangle) and negative (black full triangle) polarities, length of the laminar region of the jet for positive (red empty triangle) and negative (black empty triangle).

The observation of the APPJ under both polarities and a wide range of pulse widths provide insight into the influence of the electrical parameters on the APPJ fluid dynamic structure. The negative pulse-driven showed that the visible plasma plume was constrained in its development by the short pulses. However, the longer pulse widths provided more time for the plasma bullet to propagate.[178] The positive pulse-driven showed the plasma plume was limited in its development by short pulses, where the plasma did not have enough time to propagate. At longer pulse widths, there was a decrease in the length of the plasma plume, assumed to be independent of the electric field.[97] Moreover, the measure of the velocity flow field and the transition-to-turbulence point showed that for longer pulse widths, the reduction of the laminar region revealed the increase of turbulence in the APPJ. The link between the reduction of the laminar region and the generation of turbulence was shown in Chapter 4. Besides, the plasma-induced turbulence provokes air entrainment, as shown in Chapter 5. Thus,

reducing the helium mole fraction in the APPJ works against the propagation of the plasma bullet in ambient air, provoking a reduction of visible plasma plume length. Figure 58 shows a similar trend of the decreasing laminar region and visible plasma plume.

6.5 The impact of a target

The study of a free APPJ expands into resting ambient air and provides valuable insights into the plasma-induced turbulence and its consequences. Although it is not a suitable configuration for classic applications, it typically involves a plasma jet impinging on a surface. The final part of this thesis considered the impact of a flat target positioned downstream of the APPJ propagation axis. An APPJ which expands upwards into the ambient air and impinges on a target above the jet was considered to maintain relevance with the previously reported results.

Figure 59 shows PIV pictures of the APPJ expanding in ambient air and impinging on a horizontal target positioned at 60 mm from the exit of the capillary. In Figure 59 (a), the absence of the plasma discharge allows the jet to develop in the quiescent air in a laminar structure, and a thin layer of seeded helium travelled across the target radially. In the negative pulse-driven APPJ case with a flow rate of 3 LPM, an input power of 35 W, a repetition frequency of 8 kHz, a pulse width of 96 µs (Figure 59 (b)), and instabilities on the edges of the

jet were observed, followed by the generation of large scale eddies and a strong alteration of the core of the jet. Moreover, the large-scale eddies moved on the surface of the target.

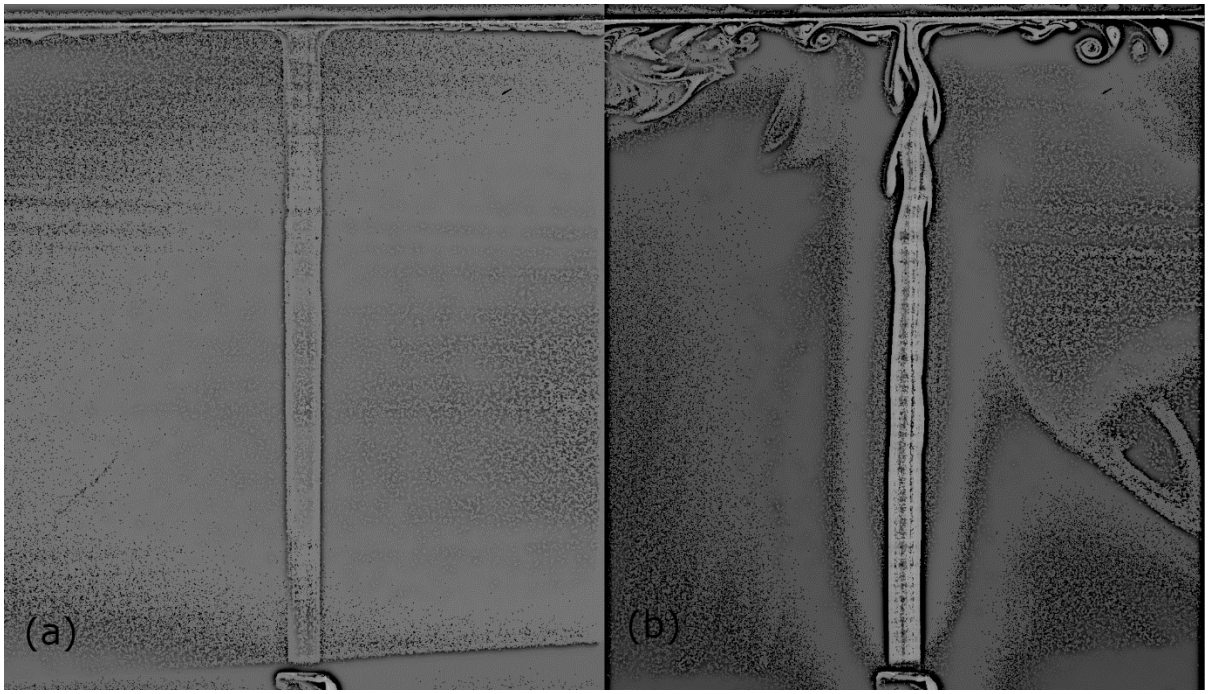

Figure 59: Picture from PIV measurements of the negative pulse-driven APPJ (a) without plasma and (b) with plasma impinging onto a horizontal target situated 60 mm from the capillary.

Furthermore, the measure of the velocity flow field of the APPJ expanding in ambient air with and without a target was conducted. The ensemble-averaged velocity contour obtained from the PIV measurements is shown in Figure 60. The negative pulse-driven APPJ, (a) without plasma, with plasma and pulse widths of (b) 32 µs, (c) 64 µs, and 96 µs (d). The APPJ aimed at a target (e) without plasma, with plasma and pulse widths of (f) 32 µs, (g) 64 µs, and 96 µs (h). These pulse widths were chosen because they showed a clear transition into a turbulent state under excitation of both positive and negative polarities without the presence of a target. Figure 60 (a) and (e) show that without the plasma generation and following precedent results, the flow is unperturbed in the field of view considered with and without the target. The velocity of the flow circulating on the target's surface was small compared to the jet velocity. The plasma cases with pulse widths of 32, 64, and 96 µs showed a similar trend as observed in chapters 4 and 5, where the applied voltage was increased. The increase in the pulse width length reduced the laminar region for 32 µs, more for 64 µs, and a significant reduction for 96 µs. An increase of the perturbations generated in the APPJ was thus observed. When the APPJ impinged on a target, the flow structure was not altered. The 32 µs did not transition into a turbulent state, as its transition-to-turbulence point was situated at a further position than the target. The 64 µs case showed signs of turbulence transition; however, the transition started near the target. The 96 µs transitioned into a turbulent state, as expected from the case without a target.

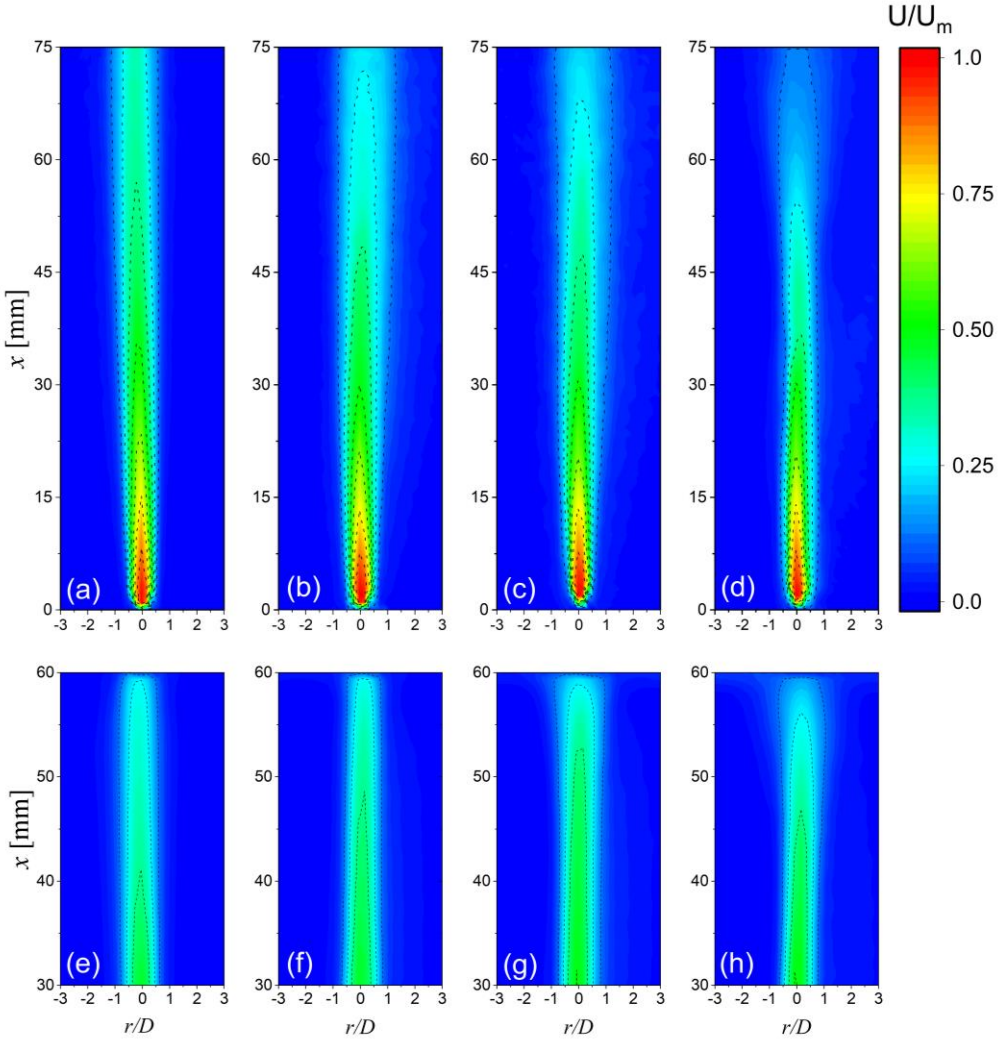

Figure 60: Ensemble-averaged velocity profile for a helium jet (a), a negative-pulse driven APPJ with a flow rate of 3 SLM, an input power of 35 W, a repetition frequency of 8 kHz, for pulse widths of 32 µs (b), 64 µs (c), and 96 µs (d). The second part is a zoomed-in version of the jet directed toward a target situated at 60 mm from the jet exit, for a helium jet (e) and pulse driven APPJ at the pulse widths of 32 µs (f), 64 µs (g), and 96 µs (h).

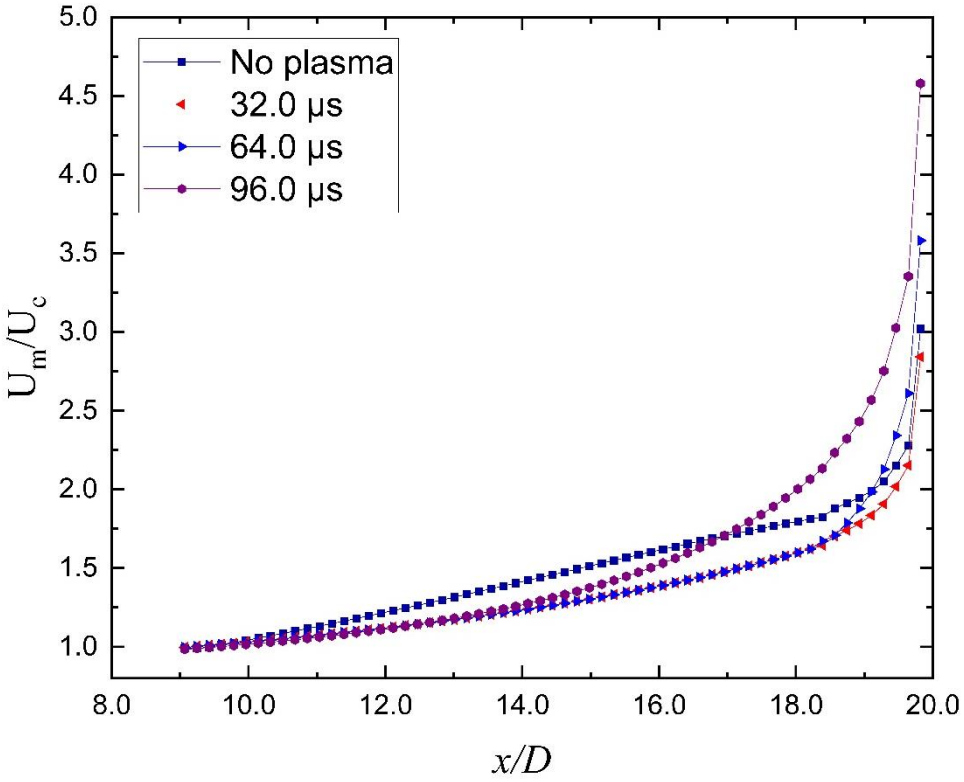

Figure 61: Streamwise normalised centreline velocity profiles Um/Uc for a pulse-driven APPJ with an input power of 35 W, a repetition frequency of 8 kHz, for pulse widths of 32 µs, 64 µs, and 96 µs. The flow rate is 3 LPM, and the jet is directed toward a target situated at 60 mm from the capillary exit.

The normalised centreline velocity decay U_m/U_c along the APPJ extracted from the ensemble-averaged velocity contour and shown in Figure 61. As expected from the no-target measurements, the longest pulse width, 96 µs, shows velocity decay significantly faster due to its earlier transition-to-turbulence. The no-plasma and the 32 µs pulse width were both laminar along the entire field of view. This is not surprising since the transition-to-turbulence without the target did not occur without a plasma discharge and occurred at 69 mm with a pulse width of 32 µs. Moreover, they share a similar drop of velocity due to the presence of a target. For the 64 µs pulse width case, the drop in velocity occurs at 18 x/D provoked by the transition into a turbulent state, in agreement with the observed transition without a target which occurred

at 60 mm. The 96 µs transitioned into a turbulent state at 15 x/D, similar to the 64 µs case, near the target; the decreasing velocity declined significantly.

6.6 Conclusion

This chapter explored the influence of the electrical parameters of a pulse-driven APPJ expanding in ambient air in both a free jet configuration and in the presence of a downstream target. The measurements of the transition-to-turbulence provided insight into the impact of the dominant excitation frequency on the structure of the APPJ. This result highlights the importance of the repetition frequency and the related Strouhal number.[35,121] Exciting the APPJ at the predicted dominant frequency showed a reduction of the laminar region and increased the plasma-induced turbulence in the APPJ. The effect of the repetition frequency on the generation and propagation of disturbances along the flow field was assessed, although it is linked to flow structure dynamics rather than the plasma itself; thus, results were observed in various configurations.

The positive polarity input voltage generates a longer plasma plume in comparison to the negative polarity. The increase induced by longer pulse width was expected due to the electric field's crucial part in propagating the plasma bullet. The limited on-time for very short pulse width cases did not allow a fully developed plume to be created under both polarities excitation. The visible plasma plume decreased at longer pulse widths. The origin of the reduction of the positive-pulse plasma plume visible length was caused by the reduction of helium mole fraction from air entrainment and mixing. The reduction of helium mole fraction in a plasma jet is extremely sensitive, as shown in Chapter 5 with Rayleigh scattering measurements. The laminar region length has a similar linear decrease to the pulse width. The plasma-induced turbulence is shown to increase with the pulse width; thus, the air entrainment and gas mixing

are expected to increase. The presence of entrainment reduces the helium mole fraction significantly, which negatively affects the propagation of the plasma bullet. Consequently, the visible plasma plume is reduced.

Although the results obtained for several pulse widths provide an encouraging indication that manipulation of the electrical parameters may provide a means to influence the chemistry of an APPJ. The lack of a target means that the results are less applicable to the range of applications to which such systems are currently being applied. Since the presence of an obstacle changes the fluid dynamics of the jet, it would thus affect the chemistry. This work showed that the addition of a target did not significantly alter the transition-to-turbulence of the cases chosen. Furthermore, the measured laminar length at the longest pulse width (96 µs) was in close agreement in both cases, with and without a target. These observations show that although the target presence and position are expected to be crucial, they did not drastically alter the fluid dynamics in the jet part.

Nowadays, the control over the laminar region of an APPJ is done by varying either the flow rate or the input power, the impact of which was explored in Chapter 4. A more convenient and efficient way of controlling the chemistry downstream of the APPJ is to optimize the electrical parameters of the exciting voltage pulse. Critically, in applications where the mixing of air is unwanted, the use of very short pulses should be considered to minimise entrainment. Furthermore, a repetition frequency different from the predicted dominant excitation frequency should be selected. In applications where mixing with the environment is crucial to obtain a high density of RONS, longer pulse widths and an appropriate selection of the repetition frequency are recommended. This latter case would be particularly attractive for use in biomedical decontamination applications where high densities of RONS are known to be the key drivers in microbial inactivation.[29,180–183]

Chapter 7 Conclusions and future outlook

7.1 Conclusion

The hypothesis was that the plasma discharge induced turbulence in the plasma jet and disturbed the jet structure, consequently affecting the fluid dynamics, plasma physics, and plasma chemistry. In this study, the first quantitative velocity measurements of a plasma jet helped in examining the velocity field and the calculation of the turbulence. The perturbations were shown to be generated at the exit of the capillary in the shear layer. They propagated along the jet edges while increasing in intensity. These perturbations are believed to be caused by gas heating and EHD. The impact of the input flow rate and the applied voltage in sine wave plasma jet were assessed, resulting in more important turbulence with an increasing applied voltage and a longer laminar region with higher flow rates.

Furthermore, these perturbations caused instability in the jet structure and the presence of increasing air entrainment ineluctable. Rayleigh scattering measurements showed that the reduction of the helium density along the jet was linked to increasing air entrainment favoured by a higher applied voltage. The measurement of the OH density along the plasma plume with Laser-induced fluorescence revealed that the OH mostly generated from impurities present in the helium, was more important for a higher applied voltage due to enhanced H_2O entrainment. It decreased at a position closer to the jet exit due to an increase presence of air entrainment quenching OH.

Finally, using a pulse input on the same plasma jet configuration allowed more finesse to the input electrical parameters. The repetition frequency in relation to the Strouhal number confirmed a dominant excitation frequency, resulting in enhanced turbulence production and, thus shorter laminar region. The polarity and the pulse width were also studied; quantitative

measurements that confirm the previous qualitative observations in the literature were provided for the first time. The effect of the polarity and the pulse width on the visible plasma plume was assessed; short pulse widths limit the length of the visible plasma plume. The positive pulse-driven APPJ had a decreasing visible plasma plume for longer pulse widths. This observation resulted from the plasma-induced turbulence in the APPJ studied in Chapter 4 and the sensitivity of the helium mole fraction from air entrainment and gas mixing studied in Chapter 5. Finally, the addition of a target downstream of the propagating APPJ did not alter the transition-to-turbulence point under the conditions considered.

The electrical parameters showed a convenient and efficient way of controlling the APPJ flow structure. Depending on the settings, the APPJ can favour air entrainment and gas mixing through very turbulent prone settings, such as a well-chosen repetition frequency, a long pulse width, low flow rate, and a high applied voltage. The turbulence generation would be enhanced; thus, the chemical interaction with the background gas can be achieved. On the other hand, by choosing opposite parameters, the laminar behaviour of the flow can be optimised to avoid the chemical interactions with the background to conserve a high helium mole fraction successfully.

7.2 Future outlook

APPJs are an excellent choice for microbial decontamination and wound healing applications. However, there are several key challenges. Perhaps the most pressing concern is the variability in RONS generation due to changes in environmental or sample conditions; any successful healthcare technology must be predictable and repeatable. Hence future efforts should be directed towards implementing strategies for the continuous monitoring and control of RONS generation. The results from this study are a step forward in controlling the dynamic

structure of fluids, which is essential for controlling chemistry; more experiments are required to optimise application-specific configurations.

While the application of sophisticated diagnostic techniques, such as laser-induced fluorescence, is unrealistic for *in-situ* monitoring. The application of optical emission or absorption spectroscopy is a realistic prospect to indicate RONS production and the day-to-day repeatability of the process. Such efforts could be further improved by comparing diagnostic data against those predicted from computational models. While monitoring the composition of RONS, reaching the target is a vital first step to ensure repeatability; acting on the data captured to dynamically alter the plasma generating conditions to manipulate the production of RONS perhaps remains perhaps the greatest challenge. To overcome this challenge, feedback from the sensor to the power source will be essential. Yet, beyond simply varying the applied voltage or frequency, it is not clear how the actual composition of RONS in the plasma could be varied to negate changes in the external environment. Recent efforts in Machine Learning have proven fruitful in safety-critical applications, where precise control of plasma parameters is a prerequisite;[184] paving the way for intelligent control of RONS generation.

Ultimately, it is clear that the use of APPJs in biomedical and healthcare applications holds enormous promise in areas of enormous clinical need. In particular, wound healing and dentistry would benefit from insights on optimisation of APPJ shown in this study. Besides, the popularisation of hair implant technology can be a new area of research for APPJ applications. The treatment of the skin and the follicle could prevent or treat infection and inflammation. There has been enormous progress in the research efforts on APPJ technology. Our growing knowledge and understanding of the underpinning mechanisms of the widespread adoption of APPJ technology in the clinic are becoming a real possibility.

Appendix A Supplementary information Chapter 4

A.1 Radial turbulence intensity of velocity fluctuations

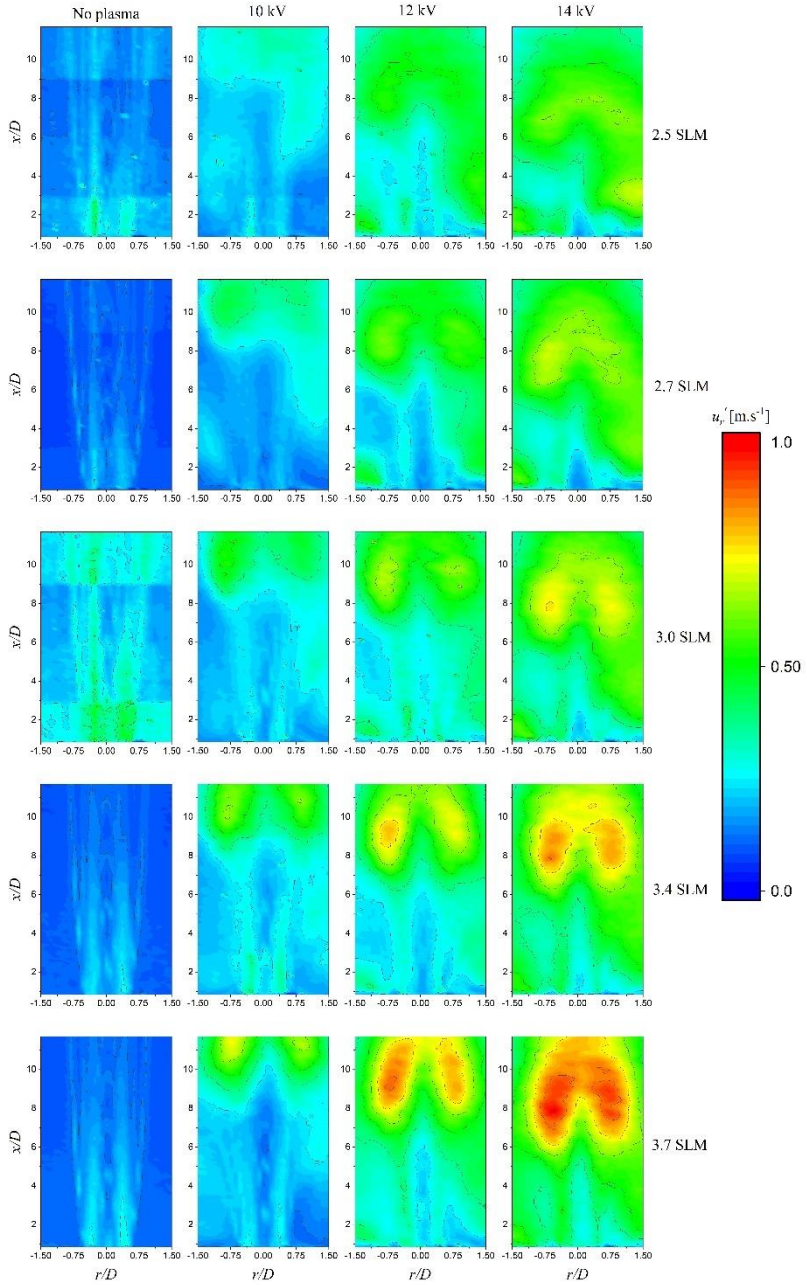

Figure A1: Radial turbulence intensity of velocity fluctuations contour for an APPJ without plasma, with an input voltage of 10, 12, and 14 kV at a flow rate of 2.5, 2.7, 3.0, 3.4, and 3.7 SLM.

A.2 Radial turbulence intensity of velocity fluctuations normalised by the centreline velocity

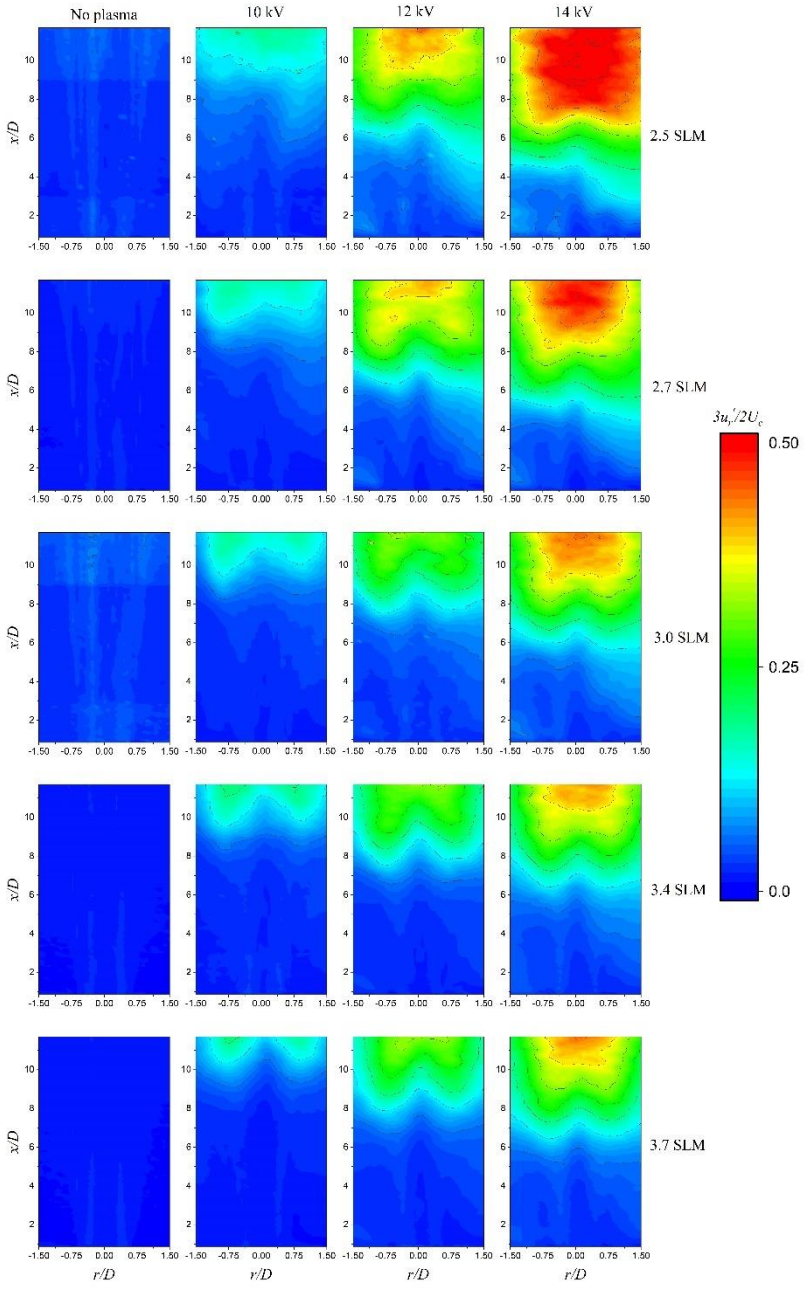

Figure A2: Radial turbulence intensity of velocity fluctuations contour normalised by the centreline velocity for an APPJ without plasma (first column), with an input voltage of (second column) 10, (third column) 12, and (fourth column) 14 kV at a flow rate of (first line) 2.5, (second line) 2.7, (third line) 3.0, (fourth line) 3.4, and (fifth line) 3.7 SLM.

A.3 Streamwise turbulence intensity of velocity fluctuations

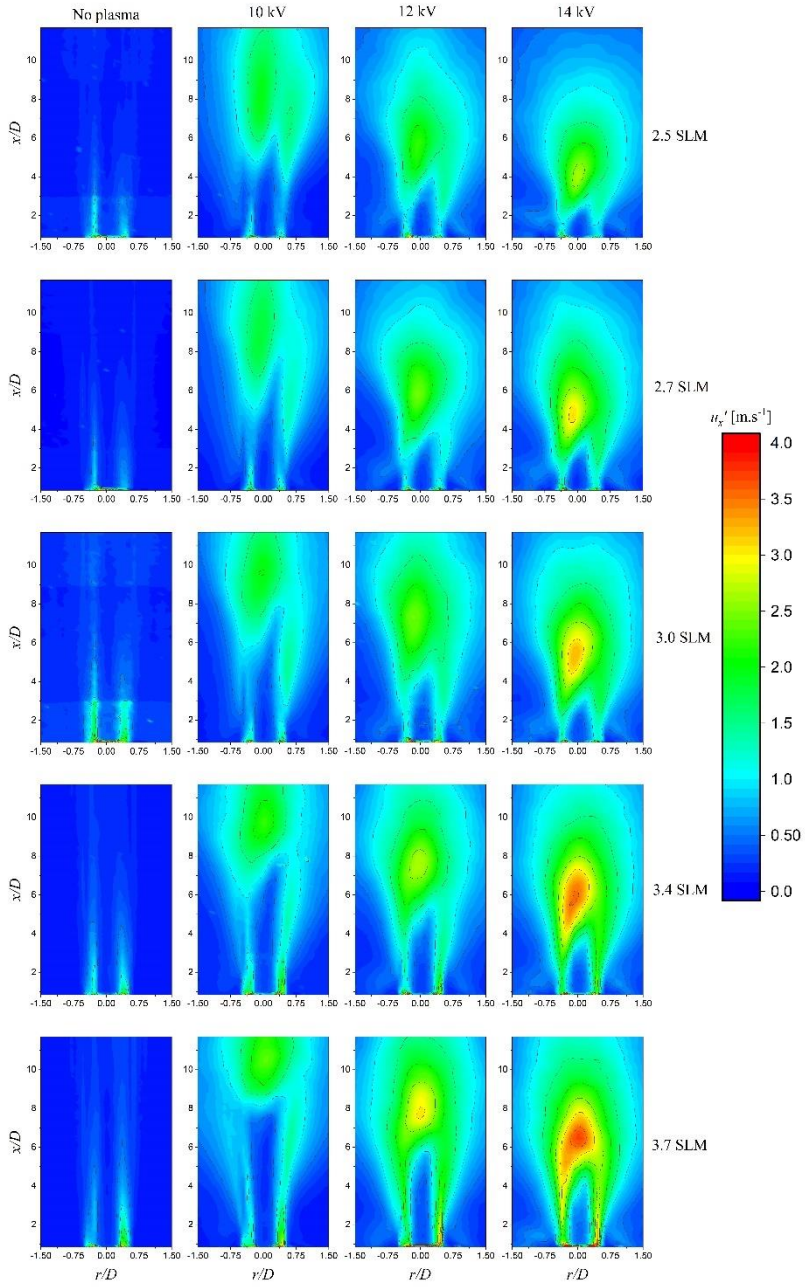

Figure A3: Streamwise turbulence intensity of velocity fluctuations contour for an APPJ without plasma (first column), with an input voltage of (second column) 10, (third column) 12, and (fourth column) 14 kV at a flow rate of (first line) 2.5, (second line) 2.7, (third line) 3.0, (fourth line) 3.4, and (fifth line) 3.7 SLM.

A.4 Streamwise turbulence intensity of velocity fluctuations normalised by the centreline velocity

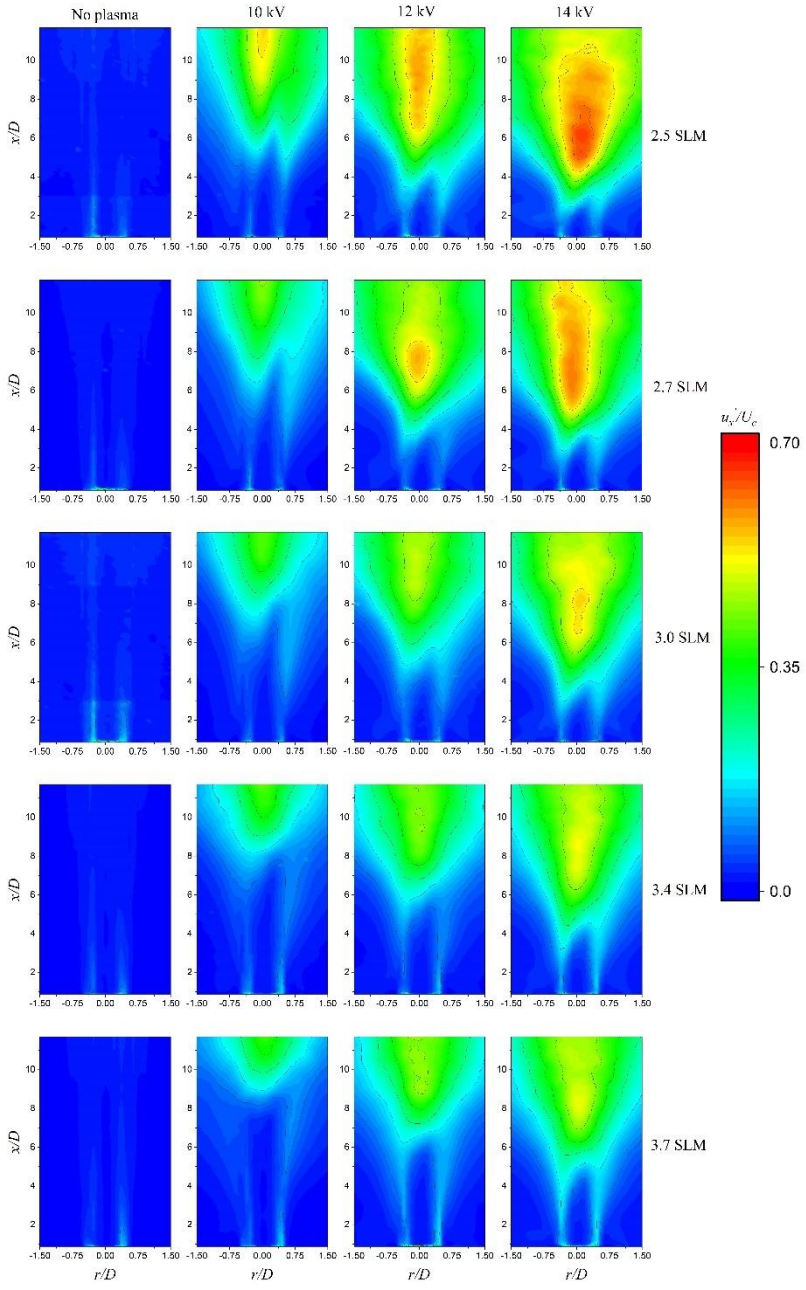

Figure A4: Streamwise turbulence intensity of velocity fluctuations contour normalised by the centreline velocity for an APPJ without plasma (first column), with an input voltage of (second column) 10, (third column) 12, and (fourth column) 14 kV at a flow rate of (first line) 2.5, (second line) 2.7, (third line) 3.0, (fourth line) 3.4, and (fifth line) 3.7 SLM.

A.5 Turbulent kinetic energy

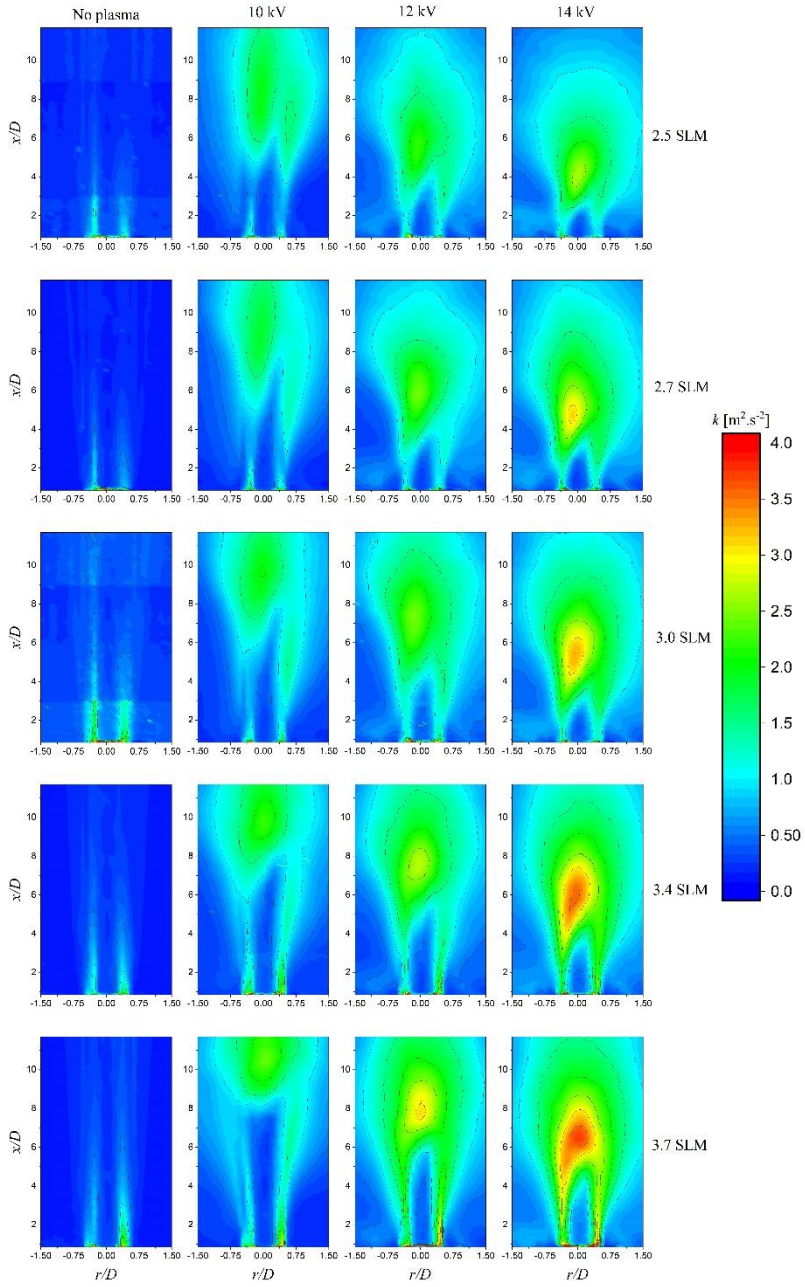

Figure A5; Turbulent kinetic energy contour for an APPJ without plasma (first column), with an input voltage of (second column) 10, (third column) 12, and (fourth column) 14 kV at a flow rate of (first line) 2.5, (second line) 2.7, (third line) 3.0, (fourth line) 3.4, and (fifth line) 3.7 SLM.

A.6 Turbulent kinetic energy normalised by centreline velocity

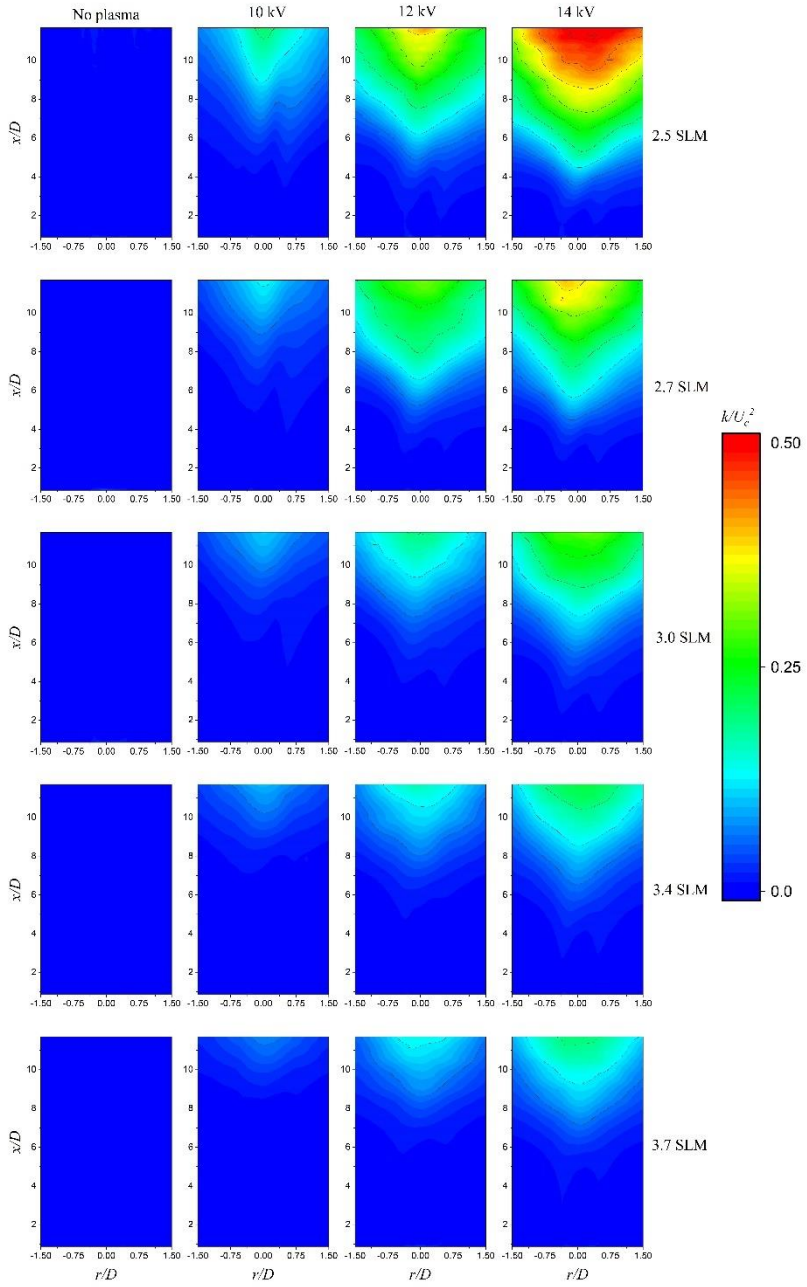

Figure A6: Turbulent kinetic energy contour normalised by the centreline velocity for an APPJ without plasma (first column), with an input voltage of (second column) 10, (third column) 12, and (fourth column) 14 kV at a flow rate of (first line) 2.5, (second line) 2.7, (third line) 3.0, (fourth line) 3.4, and (fifth line) 3.7 SLM.

A.7 Reynolds stress

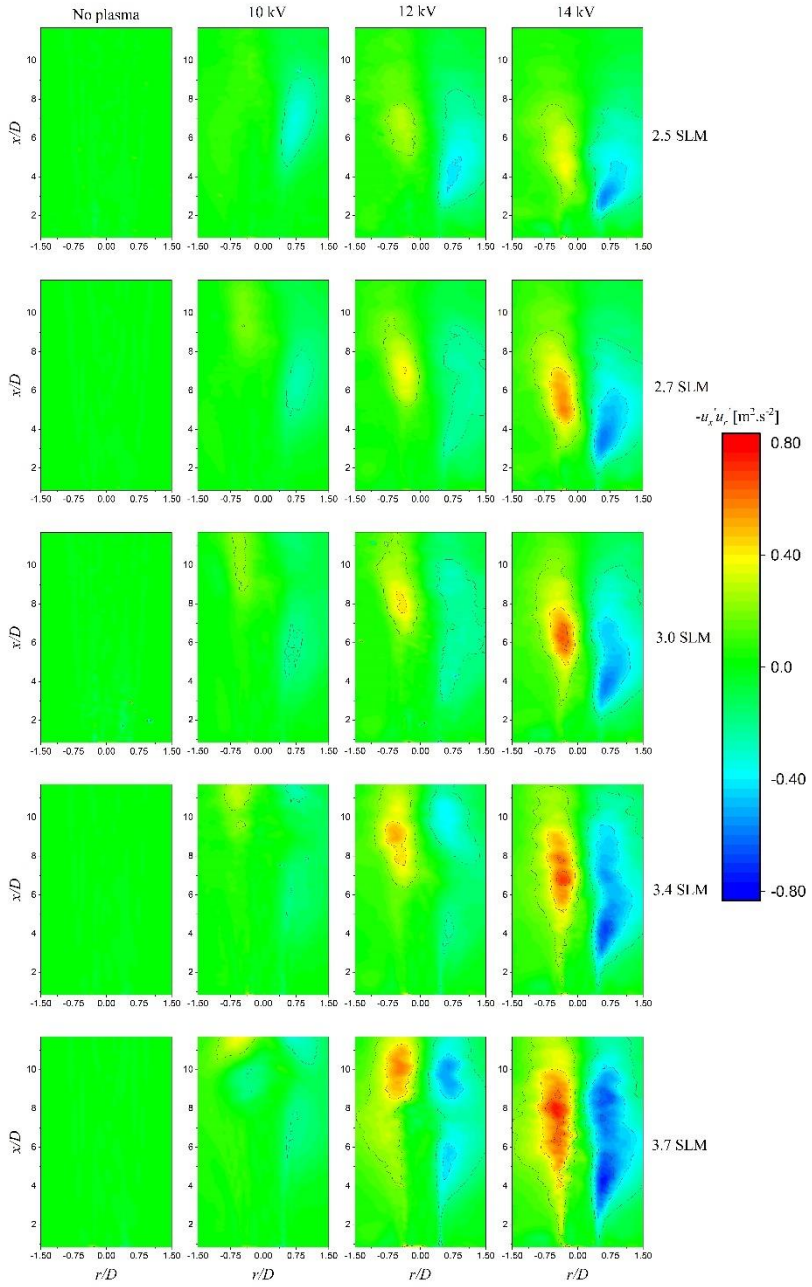

Figure A7: Reynolds stress contour for an APPJ without plasma (first column), with an input voltage of (second column) 10, (third column) 12 and (fourth column) 14 kV at a flow rate of (first line) 2.5, (second line) 2.7, (third line) 3.0, (fourth line) 3.4, and (fifth line) 3.7 SLM.

A.8 Reynolds stress normalised by the centreline velocity

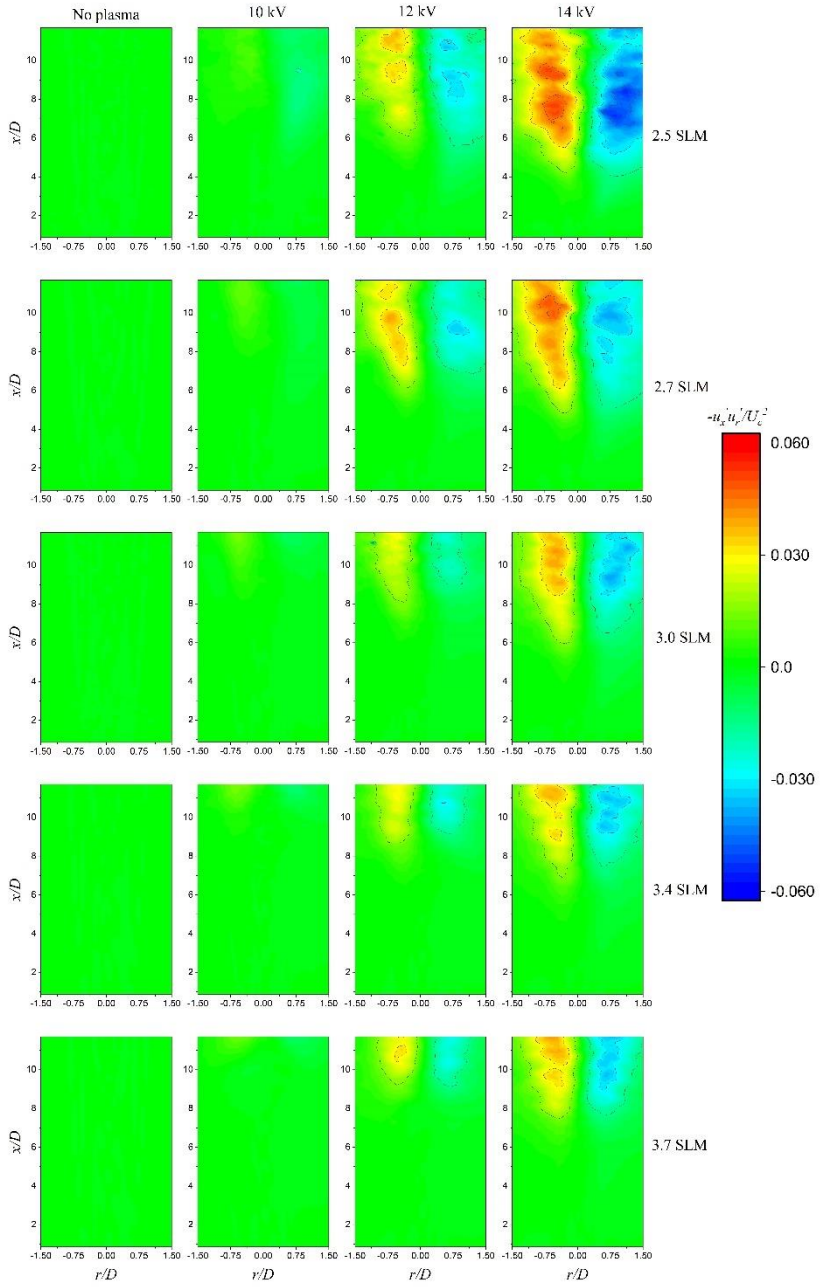

Figure A8: Reynolds stress contour normalised by centreline velocity for an APPJ without plasma (first column), with an input voltage of (second column) 10, (third column) 12, and (fourth column) 14 kV at a flow rate of (first line) 2.5, (second line) 2.7, (third line) 3.0, (fourth line) 3.4, and (fifth line) 3.7 SLM.

Appendix B Models

From *Plasma Process Polym.,* Manuscript number DOI:10.1002/ppap.

B.1 Gas mixture

In order to account for the varying composition of gas downstream of the jet orifice, a computational model was developed that solved for the velocity field of the gas mixture in addition to the mass fractions of its constituents, namely N_2, O_2, H_2O, and He. To obtain the velocity field, the model solved the mass continuity Equation (B.1), which solves for the mass density of the entire gas mixture, and the momentum conservation Equation (B.2). To compute densities of the species constituting the gas mixture, the mass continuity equation, given by Equation (B.3), was solved for the mass fraction of three species, while the mass fraction of the fourth was determined from the pressure constraint. All equations were solved in steady-state mode (*i.e.*, time-independent equations):

$$\nabla \cdot (\rho \vec{u}) = 0 \tag{B.1}$$

$$\rho(\vec{u} \cdot \nabla)\vec{u} = -\nabla \mathrm{P} + \nabla \cdot \left(\mu(\nabla \vec{u} + \nabla \vec{u}^T) - \frac{2}{3}\mu(\nabla \cdot \vec{u})I\right) - (\rho - \rho_0)g \tag{B.2}$$

$$\rho(\vec{u} \cdot \nabla)\omega_i + \nabla \cdot \left(\vec{\Gamma}_i\right) = 0 \tag{B.3}$$

Where ρ is the density of the gas mixture (kg m^{-3}), $\vec{u}$ is the velocity field of the gas mixture (m s^{-1}), P is the gas mixture's pressure (Pa), μ is the gas mixture's viscosity (Pa s), I is the identity matrix, ρ_0 is the density of air (kg m^{-3}), and g is the gravitational acceleration (m s^{-2}), ω_i is the mass fraction of the i^{th} species, and Γ_i is the diffusive flux of the i^{th} species, which is calculated according to Maxwell-Stefan theory for diffusion as given by Equation (B.4, B.5, B.6).[185,186]

$$\vec{\Gamma}_i = \rho \omega_i \vec{V}_i \tag{B.4}$$

$$\nabla x_i = \sum_{j=1}^{4} \frac{x_i x_j}{D_{ij}} \left(\vec{V}_j - \vec{V}_i \right) + \frac{\nabla p}{p} (\omega_i - x_i) \tag{B.5}$$

$$x_i = \frac{M_n}{M_i} \omega_i \tag{B.6}$$

Where $\vec{V}_i$ is the diffusion velocity of the i^{th} species (m s^{-1}), x_i is the mole fraction of the i^{th} species (dimensionless), which is related to the mass fraction by Equation (B.4), and D_{ij} is the binary diffusion coefficients between the i^{th} and the j^{th} species (m^2 s^{-1}). A list of the binary diffusion coefficients used in the model is given in Table B1. It should be noted that Equation (B.5) is incorporated in the model as a constraint linking the flux term and the mass fraction term in Equation (B.3). In Equation (B.6), M_i and M_n are the molecular weight of the i^{th} species and the average molecular weight, respectively (kg mol^{-1}). Lastly, the computational domain and the boundary conditions used are described in Appendix B2.

Table B1: A list of binary diffusion coefficients used in the model.

Combination	Diffusion coefficient [m^2 s^{-1}]	Reference
N_2 – He	6.78×10^{-5}	[187]
N_2 – O_2	2.09×10^{-5}	[188]
N_2 – H_2O	2.54×10^{-5}	[189]
O_2 – He	7.36×10^{-5}	[187]
He – H_2O	8.36×10^{-5}	[189]
O_2 – H_2O	3.185×10^{-5}	[189]

It is hypothesized that plasma-induced turbulence affects the flow's velocity field and thus the gas composition. In order to account for such effects in the computational model, the Reynolds-Averaged Navier-Stokes (RANS) approach for modelling turbulence was followed, where a turbulent viscosity μ_T (also known as eddy viscosity) was added to the viscosity of the gas mixture. The eddy viscosity is a mathematical means to describe the loss of momentum of the flow as a result of turbulence as an "effective" viscosity that is added to the physical viscosity of the fluid. Similarly, a turbulent diffusivity D_T is added to the binary diffusion coefficients.[190] The computation of the eddy viscosity is typically done using one of the conventional RANS turbulence models, such as the $k-\varepsilon$ model. The $k-\varepsilon$ model consists in a two-equation model describing the mean flow for turbulent conditions which fits well the objective here, although *k-omega* is an alternative to model turbulence. Considering that such models were calibrated for flows without plasma, their use for plasma modified flows will yield

results with unknown accuracy. To overcome this challenge, statistical analysis of the PIV data was conducted to obtain the necessary parameters to calculate the eddy viscosity resulting from the plasma generation. Following the $k-\varepsilon$ modelling approach, the turbulent kinetic energy k ($m^2\ s^{-2}$) and the turbulent kinetic energy dissipation rate ε ($m^2\ s^{-3}$) are defined by Equation (B.7) and (B.8).[190]

$$k = \frac{1}{2}\left(\overline{{u'_r}^2} + \overline{{u'_x}^2}\right) \tag{B.7}$$

$$\varepsilon = 2\nu_v \overline{s'_{ij} \cdot s'_{ij}} \tag{B.8}$$

In Equation (B.8), s'_{ij} is the fluctuating deformation rate of the fluid (s^{-1}), which was calculated from the PIV data as outlined by Xu and colleagues.[191] After calculating k and ε the eddy viscosity was calculated according to Equation (B.9).[190]

$$\mu_T = \rho C \frac{k^2}{\varepsilon} \tag{B.9}$$

Where C is a constant equal to 0.0016 and ρ is the self-consistent gas mixture density calculated by the model. The turbulent diffusivity D_T is related to the eddy viscosity by Equation (B.10).[190]

$$D_T = \frac{\mu_T}{\rho Sc_T} \tag{B.10}$$

Where Sc_T is the turbulent Schmidt number, obtaining an accurate value for this in a plasma-modified flow is not possible; however, the turbulent Schmidt number is close to unity for a wide variety of gas flows under very diverse conditions; hence it is assumed to be 1 in this investigation.[192] The model is subsequently solved with the experimental input of μ_T and D_T, which were smoothed and mirrored, then added to their physical counterpart quantities.

The model was solved for applied of 10 and 14 kV, in addition to an unperturbed laminar case, where the eddy viscosity and diffusivity were set to zero.

The model is a radiative collisional model which consisted of a system of Ordinary Differential Equations (ODE) describing the LIF transitions. The system was solved at every point in the computational domain close to the jet's orifice ($x < 20$ mm, $x/D < 7$), with the gas composition required for the ODEs being taken from that calculated by the fluid flow model. To quantify the density of ground-state OH, the 4-level model reported by Verreycken et al. was adopted.[160] The experimental parameters used in this study are summarised in Table 4. In order to validate the developed computational model, the predicted LIF signal decay times were compared to those measured experimentally at multiple points along the jet axis; a close agreement was observed.

B.2 Boundary conditions for the model

This appendix explains the geometry used in the model and the boundary conditions for the equations solved. The computational domain is shown in Figure B1 and the boundaries are labelled B1 to B5. For every equation solved, there is a boundary condition implemented on every boundary. A list of the implemented boundary conditions is listed in Table B2.

The boundary condition B1 describes the symmetry axis of the geometry. The boundary conditions B2 describe the ambient air conditions, where the gas composition is set equal to that of ambient air, assuming 1% of H_2O. The boundary B3 describes an outflow condition, where the viscous stresses are set to zero across the boundary, the convective flux of any species is continuous across the boundary, and the diffusive flux is set equal to 0. The boundaries described by B4 describe a wall where both velocity components are set to zero, in addition to setting the flux of every species equal to zero. Lastly, the boundary B5 describes the inlet, where helium gas flow is inserted into the domain. It is described by a normal velocity chosen to match the flow rate in the model as well as in the experiment (i.e., 2 SLM). The gas composition at the inlet was chosen to be in line with the composition of the Helium gas reported by the gas supplier.

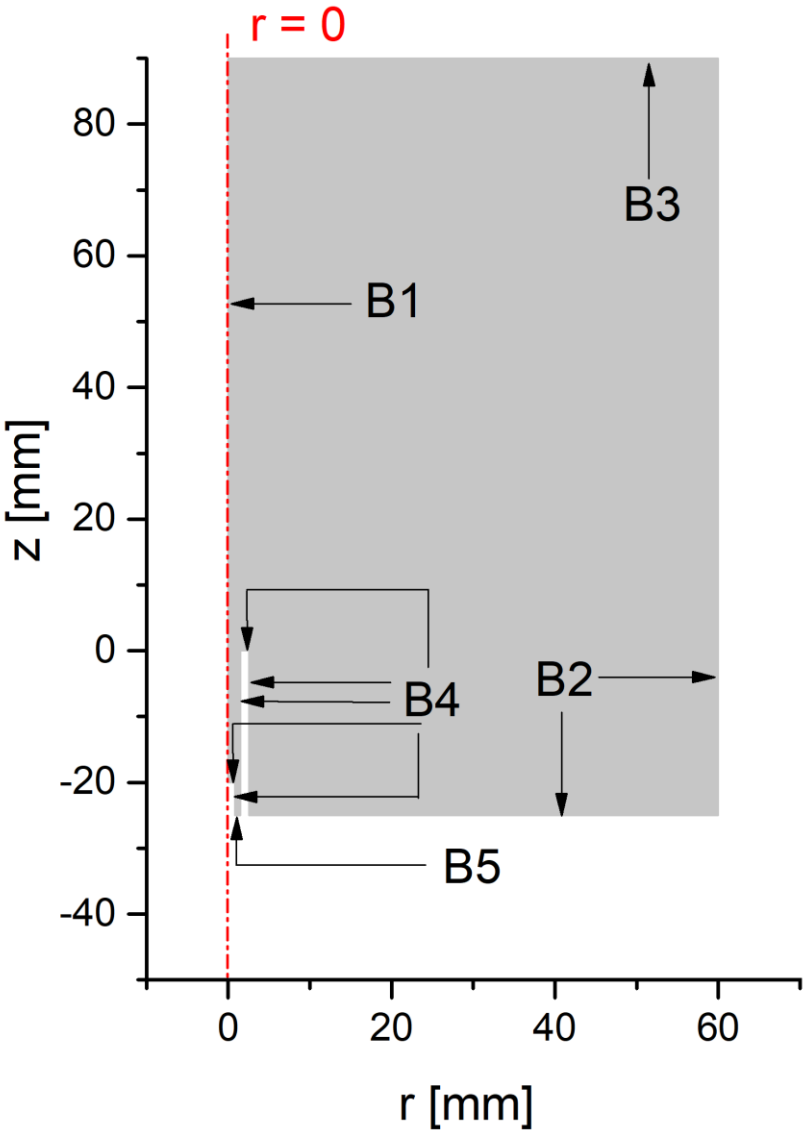

Figure B1: The computational domain of the model used in this study.

Table B2: Boundary conditions used in the model

Boundary	Mixture flow condition	j^{th} component condition
B1	Symmetry $\frac{\partial u_r}{\partial r} = \frac{\partial u_z}{\partial r} = \frac{\partial P}{\partial r} = 0$	Symmetry $\frac{\partial \omega_j}{\partial r} = 0$
B2	Open boundary $-pI + \mu\left(\nabla \vec{u} + \nabla \vec{u}^T\right) - \frac{2}{3}\mu(\nabla \cdot \vec{u})I = 0$	Fixed mass fraction $\omega_{N2} = 0.8061$ $\omega_{O2} = 0.2336$ $\omega_{H2O} = 0.0066$
B3	Open boundary $-pI + \mu\left(\nabla \vec{u} + \nabla \vec{u}^T\right) - \frac{2}{3}\mu(\nabla \cdot \vec{u})I = 0$	Outflow $-\hat{n} \cdot \rho\omega_j \sum_{k=1}^{N} D_{kj}\vec{d}_j = 0$
B4	Wall $u_r = 0, u_z = 0$	No flux $\hat{n} \cdot \vec{\Gamma}_j = 0$
B5	Inlet $u_z = V_{in}$	Fixed mass fraction $\omega_{N2} = 1.66 \times 10^{-4}$ $\omega_{O2} = 1.66 \times 10^{-4}$ $\omega_{H2O} = 1.66 \times 10^{-5}$

B.3 LIF model

In order to determine the ground state OH density based on n_{exc}, the 4-level collisional radiative model reported by Verreycken et al. was utilized.[160] Briefly, the model follows the densities of 3 laser-excited levels of OH in addition to the ground state. The followed levels are the ground state OH X(v''=0), OH A(v'=1), OH A(v'=0), and OH X(v''=1). For each level an ordinary differential equation is solved describing the gains and the losses of that level, leading to a coupled system of 4 equations. The processes described in the system are the radiative excitation by the laser, the quenching by air constituents, and the vibrational relaxation. The latter corresponds to the energy dissipation by a molecule to return to an equilibrium state. It is assumed in the model that the rotational energy transfer is much faster than the other processes; thus, the rotational levels are not resolved. The inputs to the 4-level model include the experimental parameters listed in Table 4, the gas composition determined by the flow model described in Appendix B1, and an estimated ground state OH density. Solving the 4-level model provides a prediction of the LIF signal intensity, which, by comparison to the measured LIF signal intensity is used to determine the actual ground-state OH density. Full details of the implementation can be found in the works of Verreycken and colleagues.[160]

References

1. Graves, D. B. Reactive species from cold atmospheric plasma: Implications for cancer therapy. *Plasma Process. Polym.* **11**, 1120–1127 (2014).
2. Boselli, M. *et al.* Schlieren high-speed imaging of a nanosecond pulsed atmospheric pressure non-equilibrium plasma jet. *Plasma Chem. Plasma Process.* **34**, 853–869 (2014).
3. Robert, E. *et al.* Rare gas flow structuration in plasma jet experiments. *Plasma Sources Sci. Technol.* **23**, 12003 (2014).
4. Sobota, A. *et al.* Electric field measurements in a kHz-driven He jet - The influence of the gas flow speed. *Plasma Sources Sci. Technol.* **25**, (2016).
5. Darny, T. *et al.* Plasma action on helium flow in cold atmospheric pressure plasma jet experiments. *Plasma Sources Sci. Technol.* **26**, 105001 (2017).
6. Panchapakesan, N. R. & Lumley, J. L. Turbulence Measurements in Axisymmetric Jets of Air and Helium. Part 2. Helium Jet. *J. Fluid Mech.* **246**, 225–247 (1993).
7. Tropea, C., Yarin, A. L. & Foss, J. F. *Springer Handbook of Experimental Fluid Mechanics*. (2007).
8. Wu, C. S., Wang, L., Ren, W. J. & Zhang, X. Y. Plasma arc welding: Process, sensing, control and modeling. *J. Manuf. Process.* **16**, 74–85 (2014).
9. Nemchinsky, V. A. & Severance, W. S. What we know and what we do not know about plasma arc cutting. *J. Phys. D. Appl. Phys.* **39**, (2006).
10. E, M. Airflow control by non-thermal plasma actuators. *J. Phys. D. Appl. Phys.* **40**, 605 (2007).
11. Laroussi, M. & Akan, T. Arc-free atmospheric pressure cold plasma jets: A review. *Plasma Process. Polym.* **4**, 777–788 (2007).
12. Laroussi, M. Low-temperature plasmas for medicine? *IEEE Trans. Plasma Sci.* **37**, 714–725 (2009).
13. Fridman, A. & Kennedy, L. A. *Plasma Physics and Engineering*. *Plasma Physics and Engineering* (2004). doi:10.4324/9780203334874.
14. Fridman, A. *Plasma Chemistry*. *Vasa* (2008). doi:10.1017/CBO9780511546075.
15. Bishop, C. Vacuum Deposition onto Webs, Films and Foils. *Vac. Depos. onto Webs, Film. Foils* (2011) doi:10.1016/C2009-0-64179-9.
16. Kohli, R. & Mittal, K. L. *Developments in Surface Contamination and Cleaning*. *Developments in Surface Contamination and Cleaning* vol. 10

(2016).

17. Montijn, C. & Ebert, U. Diffusion correction to the Raether-Meek criterion for the avalanche-to-streamer transition. *J. Phys. D. Appl. Phys.* **39**, 2979–2992 (2006).
18. Chirokov, A., Gutsol, A. & Fridman, A. Atmospheric pressure plasma of dielectric barrier discharges. *Pure Appl. Chem.* **77**, 487–495 (2005).
19. Chirokov, A. *et al.* A study of two-dimensional microdischarge pattern formation in dielectric barrier discharges. *Plasma Chem. Plasma Process.* **26**, 127–135 (2006).
20. Winter, J., Brandenburg, R. & Weltmann, K. D. Atmospheric pressure plasma jets: An overview of devices and new directions. *Plasma Sources Sci. Technol.* **24**, (2015).
21. Lu, X., Naidis, G. V., Laroussi, M. & Ostrikov, K. Guided ionization waves: Theory and experiments. *Phys. Rep.* **540**, 123–166 (2014).
22. Wang, R., Gao, Y., Zhang, C., Yan, P. & Shao, T. Dynamics of Plasma Bullets in a Microsecond-Pulse-Driven Atmospheric-Pressure He Plasma Jet. *IEEE Trans. Plasma Sci.* **44**, 393–397 (2016).
23. Gong, W. *et al.* Control of radial propagation and polarity in a plasma jet in surrounding Ar. *Phys. Plasmas* **25**, (2018).
24. Shao, T. *et al.* Comparison of Atmospheric-Pressure He and Ar Plasma Jets Driven by Microsecond Pulses. *IEEE Trans. Plasma Sci.* **43**, 726–732 (2015).
25. Baek, E. J., Joh, H. M., Kim, S. J. & Chung, T. H. Effects of the electrical parameters and gas flow rate on the generation of reactive species in liquids exposed to atmospheric pressure plasma jets. *Phys. Plasmas* **23**, (2016).
26. Pei, X. *et al.* Dynamics of the gas flow turbulent front in atmospheric pressure plasma jets. *Plasma Sources Sci. Technol.* **25**, 035013 (2016).
27. Qaisrani, M. H. *et al.* Study on dynamics of the influence exerted by plasma on gas flow field in non-thermal atmospheric pressure plasma jet. *Phys. Plasmas* **23**, (2016).
28. Kang, H. R., Chung, T. H., Joh, H. M. & Kim, S. J. Effects of dielectric tube shape and pin-electrode diameter on the plasma plume in atmospheric pressure helium plasma jets. *IEEE Trans. Plasma Sci.* **45**, 691–697 (2017).
29. Canal, C. *et al.* Plasma-induced selectivity in bone cancer cells death. *Free Radic. Biol. Med.* **110**, 72–80 (2017).
30. Yambe, K. & Saito, H. Estimation of flow channel parameters for flowing gas mixed with air in atmospheric-pressure plasma jets. *J. Phys. Soc. Japan* **86**, 1–5 (2017).

31. Xia, Y. *et al.* Propagation of atmospheric-pressure ionization waves along the tapered tube. *Phys. Plasmas* **25**, 2–7 (2018).

32. Naidis, G. V & Walsh, J. L. The effects of an external electric field on the dynamics of cold plasma jets—experimental and computational studies. *J. Phys. D. Appl. Phys.* **46**, 095203 (2013).

33. Papadopoulos, P. K. *et al.* Interpretation of the gas flow field modification induced by guided streamer ('plasma bullet') propagation. *J. Phys. D. Appl. Phys.* **47**, (2014).

34. Mirpour, S., Ghomi, H., Piroozmand, S. & Nikkhah, M. The Selective Characterization of Nonthermal Atmospheric Pressure Plasma Jet on Treatment of Human Breast Cancer and Normal Cells. *IEEE Trans. Plasma Sci.* **42**, 315–322 (2014).

35. Whalley, R. D. & Walsh, J. L. Turbulent jet flow generated downstream of a low temperature dielectric barrier atmospheric pressure plasma device. *Sci. Rep.* **6**, 1–11 (2016).

36. Engelhardt, M. *et al.* Interaction of an argon plasma jet with a silicon wafer. *J. Phys. D. Appl. Phys.* **49**, 145201 (2016).

37. Xiang, Q. *et al.* Antibacterial activity and a membrane damage mechanism of plasma-activated water against Pseudomonas deceptionensis CM2. *Lwt* **96**, 395–401 (2018).

38. Urabe, K., Ito, Y., Sakai, O. & Tachibana, K. Interaction between dielectric barrier discharge and positive streamer in helium plasma jet at atmospheric pressure. *Jpn. J. Appl. Phys.* **49**, 1060011–1060016 (2010).

39. Bhatt, S. *et al.* Efficacy of low-temperature plasma-activated gas disinfection against biofilm on contaminated GI endoscope channels. *Gastrointest. Endosc.* **89**, 105–114 (2019).

40. Kostov, K. G., Machida, M., Prysiazhnyi, V. & Honda, R. Y. Transfer of a cold atmospheric pressure plasma jet through a long flexible plastic tube. *Plasma Sources Sci. Technol.* **24**, (2015).

41. Cho, G., Kim, Y. & Uhm, H. S. The jet-stream channels of gas and plasma in atmospheric-pressure plasma jets. *J. Korean Phys. Soc.* **69**, 525–535 (2016).

42. Robert, E. *et al.* Experimental study of a compact nanosecond plasma gun. *Plasma Process. Polym.* **6**, 795–802 (2009).

43. Winter, J., Nishime, T. M. C., Glitsch, S., Lühder, H. & Weltmann, K. D. On the development of a deployable cold plasma endoscope. *Contrib. to Plasma Phys.* **58**, 404–414 (2018).

44. Winter, J. *et al.* Enhanced atmospheric pressure plasma jet setup for

endoscopic applications. *J. Phys. D. Appl. Phys.* **52**, (2019).

45. Kim, J. Y. *et al.* Single-cell-level cancer therapy using a hollow optical fiber-based microplasma. *Small* **6**, 1474–1478 (2010).
46. Kim, J. Y. *et al.* Single-cell-level microplasma cancer therapy. *Small* **7**, 2291–2295 (2011).
47. Xiong, Z. & Kushner, M. J. Atmospheric pressure ionization waves propagating through a flexible high aspect ratio capillary channel and impinging upon a target. *Plasma Sources Sci. Technol.* **21**, (2012).
48. Judée, F., Merbahi, N., Wattieaux, G. & Yousfi, M. Analysis of Ar plasma jets induced by single and double dielectric barrier discharges at atmospheric pressure. *J. Appl. Phys.* **120**, (2016).
49. Bekeschus, S., Schmidt, A., Weltmann, K. D. & von Woedtke, T. The plasma jet kINPen – A powerful tool for wound healing. *Clin. Plasma Med.* **4**, 19–28 (2016).
50. Nie, Q. Y., Cao, Z., Ren, C. S., Wang, D. Z. & Kong, M. G. A two-dimensional cold atmospheric plasma jet array for uniform treatment of large-area surfaces for plasma medicine. *New J. Phys.* **11**, (2009).
51. Ghasemi, M., Olszewski, P., Bradley, J. W. & Walsh, J. L. Interaction of multiple plasma plumes in an atmospheric pressure plasma jet array. *J. Phys. D. Appl. Phys.* **46**, (2013).
52. Fang, Z., Ding, Z., Shao, T. & Zhang, C. Hydrophobic surface modification of epoxy resin using an atmospheric pressure plasma jet array. *IEEE Trans. Dielectr. Electr. Insul.* **23**, 2288–2293 (2016).
53. Cui, X., Yan, B., Zhang, B. & Fang, Z. Improving surface hydrophobicity of glass using an atmospheric pressure plasma jet array in Ar/TMS. *Vacuum* **151**, 15–24 (2018).
54. Park, H. J. *et al.* Microplasma Jet Arrays as a Therapeutic Choice for Fungal Keratitis. *Sci. Rep.* **8**, 2422 (2018).
55. Wang, T. *et al.* Low temperature atmospheric microplasma jet array for uniform treatment of polymer surface for flexible electronics. *J. Micromechanics Microengineering* **27**, (2017).
56. Wan, M., Liu, F., Fang, Z., Zhang, B. & Wan, H. Influence of gas flow and applied voltage on interaction of jets in a cross-field helium plasma jet array. *Phys. Plasmas* **24**, (2017).
57. Robert, E., Darny, T., Dozias, S., Iseni, S. & Pouvesle, J. M. New insights on the propagation of pulsed atmospheric plasma streams: From single jet to multi jet arrays. *Phys. Plasmas* **22**, (2015).
58. Lietz, A. M., Damany, X., Robert, E., Pouvesle, J.-M. & Kushner, M. J.

Ionization wave propagation in an atmospheric pressure plasma multi-jet. *Plasma Sources Sci. Technol.* **28**, 125009 (2019).

59. Oh, J. S. *et al.* Imaging gas and plasma interactions in the surface-chemical modification of polymers using micro-plasma jets. *J. Phys. D. Appl. Phys.* **44**, (2011).
60. Park, S., Cvelbar, U., Choe, W. & Moon, S. Y. The creation of electric wind due to the electrohydrodynamic force. *Nat. Commun.* **9**, (2018).
61. Chen, Z. *et al.* Bullet-shaped ionization front of plasma jet plumes driven by microwave pulses at atmospheric gas pressure. *J. Appl. Phys.* **122**, (2017).
62. Teschke, M., Kedzierski, J., Finantu-Dinu, E. G., Korzec, D. & Engemann, J. High-speed photographs of a dielectric barrier atmospheric pressure plasma jet. *IEEE Trans. Plasma Sci.* **33**, 310–311 (2005).
63. Lu, X., Laroussi, M. & Puech, V. On atmospheric-pressure non-equilibrium. (2012) doi:10.1088/0963-0252/21/3/034005.
64. Naidis, G. V. Modelling of streamer propagation in atmospheric-pressure helium plasma jets. *J. Phys. D. Appl. Phys.* **43**, (2010).
65. Naidis, G. V. Modelling of plasma bullet propagation along a helium jet in ambient air. *J. Phys. D. Appl. Phys.* **44**, 215203 (2011).
66. Boeuf, J. P. & Pitchford, L. C. Two-dimensional model of a capacitively coupled rf discharge and comparisons with experiments in the Gaseous Electronics Conference reference reactor. *Phys. Rev. E* **51**, 1376–1390 (1995).
67. Breden, D., Miki, K. & Raja, L. L. Computational study of cold atmospheric nanosecond pulsed helium plasma jet in air. *Appl. Phys. Lett.* **99**, (2011).
68. Breden, D., Miki, K. & Raja, L. L. Self-consistent two-dimensional modeling of cold atmospheric-pressure plasma jets/bullets. *Plasma Sources Sci. Technol.* **21**, (2012).
69. Boeuf, J. P., Yang, L. L. & Pitchford, L. C. Dynamics of a guided streamer ('plasma bullet') in a helium jet in air at atmospheric pressure. *J. Phys. D. Appl. Phys.* **46**, (2013).
70. Robert, E. *et al.* Characterization of pulsed atmospheric-pressure plasma streams (PAPS) generated by a plasma gun. *Plasma Sources Sci. Technol.* **21**, 034017 (2012).
71. Ye, R. & Zheng, W. Temporal-spatial-resolved spectroscopic study on the formation of an atmospheric pressure microplasma jet. *Appl. Phys. Lett.* **93**, 1–4 (2008).
72. Brandenburg, R. Dielectric barrier discharges: Progress on plasma sources

and on the understanding of regimes and single filaments. *Plasma Sources Sci. Technol.* **26**, (2017).

73. Deepak, G. D., Joshi, N. K. & Prakash, R. Model analysis and electrical characterization of atmospheric pressure cold plasma jet in pin electrode configuration. *AIP Adv.* **8**, (2018).
74. Wild, R., Gerling, T., Bussiahn, R., Weltmann, K. D. & Stollenwerk, L. Phase-resolved measurement of electric charge deposited by an atmospheric pressure plasma jet on a dielectric surface. *J. Phys. D. Appl. Phys.* **47**, (2014).
75. Maletić, D. *et al.* Time-resolved optical emission imaging of an atmospheric plasma jet for different electrode positions with a constant electrode gap. *Plasma Sources Sci. Technol.* **24**, (2015).
76. Xiong, Z., Robert, E., Sarron, V., Pouvesle, J. M. & Kushner, M. J. Dynamics of ionization wave splitting and merging of atmospheric-pressure plasmas in branched dielectric tubes and channels. *J. Phys. D. Appl. Phys.* **45**, (2012).
77. Laroussi, M. Low-Temperature Plasma Jet for Biomedical Applications : A Review. *IEEE Trans. Plasma Sci.* **43**, 703–712 (2015).
78. Reuter, S., Von Woedtke, T. & Weltmann, K. D. The kINPen - A review on physics and chemistry of the atmospheric pressure plasma jet and its applications. *J. Phys. D. Appl. Phys.* **51**, (2018).
79. Sretenović, G. B., Krstić, I. B., Kovačević, V. V., Obradović, B. M. & Kuraica, M. M. Spatio-temporally resolved electric field measurements in helium plasma jet. *J. Phys. D. Appl. Phys.* **47**, (2014).
80. Kovačević, V. V. *et al.* The effect of liquid target on a nonthermal plasma jet - Imaging, electric fields, visualization of gas flow and optical emission spectroscopy. *J. Phys. D. Appl. Phys.* **51**, (2018).
81. Bourdon, A. *et al.* Numerical and experimental study of the dynamics of a μ s helium plasma gun discharge with various amounts of N 2 admixture. *Plasma Sources Sci. Technol.* **25**, 035002 (2016).
82. Liu, F., Zhang, D. & Wang, D. The influence of air on streamer propagation in atmospheric pressure cold plasma jets. *Thin Solid Films* **521**, 261–264 (2012).
83. Begum, A., Laroussi, M. & Pervez, M. R. Atmospheric pressure He-air plasma jet: Breakdown process and propagation phenomenon. *AIP Adv.* **3**, (2013).
84. Wang, R. *et al.* Effect of pulse polarity on the temporal and spatial emission of an atmospheric pressure helium plasma jet. *Plasma Sources Sci. Technol.*

25, (2016).

85. Olszewski, P., Wagenaars, E., McKay, K., Bradley, J. W. & Walsh, J. L. Measurement and control of the streamer head electric field in an atmospheric-pressure dielectric barrier plasma jet. *Plasma Sources Sci. Technol.* **23**, (2014).
86. Joshi, R. P., Sridhara, V. & Schoenbach, K. H. Microscopic calculations of local lipid membrane permittivities and diffusion coefficients for application to electroporation analyses. *Biochem. Biophys. Res. Commun.* **348**, 643–648 (2006).
87. Norberg, S. A., Johnsen, E. & Kushner, M. J. Helium atmospheric pressure plasma jets interacting with wet cells: delivery of electric fields. *J. Phys. D. Appl. Phys.* **49**, 185201 (2016).
88. Lin, L. & Keidar, M. Cold atmospheric plasma jet in an axial DC electric field. *Phys. Plasmas* **23**, (2016).
89. Walsh, J. L., Olszewski, P. & Bradley, J. W. The manipulation of atmospheric pressure dielectric barrier plasma jets. *Plasma Sources Sci. Technol.* **21**, 034007 (2012).
90. Hasan, M. I. & Bradley, J. W. Computational model of the interaction of a helium atmospheric-pressure jet with a dielectric surface. *J. Phys. D. Appl. Phys.* **48**, (2015).
91. Qian, M. *et al.* Gas flow dependence of atmospheric pressure plasma needle discharge characteristics. *Jpn. J. Appl. Phys.* **55**, (2016).
92. Liang, M. H., Liang, Y. J., Chai, J. Y., Zhou, S. S. & Jiang, J. G. Reduction of methanol in brewed wine by the use of atmospheric and room-temperature plasma method and the combination optimization of malt with different adjuncts. *J. Food Sci.* **79**, M2308–M2314 (2014).
93. Oh, J.-S. S., Walsh, J. L. & Bradley, J. W. Plasma bullet current measurements in a free-stream helium capillary jet. *Plasma Sources Sci. Technol.* **21**, 034020 (2012).
94. Boeuf, J. P. & Pitchford, L. C. Electrohydrodynamic force and aerodynamic flow acceleration in surface dielectric barrier discharge. *J. Appl. Phys.* **97**, (2005).
95. Hasan, M. I. & Bradley, J. W. Reassessment of the body forces in a He atmospheric-pressure plasma jet: A modelling study. *J. Phys. D. Appl. Phys.* **49**, (2015).
96. Xiong, Q. *et al.* Length control of He atmospheric plasma jet plumes: Effects of discharge parameters and ambient air. *Phys. Plasmas* **16**, 1–7 (2009).

97. Lu, Y., Wu, S., Cheng, W. & Lu, X. Electric field measurements in an atmospheric-pressure microplasma jet using Stark polarization emission spectroscopy of helium atom. *Eur. Phys. J. Spec. Top.* **226**, 2979–2989 (2017).

98. Ni, Y., Lynch, M. J., Modic, M., Whalley, R. D. & Walsh, J. L. A solar powered handheld plasma source for microbial decontamination applications. *J. Phys. D. Appl. Phys.* **49**, 355203 (2016).

99. Lissaman, P. B. S. Low-Reynolds-Number Airfoils. *Annu. Rev. Fluid Mech.* **15**, 223–239 (1983).

100. Todde, V., Spazzini, P. G. & Sandberg, M. Experimental analysis of low-Reynolds number free jets: Evolution along the jet centerline and Reynolds number effects. *Exp. Fluids* **47**, 279–294 (2009).

101. Jazaei, R. *Fluid Mechanics Experiments*. *Synthesis Lectures on Mechanical Engineering* vol. 5 (2020).

102. Brown, G. O. The history of the Darcy-Weisbach equation for pipe flow resistance. *Proc. Environ. Water Resour. Hist.* 34–43 (2002) doi:10.1061/40650(2003)4.

103. Whalley, R. D. & Walsh, J. L. Turbulent jet flow generated downstream of a low temperature dielectric barrier atmospheric pressure plasma device. *Nat. Publ. Gr.* (2016) doi:10.1038/srep31756.

104. Abramovich, G. General Properties of Turbulent Jets. *theory Turbul. jets* 3–49 (2003) doi:10.1515/9783110823080.77.

105. Chen, C. J. & Rodi, W. *Vertical turbulent buoyent jets: a review of experimental data*. (Pergamon Press, 1980).

106. Pai, S. *Fluid dynamics of jets*. (D. Van Nostrand Company, Inc, 1954).

107. Sato, H. & Sakao, F. An experimental investigation of the instability of a two-dimensional jet at low Reynolds numbers. *J. Fluid Mech.* **20**, 337–352 (1964).

108. Sautet, J. C. & Stepowski, D. Dynamic behavior of variable-density, turbulent jets in their near development fields. *Phys. Fluids* **7**, 2796–2806 (1995).

109. Graham K. Taylor, Robert L. Nudds & Adrian L. R. Thomas. Flying and swimming animals cruise at a Strouhal number tuned for high power efficiency. *Nature* **425**, 705–707 (2003).

110. Alexander, R. M. N. *Principles of animal locomotion*. *Principles of Animal Locomotion* (2013). doi:10.1644/1545-1542(2004)085<0584:br>2.0.co;2.

111. Hendricks, E. W. *et al.* Observations of Dolphin Swimming Speed and Strouhal Number. 13–43 (1998).

112. Ponta, F. L. & Aref, H. Strouhal-reynolds number relationship for vortex streets. *Phys. Rev. Lett.* **93**, 1–4 (2004).

113. Rienstra, S. W. A small Strouhal number analysis for acoustic wave-jet flow-pipe interaction. *J. Sound Vib.* **86**, 539–556 (1983).

114. Rayleigh, Lord. On the Stability, or Instability, of certain Fluid Motions. *Proc. London Math. Soc.* **s1-11**, 57–72 (1879).

115. Lessen, M. On the inviscid stability of the laminar mixing of two parallel streams of a compressible fluid. *Nat. Adv. Comm. Aero. Wash.* **979**, (1950).

116. Betchov, R. & Szewczyk, A. Stability of a shear layer between parallel streams. *Phys. Fluids* **6**, 1391–1396 (1963).

117. Sato, H. Errata Experimental Investigation on the Transition of Laminar Separated Layer. *J. Phys. Soc. Japan* **11**, 1128A (1956).

118. Sato, H. Further Investigation on the Transition of Two-Dimensional Separated Layer at Subsonic Speeds. *J. Phys. Soc. Japan* **14**, 1797–1810 (1959).

119. Michalke, A. On spatially growing disturbances in an inviscid shear layer. *J. Fluid Mech.* **23**, 521–544 (1965).

120. Crow, S. C. & Champagne, F. H. Orderly structure in jet turbulence. *J. Fluid Mech.* **48**, 547–591 (1971).

121. Gutmark, E. & Ho, C. M. Preferred modes and the spreading rates of jets. *Phys. Fluids* **26**, 2932–2938 (1983).

122. O'Neill, P., Soria, J. & Honnery, D. The stability of low Reynolds number round jets. *Exp. Fluids* **36**, 473–483 (2004).

123. Bradley, J. W. *et al.* Schlieren photography of the outflow from a plasma jet. *IEEE Trans. Plasma Sci.* **39**, 2312–2313 (2011).

124. Batchelor, G. K. & Gill, A. E. Analysis of the stability of axisymmetric jets. *J. Fluid Mech.* **14**, 529–551 (1962).

125. Putnam, A. A. An experimental determination of the minimum reynolds number for instability in a free jet. *J. Appl. Mech. Trans. ASME* **30**, 476–477 (1960).

126. Peacock, T., Bradley, E., Hertzberg, J. & Lee, Y. C. Forcing a planar jet flow using MEMS. *Exp. Fluids* **37**, 22–28 (2004).

127. Michalke, A. On the inviscid instability of the hyperbolictangent velocity profile. *J. Fluid Mech.* **19**, 543–556 (1964).

128. Michalke, A. & Wille, R. No Title. *Proc. 11th Intern. Congr. Appl. Mech.* (1965).

129. Hallberg, M. P. & Srykowski, P. J. On the universality of global modes in

low-density axisymmetric jets. *J. Fluid Mech.* **569**, 493–507 (2006).

130. Symons, E. P. & Labus, T. L. Experimental investigation of an axisymmetric fully developed laminar free jet. *Narional Aeronaut. Sp. Adm.* **NASA TN D**-, (1971).
131. Malmström, T. G., Kirkpatrick, A. T., Christensen, B. & Knappmiller, K. D. Centreline velocity decay measurements in low-velocity axisymmetric jets. *J. Fluid Mech.* **346**, 363–377 (1997).
132. Hussein, H. J., Capp, S. P. & George, W. K. Velocity measurements in a high-Reynolds-number, momentum-conserving, axisymmetric, turbulent jet. *J. Fluid Mech.* **258**, 31–75 (1994).
133. Hinze, J. O. *Turbulence*. (McGraw-Hill, 1975).
134. Dryden, H. L. & Kuethe, a. M. *Effect of turbulence in wind tunnel measurements*. *NACA Technical Report* http://aerade.cranfield.ac.uk/ara/1931/naca-report-342.pdf (1930).
135. Murakami, T., Niemi, K., Gans, T., O'Connell, D. & Graham, W. G. Chemical kinetics and reactive species in atmospheric pressure helium-oxygen plasmas with humid-air impurities. *Plasma Sources Sci. Technol.* **22**, (2013).
136. Yonemori, S., Nakagawa, Y., Ono, R. & Oda, T. Measurement of OH density and airhelium mixture ratio in an atmospheric-pressure helium plasma jet. *J. Phys. D. Appl. Phys.* **45**, (2012).
137. Li, L. *et al.* OH radicals distribution in an Ar-H2O atmospheric plasma jet. *Phys. Plasmas* **20**, (2013).
138. Naidis, G. V. Modelling of OH production in cold atmospheric-pressure He-H2O plasma jets. *Plasma Sources Sci. Technol.* **22**, (2013).
139. Reuter, S. *et al.* The Influence of Feed Gas Humidity Versus Ambient Humidity on Atmospheric Pressure Plasma Jet-Effluent Chemistry and Skin Cell Viability. *IEEE Trans. Plasma Sci.* **43**, 3185–3192 (2015).
140. Michalke, A. The instability of free shear layers. *Prog. Aerosp. Sci.* **12**, 213–216 (1972).
141. Melling, A. Tracer particles and seeding for particle image velocimetry. *Meas. Sci. Technol.* **8**, 1406–1416 (1997).
142. Tropea, C. Optical Particle Characterization in Flows. *Annu. Rev. Fluid Mech.* **43**, 399–426 (2011).
143. Zhang, Y., Cheng, H., Gao, H., Liu, D. & Lu, X. On the charged aerosols generated by atmospheric pressure non-equilibrium plasma. *High Volt.* (2020) doi:10.1049/hve2.12052.

144. Fan, L. *et al*. Laser-induced incandescence particle image velocimetry (LII-PIV) for two-phase flow velocity measurement. *Exp. Fluids* **59**, 1–14 (2018).

145. Hübner, S., Sousa, J. S., Puech, V., Kroesen, G. M. W. & Sadeghi, N. Electron properties in an atmospheric helium plasma jet determined by Thomson scattering. *J. Phys. D. Appl. Phys.* **47**, (2014).

146. Dantec Dynamics. Particle Image Velocimetry principle schematic.

147. Mie, G. Beiträge zur Optik trüber Medien, speziell kolloidaler Metallösungen. *Ann. Phys.* **330**, 377–445 (1908).

148. Hulst, H. C. van de. *Light scattering by small particles*. (John Wiley & Sons, 1981).

149. Fabelinkskii, I. L. *Molecular Scattering of Light*. (Plenum Press, 1968). doi:10.1007/978-1-4684-1740-1.

150. Strutt, J. W. LVIII. On the scattering of light by small particles. *London, Edinburgh, Dublin Philos. Mag. J. Sci.* **41**, (1871).

151. S., L. R. F. R. XXXIV. On the transmission of light through an atmosphere containing small particles in suspension, and on the origin of the blue of the sky. *London, Edinburgh, Dublin Philos. Mag. J. Sci.* **47**, (1899).

152. Andrews, D. L. *Rayleigh Scattering and Raman Effect, Theory*. *Encyclopedia of Spectroscopy and Spectrometry* (Elsevier Ltd., 2016). doi:10.1016/B978-0-12-409547-2.11337-X.

153. Sneep, M. & Ubachs, W. Direct measurement of the Rayleigh scattering cross section in various gases. *J. Quant. Spectrosc. Radiat. Transf.* **92**, 293–310 (2005).

154. Thalman, R., Zarzana, K. J., Tolbert, M. A. & Volkamer, R. Rayleigh scattering cross-section measurements of nitrogen, argon, oxygen and air. *J. Quant. Spectrosc. Radiat. Transf.* **147**, 171–177 (2014).

155. Ground, C. R., Gopal, V. & Maddalena, L. Filtered Rayleigh scattering mixing measurements of merging and non-merging streamwise vortex interactions in supersonic flow. *Exp. Fluids* **59**, (2018).

156. Gu, Z., Ubachs, W., Marques, W. & Van De Water, W. Rayleigh-Brillouin Scattering in Binary-Gas Mixtures. *Phys. Rev. Lett.* **114**, (2015).

157. Bonatto, J. R. & Marques, W. Kinetic model analysis of light scattering in binary mixtures of monatomic ideal gases. *J. Stat. Mech. Theory Exp.* 367–384 (2005) doi:10.1088/1742-5468/2005/09/P09014.

158. Yonemori, S. & Ono, R. Flux of OH and O radicals onto a surface by an atmospheric-pressure helium plasma jet measured by laser-induced fluorescence. *J. Phys. D. Appl. Phys.* **47**, (2014).

159. Voráč, J., Dvořák, P., Procházka, V., Ehlbeck, J. & Reuter, S. Measurement of hydroxyl radical (OH) concentration in an argon RF plasma jet by laser-induced fluorescence. *Plasma Sources Sci. Technol.* **22**, (2013).

160. Verreycken, T., Van Der Horst, R. M., Sadeghi, N. & Bruggeman, P. J. Absolute calibration of OH density in a nanosecond pulsed plasma filament in atmospheric pressure He-H2O: Comparison of independent calibration methods. *J. Phys. D. Appl. Phys.* **46**, (2013).

161. Dilecce, G., Martini, L. M., Tosi, P., Scotoni, M. & De Benedictis, S. Laser induced fluorescence in atmospheric pressure discharges. *Plasma Sources Sci. Technol.* **24**, (2015).

162. Riès, D. *et al.* LIF and fast imaging plasma jet characterization relevant for NTP biomedical applications. *J. Phys. D. Appl. Phys.* **47**, (2014).

163. Yue, Y., Pei, X. & Lu, X. Comparison on the Absolute Concentrations of Hydroxyl and Atomic Oxygen Generated by Five Different Nonequilibrium Atmospheric-Pressure Plasma Jets. *IEEE Trans. Radiat. Plasma Med. Sci.* **1**, 541–549 (2017).

164. Amielh, M., Djeridane, T., Anselmet, F. & Fulachier, L. Velocity near-field of variable density turbulent jets. *Int. J. Heat Mass Transf.* **39**, 2149–2164 (1996).

165. Djeridane, T., Amielh, M., Anselmet, F. & Fulachier, L. Velocity turbulence properties in the near-field region of axisymmetric variable density jets. *Phys. Fluids* **8**, 1614–1630 (1996).

166. Hofmann, S., Van Gessel, A. F. H., Verreycken, T. & Bruggeman, P. Power dissipation, gas temperatures and electron densities of cold atmospheric pressure helium and argon RF plasma jets. *Plasma Sources Sci. Technol.* **20**, (2011).

167. Morabit, Y., Whalley, R. D., Robert, E., Hasan, M. I. & Walsh, J. L. Turbulence and entrainment in an atmospheric pressure dielectric barrier plasma jet. *Plasma Process. Polym.* (2019) doi:10.1002/ppap.201900217.

168. Pipa, A. V. *et al.* Absolute production rate measurements of nitric oxide by an atmospheric pressure plasma jet (APPJ). *J. Phys. D. Appl. Phys.* **41**, (2008).

169. McKay, K., Walsh, J. L. & Bradley, J. W. Observations of ionic species produced in an atmospheric pressure pulse-modulated RF plasma needle. *Plasma Sources Sci. Technol.* **22**, (2013).

170. Schmidt-Bleker, A. *et al.* Reactive species output of a plasma jet with a shielding gas device - Combination of FTIR absorption spectroscopy and gas phase modelling. *J. Phys. D. Appl. Phys.* **47**, (2014).

171. Reuter, S. *et al.* Atomic oxygen in a cold argon plasma jet: TALIF spectroscopy in ambient air with modelling and measurements of ambient species diffusion. *Plasma Sources Sci. Technol.* **21**, (2012).

172. Nikiforov, A. *et al.* Influence of air diffusion on the OH radicals and atomic O distribution in an atmospheric Ar (bio)plasma jet. *Plasma Sources Sci. Technol.* **23**, (2014).

173. Cohen, J. The evolution of instabilities in the axisymmetric jet. part 1. the linear growth of disturbances near the nozzle. *J. Fluid Mech.* **176**, 191–219 (1987).

174. Westerweel, J., Fukushima, C., Pedersen, J. M. & Hunt, J. C. R. Mechanics of the turbulent-nonturbulent interface of a jet. *Phys. Rev. Lett.* **95**, 1–4 (2005).

175. Lautrup, B. *Physics of continuous matter, second edition: Exotic and everyday phenomena in the macroscopic world*. *Physics of Continuous Matter, Second Edition: Exotic and Everyday Phenomena in the Macroscopic World* (2011).

176. Uchida, G., Takenaka, K. & Setsuhara, Y. Influence of voltage pulse width on the discharge characteristics in an atmospheric dielectric-barrier-discharge plasma jet. *Jpn. J. Appl. Phys.* **55**, (2016).

177. Mericam-Bourdet, N., Laroussi, M., Begum, A. & Karakas, E. Experimental investigations of plasma bullets. *J. Phys. D. Appl. Phys.* **42**, (2009).

178. Shao, T. *et al.* Temporal evolution of atmosphere pressure plasma jets driven by microsecond pulses with positive and negative polarities. *Epl* **107**, (2014).

179. Lietz, A. M., Johnsen, E. & Kushner, M. J. Plasma-induced flow instabilities in atmospheric pressure plasma jets. *Appl. Phys. Lett.* **111**, (2017).

180. Isbary, G. *et al.* A first prospective randomized controlled trial to decrease bacterial load using cold atmospheric argon plasma on chronic wounds in patients. *Br. J. Dermatol.* **163**, 78–82 (2010).

181. Isbary, G. *et al.* Successful and safe use of 2 min cold atmospheric argon plasma in chronic wounds: Results of a randomized controlled trial. *Br. J. Dermatol.* **167**, 404–410 (2012).

182. Chen, Z. *et al.* Inactivation of myeloma cancer cells by helium and argon plasma jets: The effect comparison and the key reactive species. *Phys. Plasmas* **25**, (2018).

183. Cells, T.-L. C., Thiyagarajan, M., Sarani, A. & Gonzales, X.

Characterization of Portable Resistive Barrier Plasma Jet and Its Direct and Indirect Treatment for Antibiotic Resistant Bacteria and. **40**, 3533–3545 (2012).

184. Mesbah, A. & Graves, D. B. Machine learning for modeling, diagnostics, and control of non-equilibrium plasmas. *J. Phys. D. Appl. Phys.* **52**, (2019).
185. Kee, R. J., Coltrin, M. E. & Glarborg, P. *Chemically reacting flow: theory and practice*. *Choice Reviews Online* vol. 41 (Wiley-Interscience, 2003).
186. Bird, R. B., Stewart, W. E. & Lightfoot, E. N. *Transport Phenomena*. (John Wiley & Sons, 2002).
187. Wasik, S. P. & McCulloh, K. E. Measurements of gaseous diffusion coefficients by a gas chromatographic technique. *J. Res. Natl. Bur. Stand. Sect. A Phys. Chem.* **73A**, 207 (1969).
188. Rohling, J. H., Shen, J., Wang, C., Zhou, J. & Gu, C. E. Determination of binary diffusion coefficients of gases using photothermal deflection technique. *Appl. Phys. B Lasers Opt.* **87**, 355–362 (2007).
189. Paganelli, C. V. & Kurata, F. K. Diffusion of water vapor in binary and ternary gas mixtures at increased pressures. *Respir. Physiol.* **30**, 15–26 (1977).
190. Chung, T. J. *Computational fluid dynamics*. (Cambridge University Press, 2002).
191. Xu, D. & Chen, J. Accurate estimate of turbulent dissipation rate using PIV data. *Exp. Therm. Fluid Sci.* **44**, 662–672 (2013).
192. Gualtieri, C., Angeloudis, A., Bombardelli, F., Jha, S. & Stoesser, T. On the values for the turbulent schmidt number in environmental flows. *Fluids* **2**, (2017).